Semi Annual Report

(January 1 — June 30, 2000)

Contract Number NAS5—31363

OCEAN OBSERVATIONS WITH EOS/MODIS:

Algorithm Development and Post Launch Studies

Howard R. Gordon
University of Miami
Department of Physics
Coral Gables, FL 33124
(Submitted July 14, 2000)

Preamble

This document describes our progress thus far toward completion of our research plans regarding two MODIS Ocean-related algorithms.

A. Retrieval of the Normalized Water-Leaving Radiance (Atmospheric Correction).
B. Retrieval of the Detached Coccolith/Calcite Concentration

Our plans for Fiscal Year 2000 are included in this report as **Appendix I**. Fiscal Year 2000 was to be heavily focused on validation of MODIS-derived products. Unfortunately, the delay of the launch of Terra required some modification of out initial plan. Our approach was to use SeaWiFS for *validating* MODIS *algorithms* in the absence of MODIS itself, and when MODIS data became available, to perform the required initialization exercise and validate the MODIS products directly. However, as we already know (from theoretical studies and from SeaWiFS), that there are certain situations in which the algorithms are unable to perform properly, or that there are items that have not been included in the initial implementation, a portion of our effort will be directed toward algorithm improvement. Thus, we break our effort into two broad components for each algorithm:

- Algorithm Improvement/Enhancement;
- Validation of MODIS Algorithms and Products.

Of course, these components will overlap in some instances.

RETREIVAL OF NORMALIZED WATER-LEAVING RADIANCE (ATMOSPHERIC CORRECTION)

Algorithm Improvement/Enhancement

1. Evaluation/Tuning of Algorithm Performance

Task Progress:

With the launch of Terra, the availability of MODIS imagery, and the processing of the imagery by SDST (MODAPS) and the Goddard DAAC, we were in a position to begin an initial evaluation of the performance of MODIS and the algorithms. We started this by looking in detail at MODIS Granual 2000102.2215, starting just south of the Equator and progressing to 20 degrees South in the vicinity of 160 degrees West. Our evaluation is described in detail in **Appendix II**. Based on what is presented in Appendix II for this single granual, we can conclude the following:

(1) The overall the retrieved water-leaving radiances on the average are in the correct ranges, suggesting that the overall system calibration and the atmospheric correction are in the nominal ranges; however, when the imagery is evaluated at full resolution many artifacts are apparent.
(2) The normalized water-leaving radiance at 551 nm, $nL_w(551)$, shows severe striping (a maximum of about 10% over the 10 detectors in the spectral band) normal to the subsatellite track, and the average value is ~ 50% too high.
(3) After correcting errors and omissions in the processing codes, and reprocessing the granual at Miami, this error in the average $nL_w(551)$ was reduced to ~ +10%; however, the striping in $nL_w(551)$ remained.
(4) After an initial attempt by R. Evans and co-workers at flat fielding the imagery, the strongly periodic nature of the striping was removed, but there was still some striping.
(5) The retrieved $nL_w(551)$ across a scan line showed some limb brightening that could be due to overall calibration errors or to the influence of an unaccounted variability in the system response as a function of scan angle.
(6) Bands 15 or 16, or both, (used for atmospheric correction) appear to display excessive noise. This may require averaging the atmospheric correction parameter $\varepsilon(15,16)$ over several pixels.
(7) Sun glint will likely render the eastern half of the scan useless in the tropics unless a correction scheme is developed.
(8) The striping in $nL_w(551)$ is not due to atmospheric correction, as $\varepsilon(15,16)$ does not show significant banding.
(9) A significant amount of work will be required to removing the striping from the MODIS derived products, as its root cause is probably spread

over several processes, e.g., instrument polarization sensitivity, variability in system response with scan angle, etc. Thus the improvement process will require an incremental resolution and balancing of the individual effects.

(10) Plans should be made to reprocess MODIS imagery as incremental progress is made.

In addition to evaluation of the initial performance of MODIS and the algorithms, we have implemented two enhancements: (1) a wind-speed dependent computation of the Rayleigh scattering contribution to the radiance at the sensor, and (2) correction software for removing some of the influence of the MODIS polarization sensitivity. The polarization software can become fully operational only after MSCT and SBRS agree on the validity of the analysis of the pre-launch polarization sensitivity characterization data. We consider resolving the polarization characterization issue to be of the highest priority for MCST in terms of MODIS ocean processing.

Anticipated Future Actions:

We will continue the evaluation of MODIS imagery, and work closely with R. Evans on removing the artifacts from the imagery. We will also try to evaluate the ramifications of averaging the atmospheric correction parameter over several pixels. One obvious problem with this approach is that a small cloud in any one pixel used in the averaging will influence several pixels, reducing the amount of usable data.

2. Implement the Initial Algorithm Enhancements

The most important enhancement we have been considering focussed on absorbing aerosols. These constitute an important unsolved atmospheric correction issue for case 1 waters, and these aerosols have a significant impact in many geographical areas. Two important situations in which absorbing aerosols make an impact are desert dust and urban pollution carried over the oceans by the winds. In the case of urban pollution the aerosol contains black carbon and usually exhibits absorption that is nonselective, i.e., the imaginary part of the refractive index (the absorption index) is independent of wavelength. In contrast, desert dust absorbs more in the blue than the red, i.e., the absorption index decreases with wavelength.

Task Progress:

We are in the process of extensively examining two enhancements: (1) the spectral matching algorithm (SMA) [Gordon, Du, and Zhang, "Remote sensing ocean color and aerosol properties: resolving the issue of aerosol absorption," *Applied Optics*, **36**, 8670-8684 (1997)]; and (2) the spectral optimization algorithm SOA [Chomko and Gordon, "Atmospheric correction of ocean color imagery: Use of the Junge power-law aerosol size distribution with variable refractive index to handle aerosol absorption," *Applied Optics* , **37**, 5560-5572 (1998)]. Simulations reveal that both algorithms have the potential to perform well in the presence of strongly absorbing aerosols.

Our progress to date toward algorithm enhancements for these aerosols are provided in **Appendices III and IV**. Appendix III is a paper (submitted to *Geophysical Research Letters*) describing a successful processing of SeaWiFS imagery in the Saharan dust zone using the SMA. Appendix IV is a paper (submitted to *Applied Optics*) that describes application of the SOA to SeaWiFS imagery off the U.S. East Coast using the SOA. The performance of the algorithms (compared to the standard SeaWiFS/MODIS algorithm) is very encouraging.

Anticipated Future Actions:

We will continue to evaluate the performance of these algorithms for possible inclusion in the MODIS processing software.

3. Study Future Enhancements

There are three additional issues that we are examining for inclusion into the MODIS algorithm: modeling the subsurface upwelling BRDF, understanding the influence of colored dissolve organic matter (CDOM) on the operation of the SOA and SMA, and removing the influence of whitecaps on the sea surface.

Task progress:

The subsurface upwelling BRDF

We have reduced the RADS BRDF data acquired during the MOCE-5 validation cruise in the Gulf of California. This is an excellent data set in that it spans a wide range of cholorophyll *a* concentrations. To study the influence of self-shading by the RADS instrument, we participated in Dennis Clark's February cruise and compared the measurements from RADS with those from a new smaller instrument Dennis Clark has developed for MOBY that will essentially eliminate the self-shading problem. These data are still being reduced. Similar measurements were made during a one-week MODIS initialization cruise in April.

The influence of CDOM on the SOA and SMA

We have replaced the Gordon et al. semianalytic radiance model [A semianalytic radiance model of ocean color, *Jour. Geophys. Res.*, **93(D9)**, 10909—10924, 1988] with a version of the Garver and Siegel reflectance model [Inherent optical property inversion of ocean color spectra and its biogeochemical interpretation: 1 time series from the Sargasso Sea, *Geophys. Res.*, **102C**, 18607—18625, 1997] in our SOA algorithm. The Garver and Siegel model has been tuned to the SeaBASS data set. This model includes absorption by CDOM, detritus, and phytoplankton, as well as particle backscattering. In contrast, the Gordon et al. model includes only chlorophyll absorption and particle backscattering. The principal difficulty incorporating CDOM is that this model requires

that seven (instead of six) parameters must be determined by eight spectral bands. A second difficulty is that the optical effect of CDOM on the water-leaving reflectance is similar to the effect of absorbing aerosols on the aerosol component of the reflectance. In our initial trial we processed the same imagery as processed in Appendix IV. The results suggest that the influence of CDOM is much more significant than expected.

Influence of whitecaps on the sea surface

A paper describing our determination of the whitecap-augmented reflectance was published in *JGR* [K.D. Moore, K.J. Voss, and H.R. Gordon, Spectral reflectance of whitecaps: Their contribution to water-leaving radiance, *Jour. Geophys. Res.*, **105(C3)**, 6493—6499, 2000].

Anticipated Future Actions:

The subsurface upwelling BRDF

We will compare the newly reduced BRDF data with our model, and estimate the RADS self-shading effects using the data from the February and April experiments.

The influence of CDOM on the SOA and SMA

We have acquired AOL measurements of CDOM from Frank Hoge on a flight line through one of the SeaWiFS images we processed. This track will be compared to CDOM retrievals by the SOA. We are also studying the optimization algorithm in detail to try to understand how best to avoid the spurious results that sometimes occur at isolated pixels. In addition, we are studying the scaling of the various optimized variables to try to improve the performance over a wider range of parameter values.

Influence of whitecaps on the sea surface

This work is now essentially complete. We will now operate the whitecap instrumentation only during MODIS validation cruises.

Validation of MODIS Algorithms and Products

4. Participate in MODIS Initialization/Validation Campaigns

This task refers to our participation in actual Terra/MODIS validation/initialization exercises.

Task Progress:

During the last six months we participated in a shortened MODIS initialization cruise (MOCE-6). The longer cruise was delayed until more favorable sun glint conditions could be obtained. This longer cruise will occur later this year or early next year depending on ship schedules and the Aqua launch schedule. We are now in the process of reducing the data obtained on MOCE-6.

In addition, we continued to maintain our CIMEL station in the Dry Tortugas during this period. This station will be used to help validate the MODIS derived aerosol optical depth (AOD), and aid in investigating the calibration of the near infrared (NIR) spectral bands of MODIS.

Anticipated future efforts:

We will complete analysis of the MOCE-6 data to provide an initial vicarious calibration for MODIS ocean bands. We will participate on the next MODIS initialization campaign when it occurs. We will make measurements of the sky radiance distribution (large angle and aureole), the in-water radiance distribution, AOD, and whitecap radiance. The Micro-Pulse LIDAR (MPL) system has been repaired by the manufacturer and will be operational for providing the aerosol's vertical distribution during this campaign. We are currently testing the MPL. To ensure success with the MPL in this effort, we obtained a spare detector to try to avoid the long delay experienced in the last repair cycle (difficult, because they are no longer being manufactured).

5. Participate in Validation Campaign (SeaWiFS)

As part of our effort to validate the MODIS normalized water-leaving radiance algorithm using SeaWiFS data, we participated in three long cruises, Aerosols99, INDOEX, and MOCE-5. This section describes those efforts.

Task Progress:

The Aerosols99 cruise took place between January 14 to February 8, 1999 between Norfolk, VA. and Cape Town, S.A. This was a multidisciplinary cruise with extensive measurements of the boundary layer aerosol (chemical, physical, and optical measurements), chemistry, and vertical sounding (radio-sondes, ozone-sondes, and our MPL), as well as in-water optics. It was very interesting as we encountered several aerosol types: North American continental aerosols, North Atlantic clean maritime aerosols, a Saharan dust event, biomass burning aerosols from the African continent, and South Atlantic maritime aerosols. The first regime (continental aerosols) occurred during a cloudy period so our optical measurements were limited. We found that the North Atlantic and South Atlantic maritime aerosols were similar, with optical depths in the range of 0.10 ± 0.03, with small angstrom exponents (0.30 ± 0.3). These aerosols were capped at approximately 1 km by a strong temperature inversion so most of the attenuation occurred below this. We calculated the level at which 90% of the AOD was

accounted for (from the surface up). In this area the 90% level for the attenuation was at 1-2 km. The Saharan dust event changed the optical properties of the column significantly. The AOD increased to 0.29±0.05, but the angstrom exponent remained low (0.36±0.13). The temperature inversion went to 1.5 km. The surface layer of the aerosols was capped by this inversion; however, another layer of aerosol was above this inversion and extended to 3 km or so. The 90% level for attenuation was at 2 km, with excursions up to 3 km at times. The biomass burning episode also had a high AOD (0.36±0.13) and was associated with the highest angstrom exponent experienced during the cruise (0.88±0.3), typical of smaller particles. The temperature structure in the atmosphere was more confusing with inversions occurring at many levels starting at 1 km. The aerosol extended very high into the atmosphere with the 90% level of attenuation at >3 km. At the end of this period the surface cleared before the upper atmosphere. Surface conditions indicated a very clean marine atmosphere, yet column properties showed a fairly turbid aerosol above this. As we continued south the entire column cleared and the aerosol structure reverted to the clean maritime case (AOD around 0.1, capped at 1 km). These results are described in detail in the attached **Appendices V** and **VI**.

The results from the INDOEX data set are still in the process of being prepared for publication. Thus far, one important result we participated in was the observation that absorbing aerosols tend to reduce cloud fraction [Ackerman, *et al.*, Reduction of tropical cloudiness by soot, *Science*, **288**, 1042-1047, 2000].

Anticipated future efforts:

We will complete our analysis of the INDOEX atmospheric data, and have manuscripts ready for submission within the next reporting period. We will use the INDOEX results to study the performance of our SOA and SMA algorithms with SeaWiFS imagery.

For MOCE-5 we are working extensively with the Sky and Aureole radiance distribution data to investigate the aerosol phase function retrieval methods.

We will complete analysis of the in-water radiance distribution data obtained during the MOCE-5 cruise, as well as those obtained during Aerosols99 and INDOEX. This data set provides an extensive body of upwelling radiance distributions with varying optical properties (Chlorophyll concentration, solar zenith angle). We will present results from this radiance distribution data set at the “Oceans from Space, Venice 2000” meeting in Venice, Italy in October.

RETRIEVAL OF DETACHED COCCOLITH/CALCITE CONCENTRATION

This last half year of work has focussed on several areas: 1) submitting a manuscript of publication on coccolithophore distributions from the Indian Ocean, 2) participating in the development of a new 3-band coccolithophore algorithm, 3) planning of a large-scale manipulative experiment for testing the MODIS suspended calcite algorithm, 4) finishing coccolith counts from 1999, evaluating the early MODIS coccolith products, and 5) monitoring bio-optical properties of a coccolithophore bloom in the Gulf of Maine,

Algorithm Evaluation/Improvement

Task Progress:

A second manuscript on our Arabian Sea has been submitted for publication [Balch, W. M., D. Drapeau, B. Bowler, and J. Fritz. Continuous measurements of calcite-dependent light scattering in the Arabian Sea. Submitted to**.** *Deep Sea Res. I*]. The results are summarized in the abstract provided below.

Continuous surface measurements of temperature, salinity, fluorescence and optical backscattering were made during *R/V Thompson* cruise #TN053 in the northern Arabian Sea ("Bio-Optical cruise"; October-November, 1995). The cruise covered the early NE monsoon period. Optical measurements involved estimates of total backscattering and "acidified backscattering" (measured after addition of a weak acid to dissolve calcium carbonate). Acid-labile backscattering was calculated as the difference between total- and acidified backscattering. Total and acid-labile backscattering were converted to the concentration of particulate organic carbon (POC) and particulate inorganic carbon (PIC; calcium carbonate), respectively, utilizing discrete samples taken along the cruise track for calibration. Backscattering data were frequently coherent with temperature, salinity, and density variability. Acid-labile backscattering values revealed that calcium carbonate accounted for 10-40% of the total optical backscattering in the region and the continuous records demonstrated distinct patches of coccolith-rich water. The northern region of the Arabian Sea had the highest acid-labile backscattering. Results suggest that PIC:POC ratios can vary over about four orders of magnitude. Highest surface values of PIC:POC approached 1 in several places. We also report qualitative observations of phytoplankton community structure made aboard ship, on fresh samples.

The observation that calcium carbonate accounted for 10-40% of the total optical backscattering, is particularly significant in oceanic optics, as the particles responsible for the observed backscattering in the sea are still a mystery.

We have also developed a new algorithm for retrieval of coccolith calcium carbonate from MODIS imagery. This algorithm utilizes only red and near infrared bands and does *not* require knowledge of the chlorophyll concentration, which is very difficult to estimate remotely in coccolithophore blooms. This algorithm is described in detail in **Appendix VII**.

Anticipated future efforts:

We will incorporate the new coccolithophore calcite algorithm into the MODIS processing code. We shall continue validating the new coccolithophore algorithm with both MODIS and SeaWiFS data. The principal difficulty in validation being that of simultaneous acquisition of coccolithophore data and satellite imagery because of the ephemeral nature of coccolithophore blooms. A novel approach toward remedying this is described below.

Validation of MODIS Algorithms and Products

Task Progress:

Chalk-Ex

Given our interest in monitoring coccolithophores and their suspended calcite, plus the major difficulty in predicting coccolithophore blooms in space and time, W.M. Balch had the idea to make a bloom, rather than hunt a bloom. The concept is relatively straight-forward. Bloom concentrations of calcium carbonate are ~10 g C as $CaCO_3$ m^{-2} of ocean water (integrated over the top 50m of the sea). Concentrations of coccoliths are thus ~200 mg C as $CaCO_3$ m^{-3}. Thus, in one km^2 of sea, there are ~10 metric tons of $CaCO_3$ (or ~ 10 cubic yards). We have performed two initial experiments, testing the feasibility of this approach. The first involved spreading 25 kg of chalk, the second, 0.9 tons. Our first large-scale "Chalk-Ex" experiment is designed to sea-truth the MODIS coccolith algorithm at slightly lower concentrations than found in a bloom, but still high enough to be easily visible to MODIS. We will make an elongated chalk patch with an area of ~3 km^2 (requiring ~ 26 cubic yards, or ~26 metric tonnes), which will be visible even at the 1km pixel resolution. We propose to make this patch in continental slope waters SW of Georges Bank, which is the main, ultimate, repository for coccolithophore blooms originating in the Gulf of Maine. Most of these blooms are ~100,000 km^2 features which form either in the Jordan Basin or Wilkinson Basin, and ultimately are advected around the northern flank of Georges Bank into slope waters. Note, previous blooms contained as much as ~8.3 million metric tonnes of $CaCO_3$ in the form of coccoliths, hence our experiment is quite innocuous compared to the real thing.

We will lay this patch by diluting ground Cretaceous chalk (from the same coccolith deposits which produced the White Cliffs of Dover) in surface sea water, and adding it to the wake of a steaming vessel in order to further mix it as the ship steams a "radiator" pattern. We will have optical instrumentation available aboard the same vessel, to validate the satellite optical measurements inside and outside the patch. The fate of this inert chalk will be to sink onto the continental slope. It is well known that the sediments of the continental slope consist of mostly $CaCO_3$ coccolith ooze [Milliman, J.D., Pilkey, O.H. and Ross, D.A., Sediments of the continental margin off the eastern United States. Geological Society of America Bulletin 83, 1315-1334, 1972.].

Chalk is commercially available, and ground so that it all passes a 10 μm sieve, with 50% of the particles having diameter <1.9 μm. The chalk is ~98% pure, and is used for everything from agricultural liming of soils, to absorbing polluting oils. It is likely that about 50% of the chalk will sink from surface waters on a time scale of hours, as the larger calcite particles will settle quite rapidly. Coccolith blooms of 100,000 km^2 typically are visible from satellite for 1-2 weeks. This time is determined by the rate of coccolithophore calcification and loss to zooplankton grazing. Field evidence shows, coccoliths are quickly consumed where they dissolve in the zooplankton guts or are incorporated into fast-sinking fecal pellets. Our laboratory evidence on sinking rates of this ground chalk suggests that it will be visible in surface waters for a few days after dispersal.

The timing of this experiment is fairly flexible. Our biggest constraint is that the weather be clear, so that NASA's satellite-borne ocean color sensors (SeaWiFS and Terra/MODIS) can see the experimental area. The experiment is planned for early August 2000, aboard the r/v Cape Hatteras. This is an optimal period for the first experiment due to the favorable cloud climatology at this time. We would like to repeat this experiment in the summer of 2001, but utilizing a larger research vessel, so that we could deploy sediment traps, and drifting arrays to monitor temperature, salinity and optics. Both of these features will allow better documentation of the sinking flux and bio-transformations of the $CaCO_3$. The Office of Naval Research requested a proposal from W. Balch, C. Pilskaln, and A. Plueddemann (already submitted) to use a patch of suspended chalk to monitor mixed layer dynamics, and the processes responsible for the loss of chalk particles from the mixed layer. If funded, the ONR experiment would provide another Chalk-Ex cruise in November, 2001, at no cost to NASA.

Coccolith and Coccolithophore Counts

Discrete samples for the 1999 field season were all processed, including coccolith concentration (microscopy, which was by far the most laborious). The 1999 field data sets have a wealth of information on coccolith concentrations in non-bloom conditions. All the atomic absorption samples have been sent to Scripps Inst. Of Oceanography for processing. We are awaiting the last numbers back to complete our spread sheets and write the papers.

2000 Coccolithophore Bloom in the Gulf of Maine

This year has seen a coccolithophore bloom directly along our SIMBIOS ferry track, which provided us with an unprecedented oppurtunity to monitor 1) pre-bloom conditions, 2) bloom growth, and 3) bloom demise. Coccolith concentrations were highest around Jordan Basin (on east and west sides). Perhaps the most impressive aspect was that MODIS was able to detect the bloom at concentrations lower than we originally imagined. This bodes well for the MODIS calcite algorithm. As of this writing, the bloom is decreasing in concentration. In terms of algorithm development, this bloom will provide us with the most sea-truth data, in concentration ranges much more commonly found in nature.

Anticipated future efforts:

As stated above, the implementation of "Chalk-Ex" will be done in August, 2000. The experiment, plus processing of the data, will occupy most of our MODIS effort for the next few months. In preparation for this experiment, we have purchased a free-fall Satlantic radiometer for acquiring vertical radiance data, and calculation of diffuse attenuation coefficients. We also will spend time processing samples and data from the recent Gulf of Maine coccolithophore bloom.

PUBLICATIONS

E. J. Welton, K. J. Voss, H. R. Gordon, H. Maring, A. Smirnov, B. Holben, B. Schmid, J. M. Livingston, P. B. Russell, P. A. Durkee, P. Formenti, M. O. Andreae, "Ground-based lidar measurements of aerosols during ACE-2: instrument description, results, and comparisons with other ground-based and airborne measurements", *Tellus*, **52B**, 568—593, 2000.

B. Schmid, J. M. Livingston, P. B. Russell, P. A. Durkee, H. H. Jonsson, D. R. Collins, R. C. Flagan, J. H. Seinfeld, S. Gassó, D. A. Hegg, E. Öström, K. J. Noone, E. J. Welton, K. J. Voss, H. R. Gordon, P. Formenti, and M. O. Andreae, "Clear sky closure studies of lower tropospheric aerosol and water vapor during ACE 2 using airborne sunphotometer, airborne in-situ, space-borne, and ground-based measurements", *Tellus*, **52B**, 636—651, 2000.

K.D. Moore, K. J. Voss, and H. R. Gordon, "Spectral reflectance of whitecaps: Their contribution to water leaving radiance", *Journal of Geophysical Research*, **105(C3)**, 6493—6499, 2000.

Ackerman, A. S., O. B. Toon, D. E. Stevens, A. J. Heymsfield, V. Ramanathan, and E. J. Welton, Reduction of tropical cloudiness by soot, *Science*, **288**, 1042—1047, 2000.

J. M. Ritter and K. J. Voss, A new instrument to measure the solar aureole from an unstable platform, *Journal of Atmospheric and Oceanic Technology* (In Press).

Vaillancourt, R. D. and W. M. Balch, Size distribution of coastal sub-micron particles determined by flow, field flow fractionation, *Limnology and Oceanography*, **45**, 485—492, 2000.

Graziano, L., W. Balch, D. Drapeau, B.Bowler, and S. Dunford, Organic and inorganic carbon production in the Gulf of Maine, *Continental Shelf Research,* **20**, 685—705, 2000.

Balch, W.M., D. Drapeau, and J. Fritz, Monsoonal forcing of calcification in the Arabian Sea, *Deep Sea Research II*, **47**, 1301—1333, 2000.

Balch, W.M., J. Vaughn, J. Novotny, D.T. Drapeau, R.D. Vaillancourt, J. Lapierre, and A. Ashe, Light scattering by viral suspensions, *Limnology and Oceanography*, **45**, 492—498, 2000.

Balch, W.M., D. Drapeau, B. Bowler and J. Fritz, Continuous measurements of calcite-dependent light scattering in the Arabian Sea, *Deep Sea Research I* (Submitted).

Gordon, H.R., G.C. Boynton, W.M. Balch, S.B. Groom, D.S. Harbour, and T.J. Smyth, Retrieval of Coccolithophore Calcite Concentration from SeaWiFS Imagery, *Geophysical Research Letters* (Submitted).

Moulin, C., H.R. Gordon, V.F. Banzon, and R.H. Evans, Assessment of Saharan dust absorption in the visible to improve ocean color retrievals and dust radiative forcing estimates from SeaWiFS, *Journal of Geophysical Research* (Submitted).

Moulin, C., H.R. Gordon, R.M. Chomko, V.F. Banzon, and R.H. Evans, Atmospheric correction of ocean color imagery through thick layers of Saharan dust, *Geophysical Research Letters* (Submitted).

Chomko, R.M. and H.R. Gordon, Atmospheric correction of ocean color imagery: Test of the spectral optimization algorithm with SeaWiFS, *Applied Optics*, (Submitted).

Voss, K. J., E. J. Welton, J. Johnson, A. Thompson, P. K. Quinn, and H. R. Gordon, Lidar Measurements During Aerosols99, *Journal of Geophysical Research* (Submitted).

Voss, K. J., E. J. Welton, P. K. Quinn, R. Frouin, M. Reynolds, and M. Miller, Aerosol Optical Depth Measurements During the Aerosols99 Experiment, *Journal of Geophysical Research* (Submitted).

Quinn, P. K., D. J. Coffman, T. S. Bates, T. L. Miller, J. E. Johnson, K. J. Voss, E. J. Welton, C. Neusüss, Dominant Aerosol Chemical Components and Their Contribution to Extinction During the Aerosols99 Cruise Across the Atlantic, *Journal of Geophysical Research* (Submitted).

Welton, E. J., P. J. Flatau, K. J. Voss, H. R. Gordon, K. Markowicz, J. R. Campbell, and J. D. Spinhirne, Micro-pulse Lidar Measurements of Aerosols and Clouds During INDOEX 1999, *Journal of Geophysical Research* (Submitted).

Collins, W. D., P. J. Rasch, B. E. Eaton, E. J. Welton, and J. D. Spinhirne, Improvements in aerosol forecasts from assimilation of in situ and remotely sensed aerosol properties, *Journal of Geophysical Research* (Submitted).

PRESENTATIONS

W. M. Balch, Drapeau, D. T., Bowler, B., Ashe, A., Vaillancourt, R., Dunford, S., and Graziano, L, Backscattering probability and calcite-dependent backscattering in the Gulf of Maine. Proceedings of the ASLO Meeting, Santa Fe, NM. *ASLO Santa Fe,* 1-5 February, 1999, p. 18.

H.R. Gordon, MODIS Atmospheric Correction Performance: Initial Evaluation, MODIS Science Team Meeting, Greenbelt, MD, June 7-9, 2000.

W.M. Balch, Chalk-Ex, MODIS Science Team Meeting, Greenbelt, MD, June 7-9, 2000.

ATTACHMENTS

Appendix I: Plans for FY 2000

Appendix II: MODIS Atmospheric Correction Performance: Initial Evaluation

Appendix III: Atmospheric correction of ocean color imagery through thick layers of Saharan dust

Appendix IV: Atmospheric correction of ocean color imagery: Test of the spectral optimization algorithm with SeaWiFS

Appendix V: Aerosol Optical Depth Measurements During the Aerosols99 Experiment

Appendix VI: Lidar Measurements During Aerosols99

Appendix VII: Retrieval of Coccolithophore Calcite Concentration from SeaWiFS Imagery

Appendix I

NASA/GSFC Contract No. NAS5-31363

OCEAN OBSERVATIONS WITH EOS/MODIS
Algorithm Development and Post Launch Studies

Howard R. Gordon
University of Miami
Department of Physics
Coral Gables, FL 33124

Plans for FY 00

Preamble

This document describes plans for Fiscal Year 2000 regarding two MODIS Ocean-related algorithms.

A. Retrieval of the Normalized Water-Leaving Radiance (Atmospheric Correction).

B. Retrieval of the Detached Coccolith/Calcite Concentration

Fiscal Year 2000 will be heavily focused on validation of MODIS-derived products. Unfortunately, the delay of the launch of Terra requires some modification of out initial plan. Our approach for the coming year will be to use SeaWiFS for *validating* MODIS *algorithms* in the absence of MODIS itself, and when MODIS data become available, to perform the required initialization exercise and validate the MODIS products directly. However, as we already know (from theoretical studies and from SeaWiFS) that there are certain situations in which the algorithms are unable to perform properly or that there are items that have not been included in the initial implementation, a portion of our effort will be directed toward algorithm improvement. Thus, we break our effort into two broad components for each algorithm:

- Algorithm Improvement/Enhancement;
- Validation of MODIS Algorithms and Products.

These components will overlap in some instances.

RETREIVAL OF NORMALIZED WATER-LEAVING RADIANCE (ATMOSPHERIC CORRECTION)

Algorithm Evaluation/Improvement

1. *Evaluation/Tuning of Algorithm Performance*

Once MODIS imagery becomes available, there are several aspects of the data that must be examined. After the initialization procedure, with a ship-borne campaign, the imagery must be examined on a regular basis to ensure that the algorithms and the instrument are operating properly. Specifically, the sensor-algorithms should provide the expected "clear water radiances" [Gordon and Clark, "Clear water radiances for atmospheric correction of coastal zone color scanner imagery," *Applied Optics,* **20**, 4175-4180, 1981] in the blue-green region of the spectrum, and should retrieve water-leaving radiances that agree with measurements at the MOBY site [Clark *et al.*, "Validation of Atmospheric Correction over the Oceans," *Jour. Geophys. Res.,* **102D**, 17209-17217, 1997]. Any deviation from expectation or measurement must be reconciled. Deviations could be due to time dependence of the sensor calibration coefficients (i.e., instability in the sensor's radiometric response), improper initialization, improper correction for the sensor's polarization sensitivity, etc. Such analysis of necessity involves a statistical study of the derived water-leaving radiances with sufficient observations to unravel possible effects due to viewing angle, solar zenith angle, and other factors that could influence the retrievals. In addition, the performance of the atmospheric correction algorithm needs to be carefully studied. For example, does the algorithm choose candidate aerosol models that do not vary significantly from pixel to pixel? Such variation could indicate poor performance of the sensor in the NIR. Do the models that are chosen suggest that $\varepsilon(749,869)$ is undergoing a systematic variation with time? Such a variation would indicate that the radiometric response of the sensor is varying in time.

These studies will enable the algorithms to be tuned to the sensor and, in the event of an expected degradation in the sensor response, provide the necessary corrections to the response.

2. *Implement the Initial Algorithm Enhancements*

Several algorithm enhancements are planned for implementation into the processing stream in the immediate post-lanch era. Most of the enhancements focus on dealing with absorbing aerosols, which we consider to be the most important of the unsolved atmospheric correction issues because it has such a significant impact in many geographical areas. They are under intense development now. Among the enhancements we are studying are the spectral matching algorithm (SMA) [Gordon, Du, and Zhang,

"Remote sensing ocean color and aerosol properties: resolving the issue of aerosol absorption," *Applied Optics*, **36**, 8670-8684 (1997)], the spectral optimization algorithm SOA [Chomko and Gordon, "Atmospheric correction of ocean color imagery: Use of the Junge power-law aerosol size distribution with variable refractive index to handle aerosol absorption," *Applied Optics* , **37**, 5560-5572 (1998)], and application of a model of Saharan dust transported over the ocean by the winds that is currently in the testing phase (Moulin *et al.*, in preparation).

The SMA is now being studied extensively because it can be added to the present MODIS algorithm with minor impact, as it uses the same look-up-tables (LUTs) as the existing algorithm. Another attractive feature is that it is completely compatible with our present plans for dealing with wind-blown desert dust. We plan to implement this algorithm in phases. In the first phase, the algorithm will be used to provide a flag that signals the presence of absorbing aerosols. In the second phase, the SMA will actually perform the atmospheric correction and retrieve the ocean products. In the third phase, it will be applied to wind-blown dust. Our goal is to implement all three phases during FY00. A question that needs to be resolved is whether or not the SMA, which employs a semi-analytic model of ocean color [Gordon *et al.*, "A Semi-Analytic Radiance Model of Ocean Color," *Jour. Geophys. Res.*, **93D**, 10909-10924, 1988], is compatible with more sophisticated ocean color models, e.g., Lee *et al.*, "Method to derive ocean absorption coefficients from remote sensing reflectance," *Applied Optics*, **35**, 453—462, 1996.

The SOA is attractive in that it does not require detailed aerosol models to effect atmospheric correction; however, it is unclear as to its efficacy in dealing with wind-blown desert dust which displays absorption that varies strongly with wavelength. The performance of this algorithm will be studied in parallel with the SMA development.

We have implemented in principle our correction for the polarization sensitivity of MODIS [Gordon, Du, and Zhang, "Atmospheric correction of ocean color sensors: analysis of the effects of residual instrument polarization sensitivity," *Applied Optics*, **36**, 6938-6948]. All that is required now is the analysis of the SBRS polarization characterization measurements by MCST. When these become avaliable, they will be added to the code.

Finally, rather than assuming the sea surface is flat for computing the Rayleigh scattering contribution to the top-of-atmosphere reflectance, we have computed it as a function of wind speed. This addition will improve the performance of the algorithm as described in Gordon, "Atmospheric Correction of Ocean Color Imagery in the Earth Observing System Era," *Jour. Geophys. Res.*, **102D**, 17081-17106, 1997.

3. Study Future Enhancements

There are several enhancements that are now in the research phase. The study of these will continue during FY 2000. The two that we consider most important are (1) developing an accurate model of the subsurface upwelling radiance distribution as a function of view angle, sun angle, and pigment concentration, and (2) evaluating the

performance of the SMA and SOA algorithms in the presence of high concentrations of colored dissolved organic matter (CDOM).

Most validation measurements of upwelled spectral radiance (BRDF) in the water are made viewing in the nadir direction. In contrast, ocean color sensors are usually non-nadir viewing. Thus, an important question is how does one validate the sensor performance when the quantity being measured differs from the quantity being sensed? Obviously, one must either correct the validation measurement to the correct viewing angle of the sensor, or correct the sensor observation to what it would be if the view were nadir. Either strategy requires a model of the subsurface radiance distribution. We are using measurements made near the MOBY site to develop such a model. We started using the model of Morel and Gentili ["Diffuse reflectance of oceanic waters. II. Bidirectional aspects," *Applied Optics*, **32**, 6864—6879 (1993)]; however, that model did not agree well with the experimental results. We are now trying to understand the source of the disagreement by examining processes left out of the computation of the radiance distribution, such as instrument self-shadowing and polarization.

The SMA and the SOA identify the presence of absorbing aerosols by using the full spectrum of radiance at the top of the atmosphere (TOA). Typically, absorbing aerosols cause a depression of the TOA radiance in the blue portion of the spectrum. Unfortunately, CDOM in the water leads to a depression in the blue. We are examining the interference of these two effects. Strong interference could limit the usefulness of ocean color sensors in coastal waters where CDOM is high and absorbing aerosols (from urban pollution) are likely to be present.

Once a model of the BRDF is available, we will use it to correct the diffuse transmittance for BRDF effects as described by Yang and Gordon ["Remote sensing of ocean color: Assessment of the water-leaving radiance bidirectional effects on the atmospheric diffuse transmittance," *Applied Optics*, **36**, 7887-7897 (1997)].

We had originally planned to use MODIS Band 26 (1.38 μm) to correct the imagery for the presence of thin cirrus clouds [Gordon, *et al.*, "Effects of stratospheric aerosols and thin cirrus clouds on atmospheric correction of ocean color imagery: Simulations," *Applied Optics*, **36**, 682-697 (1997)]; however, the modification to the algorithm required to deal with strongly absorbing aerosol appear to be incompatible with our original ideas. For the time being we will use Band 26 only to screen for the presence of thin cirrus.

A difficulty that we have noticed with SeaWiFS imagery is poor performance of the atmospheric correction algorithm at large viewing angles (much larger than will be encountered with MODIS). Presumably this is due to the neglect of the curvature of the earth. We will examine the algorithm to see if the curvature needs to be considered for MODIS.

Validation of MODIS Algorithms and Products

Our participation in validation and initialization exercises requires that an array of instrumentation be maintained and fully operational at all times. Furthermore, data analysis skills need to be maintained as well. Personnel for such maintenance are included in our cost estimates.

4. Participate in MODIS Initialization Campaign

Present plans are to have an initialization field campaign within approximately 90 days of the launch of Terra. We will participate in this campaign by providing several data sets: (1) we shall use our whitecap radiometer [K.D. Moore, K.J. Voss, and H.R. Gordon, "Spectral reflectance of whitecaps: Instrumentation, calibration, and performance in coastal waters," *Jour. Atmos. Ocean. Tech.*, **15**, 496-509 (1998)] to measure the augmented reflectance of the water due to the presence of whitecaps; (2) we shall use our radiance distribution camera system (RADS) to measure the BRDF of the subsurface reflectance; (3) we shall employ our micro pulse lidar (MPL) to measure the vertical distribution of the aerosol (of critical importance when absorbing aerosols are present); (4) we shall use our solar aureole cameras and all-sky radiance camera (SkyRADS) to measure the sky radiance distribution to provide the aerosol scattering phase function; and (5) we will measure the aerosol optical depth (AOD). All measurements will be carried out at the station locations with the exception of the MPL which will operate continuously during the campaign. This data will be combined with the data from MOBY to fine tune the sensor and algorithms.

In addition, we will continue to operate our CIMEL station in the Dry Tortugas as part of the Aeronet Network [Holben, *et al*., "AERONET--A federated instrument network and data archive for aerosol characterization," *Remote Sensing of Environment*, **66**. 1-16]. Data from this site will be used to validate MODIS-derived AOD and possibly provide a means to examine the calibration of the near infrared (NIR) spectral bands.

5. Participate in Validation Campaign (SeaWiFS)

We also plan to participate in the pre-launch validation campaign scheduled for October 1999. This campaign will utilize SeaWiFS imagery to validate the MODIS algorithms and processing software. The measurements what we will make are identical to those described above in reference to the MODIS initialization campaign.

RETRIEVAL OF DETACHED COCCOLITH/CALCITE CONCENTRATION

Algorithm Evaluation/Improvement

We are currently putting effort into evaluating the MODIS coccolith algorithm using historical SeaWiFS observations, converted to synthetic MODIS products. Unfortunately, there have been very few observations of major coccolithophore blooms that were adequately sea-truthed, since the launch of SeaWiFS. The most striking of the features has been the Bering Sea coccolithophore bloom of 1997 and 1998. We enumerated field samples at two sites within the feature, and are comparing these to the derived quantities using the synthetic MODIS product. Our aim over the next year will be to examine other such features that have corresponding sea-truth data. For example, there have been numerous coccolithophore blooms off of the European continental shelf, which were sampled by personnel from the Plymouth Marine Laboratory, (Plymouth, U.K.). We will request coccolith concentration data from these investigators, for comparison with the satellite-derived coccolith concentrations. Moreover, we routinely have been working in the Gulf of Maine, measuring optical properties, enumerating coccolith concentrations, and measuring suspended calcite. These cruises have traversed some relatively coccolith-rich areas (while still considered "non-bloom" they nevertheless should be above the noise threshold of the algorithm).

We have had to change analytical facilities for processing our calcite samples due to non-availability of the previous graphite furnace atomic absorption spectrometer that we were using. We are now working with the Scripps Institution Of Oceanography Analytical Facility, which has an Inductively Coupled Plasma Optical Emission Spectrometer (ICPOES). This instrument is more sensitive than a graphite furnace atomic absorption spectrometer for an equally sized sample. Before they can process our complete set of samples, however, they must first run blanks, and verify proper signal to noise for test samples (happening now). In late September, we will be sending them all unprocessed samples from the Gulf of Maine. Following receipt of the data, we will then collate all data sets that we have for the Gulf of Maine, from 1996 to present, as well as other data that we have collected from the North Atlantic, Caribbean, and Arabian Sea, for revision of the "mean" backscattering versus suspended calcite relationship. This data set would be the largest of its kind available, and the validated relationship will allow significant improvement in the MODIS algorithm code.

Validation of MODIS Algorithms and Products

We are maintaining an active cruise schedule in the Gulf of Maine aboard the ship of opportunity, the passenger ferry m/s *Scotia Prince*. By the end of October, we will have 20 trips for 1999, with 10 more planned for the year 2000. We will make application to continue these trips into upcoming years. These data sets are still being examined, and calcite concentrations are being determined. We also participated in an eight-day cruise to the Gulf of Maine during June and July of this year, aboard the r/v Edwin Linke. These data will be processed over the upcoming months. These trips all have had an above-water radiometer recording upwelling radiance at 40 Deg. from nadir, at the SeaWiFS wavelengths. We will apply the coccolithophore algorithm to these data, for additional validation when satellite coverage is not available. Lastly, we are in the planning stages for a Navy funded experiment to sample the N. Atlantic coccolithophore bloom (ideally this would be during June/July 2001). If funded, this will provide probably the best opportunity for validating the MODIS coccolith algorithm.

MODIS Baseline Spending Plan FY00

The table on the next page delineates the cost to the project on a monthly basis. Travel and shipping have been computed on the following assumptions: (1) we will continue to maintain and operate the AERONET site on the Dry Tortugas at a cost of $600 per month; (2) because of the launch of Terra we have budgeted for four Science Team Meetings (Nov., May, July, Sept.); (3) we plan to send at least one group member to deliver papers at the Fall AGU Meeting, the Ocean Sciences Meeting (Jan.), AGU 2000 (May), and IGARRS 2000 (July); and (4) the MODIS initialization cruise will take place in the March-April time frame. The October cruise costs (travel and shipping) have been included as FY99 costs, i.e., they are reflected in the FY99 carryover. “Communication” included publication page charges. “Maintenance” refers to both hardware and software maintenance of computers. “Subcontracts” refers to the subcontract to Bigelow Laboratory for Ocean Sciences for carrying out the coccolithophore studies. “Capital” refers to procurement of additional mass storage capacity (both increasing the number of disk drives or upgrading low-capacity drives with high-capacity drives) of our Team Member Computer Facility.

APPENDIX II

MODIS Atmospheric Correction Performance: Initial Evaluation

Howard R. Gordon
University of Miami

With significant help from K. Turpie, R. Vogel, B. Franz, R. Evans, J. Brown, W. Esaias, MODIS SDST and MCST.

Preamble

In this appendix we describe an initial evaluation of the performance of MODIS and the atmospheric correction algorithm based on a single MODIS granual (2000102.2215) that covers an area in the Central Pacific from approximately 0–20 Deg. South and 147–172 Deg. West. First, a simplified version of the atmospheric correction algorithm is presented. Next, the retrieved normalized water-leaving radiance at 551 nm is evaluated. Then, the performance of the MODIS atmospheric correction bands is examined. Finally, preliminary conclusions are presented.

Atmospheric correction review

The atmospheric correction algorithm for MODIS is based on the work of Gordon and Wang (1994). Improvements and unresolved problems concerning the MODIS algorithm have been described in detail by Gordon (1997). The algorithm uses the MODIS near infrared bands (15 and 16 at 749 and 869 nm, respectively) to assess the aerosol contribution in the visible. To understand the analysis that follows, a brief and simplified description of the correction algorithm is provided below.

We convert all radiances to reflectance defined by

$$\rho = \frac{\pi L}{F_0 \cos\theta_0},$$

where L is radiance, F_0 is the extraterrestrial solar irradiance, and θ_0 is the solar zenith angle. Then the reflectance measured at the top of the atmosphere (TOA), ρ_t, is given by

$$\rho_t(\lambda) = \rho_r(\lambda) + \underbrace{\rho_a(\lambda) + \rho_{ra}(\lambda)}_{\rho_A(\lambda)} + t_0(\lambda)t_v(\lambda)n\rho_w(\lambda),$$

where ρ_r is the contribution from molecular (Rayleigh) scattering in the absence of aerosols, ρ_a the contribution from the aerosol in the absence of air, ρ_{ra} the contribution from interactive Rayleigh and aerosol scattering, and $n\rho_w$ is the normalized water-leaving reflectance. The quantities t_0 and t_v are the diffuse transmittances in directions from sea surface toward the sun and from the sea surface toward the sensor, respectively. The Rayleigh contribution can be computed from an estimate of the surface atmospheric pressure (provided in the ancillary data from NOAA). In the NIR $n\rho_w \approx 0$, which allows determination of ρ_A there. The atmospheric correction parameter $\varepsilon(\lambda,\lambda_0)$ is approximately given by

$$\varepsilon(\lambda,\lambda_0) \approx \frac{\rho_A(\lambda)}{\rho_A(\lambda_0)}$$

(see Gordon 1997 for a more precise definition), so in the NIR $\varepsilon(\lambda,\lambda_0)$, can be determined for λ and λ_0 representative of Bands 15 and 16, i.e.,

$$\varepsilon(15,16) \approx \frac{\rho_A(15)}{\rho_A(16)}.$$

For the other bands, we estimate $\varepsilon(\lambda,16)$ from $\varepsilon(15,16)$ using a set of candidate aerosol models. Then the water-leaving reflectance in any band can be estimated from

$$n\rho_W(\lambda) = t_0{}^{-1}(\lambda)t_V{}^{-1}(\lambda)\{\rho_t(\lambda) - \rho_r(\lambda) - \varepsilon(\lambda,16)[\rho_t(16) - \rho_r(16)]\},$$

with the diffuse transmittances being determined from the chosen candidate aerosol model and the aerosol concentration (found from $\rho_A(16)$).

To look at the performance of the atmospheric correction algorithm we examined the retrieved normalized water-leaving radiance at 551 nm $nL_w(551)$ and the retrieved $\varepsilon(15,16)$ from MODIS granual 2000102.2115. We chose to look at $nL_w(\lambda)$ at 551 nm because the value of $nL_w(551)$ is almost independent of the chlorophyll concentration if it is less than about 0.25 mg/m^3, and has a nominal value of approximately 2.8 W/m^2 μm Sr, and (Gordon and Clark, 1981). Also, in typical maritime atmospheres, $nL_w(551)$ comprises only about 5% of $L_t(551)$. We discuss $nL_w(551)$ first.

Retrieved *$nL_w(551)$* evaluation

Figure 1 is an image of $nL_w(551)$ produced at Goddard using the MODIS Ocean processing code and the post-launch radiometric calibration (March 17) that was based on observations of the solar diffuser. Periodic banding is evident in the imagery, and is caused by the fact that the ten detectors that individually record a scan are not properly calibrated in a relative sense. (Such a calibration is usually referred to as "flat fielding.") In this figure the line numbers are arranged from 1 at the bottom (southern edge) of the image to ~ 2000 at the top (northern edge), and the pixel numbers range from 1 (western) at the left edge to 1354 at the right (eastern) edge. Lines of constant pixel number correspond to a constant scan angle and a constant angle of incidence (AOI) on the scan mirror, but employ all 10 detectors. In contrast, along a single scan line, only one detector is employed, but all (earth scan) angles of incidence on the scan mirror are used. Figures 2 provide the actual values of $nL_w(551)$ extracted from the L2 product along a line of constant pixel number (Figure 2(a) from the vertical line in Figure 1(a)) and constant line number (Figure 2(b) from the horizontal line in Figure 1(a)). The large excursions of $nL_w(551)$ from the background ~ 4.2 W/m^2 μm Sr mean are due to data that have been corrupted by clouds. The small excursions are the result of a systematic change in the radiometric characteristics of the individual detectors in the track direction,

which we refer to as "banding" or "striping." The banding evident in Figure 1(a) is further quantified in the Figure 3, and very evident in an expanded version of the image (Figure 1(b)). Figure 3, shows that the banding appears to be due primarily to a single detector. The general level of $nL_w(551)$ is ~4.0-4.5 W/m^2 μm Sr, i.e., about 50% too high. Figure 2(b) shows that there appears to be a regular variation of $nL_w(551)$ with scan angle, i.e., $nL_w(551)$ is larger at the edges of the scan than at the center. This is likely due in part to an overall system calibration error in this band, but it could also result from an uncorrected variation of the MODIS system response as a function of the scan angle.

A new version of the processing code was produced in which errors in the original code were corrected, and $\varepsilon(15,16)$ was estimated using a 3×3 pixel average rather than individually to reduce noise (see $\varepsilon(15,16)$ discussion below). Imagery processed at the University of Miami using this new code version with the L1B data still showed significant banding (Figure 4), but the overall level of $nL_w(551)$ was reduced to ~ 3.0-3.5 W/m^{2}μm Sr, closer to the expected 2.8 W/m^{2}μm Sr. Figure 4(b) also shows that the banding now appears to be more of a ramp or linear trend (linear increase in radiance with detector number) rather than a higher radiance from a single detector (Figure 3). Comparison of Figure 4(a) with Figure 2(a) shows that the $\varepsilon(15,16)$-averaging procedure magnifies the influence of clouds. This is because a small cloud anywhere in the 3×3 pixel box will corrupt the results. The variation of $nL_w(551)$ across the scan using the corrected code still exhibits some variation; however, because of the increased cloud corruption (compare Figures 2(a) and 4(a)) it is difficult to assess with this image.

Finally, Figure 5 shows along track retrieval of $nL_w(551)$ using the University of Miami empirical calibration adjustments. With this calibration the overall level is now ~3.3-3.5 W/m^{2}μm Sr, but the periodic banding is not as evident.

Retrieved $\varepsilon(15,16)$ evaluation

Much of the striping seen in $nL_w(551)$ is evident in the L1B data, i.e., $L_t(551)$. However, we need to know how much, if any, of the banding is due to the atmospheric correction process. For this we examined the behavior of $\varepsilon(15,16)$ for this image. Figure 6 provides the observed values of $\varepsilon(15,16)$ and the retrieved aerosol optical thickness at 869 nm, $\tau_a(869)$, for the along track (Figure 6(a)) and along scan (Figure 6(b)) directions of the image in Figure 1. The most obvious observation to be made from these figures is that the observed values of $\varepsilon(15,16)$ are quite noisy, and in the scan direction (Figure 6(b)) the behavior of $\tau_a(869)$ shows that the sun glint centered near pixel 900 extends significantly beyond the area that has been masked as sun glint (pixels 745—935). Clearly, the sun glint is being interpreted as aerosol by the algorithm. This shows that a large portion of the scan is unusable (pixels 600—1354) for this scan line that is at approximately 10 degrees south of the Equator.

Figure 7 shows $\varepsilon(15,16)$ for a small section of the track-direction line from lines 250 to 600 that is relatively free of clouds. As mentioned earlier, this indicates that $\varepsilon(15,16)$ is noisy, but the noise does not appear to be systematic. One expects that, since $\varepsilon(15,16)$

depends mostly on the aerosol size distribution and should be independent of the aerosol concentration, it would be essentially constant, at least over distances ~ few hundred km in this region of the ocean (far from terrestrial and anthropogenic sources). The noise we observe must be sensor generated. The red line on the figure provides the value of $\varepsilon(15,16)$ for the same detector, i.e., it is the value for every 10^{th} line. In addition each data point applies to the same AOI on the scan mirror. Thus, the noise does not appear to be related to calibration. We tried to understand the source of this noise in the following manner. Figure 6(a) shows that in this region, $\tau_a(869) \approx 0.1$. For this value of $\tau_a(869)$ and a typical marine aerosol (the Shettle and Fenn (1979) maritime aerosol model with a relative humidity of 80%, and referred to as M80) the characteristic values of the reflectances in the NIR are provided in Table 1.

Table 1: Characteristic Values (M80)(θ_0=0, θ_v=45°)

Band	ρ_t	ρ_r	$\rho_a + \rho_{ra}$
15	0.017759	0.010964	0.006795
16	0.013219	0.006648	0.006574

For these values, the expected value of $\varepsilon(15,16) \approx 0.006795/0.006574 = 1.0336$. Using the measured SNR's we can compute the expected noise in ρ_t. This is provided in Table 2.

Table 2: Expected noise in ρ_t

Band	SNR	$\Delta(\rho_t)$
15	800	2.22×10^{-5}
16	700	1.88×10^{-5}

Thus, we can compute a worst-case estimate of the expected noise in $\varepsilon(15,16)$ by assuming maximum excursions of $\Delta(\rho_t)$ in the two bands, but with opposite sign, i.e., the upper excursion of $\varepsilon(15,16)$ would be

$$\varepsilon(15,16)^{+} = \frac{\rho_a(15) + \rho_{ra}(15) + \Delta\rho_t(15)}{\rho_a(16) + \rho_{ra}(16) - \Delta\rho_t(16)} = 1.0398,$$

while the lower excursion is

$$\varepsilon(15,16)^{-} = \frac{\rho_a(15) + \rho_{ra}(15) - \Delta\rho_t(15)}{\rho_a(16) + \rho_{ra}(16) + \Delta\rho_t(16)} = 1.0274.$$

The maximum amount of expected noise (peak-to-peak) should not exceed $\Delta\varepsilon(15,16) = \varepsilon(15,16)^{+} - \varepsilon(15,16)^{-} \approx 0.012$. Halving the value of $\tau_a(869)$ would approximately double $\Delta\varepsilon(15,16)$. The actual noise appears to be significantly in excess of these computed values of $\Delta\varepsilon(15,16)$. We do not know the source of this additional noise. To reduce the importance of this noise, we have modified the processing code so that the value of

$\varepsilon(15,16)$ is estimated by averaging the values of ρ_t in the NIR over a 3×3 pixel box around the pixel being processed. However, the value of $\rho_t(16)$ at the actual pixel is used in computing $n\rho_w(\lambda)$. Unfortunately this averaging procedure will increase the number of pixels that are corrupted by clouds.

Conclusions

Based on the above analysis of granual 2000102.2215, we make the following conclusions:

- The overall the retrieved water-leaving radiances on the average are in the correct ranges, suggesting that the overall system calibration and the atmospheric correction are in the nominal ranges; however, when the imagery is evaluated at full resolution many artifacts are apparent.

- The initial normalized water-leaving radiance at 551 nm, $nL_w(551)$, showed severe striping (a maximum of about 10% over the 10 detectors in the spectral band) normal to the subsatellite track, and the average value is ~ 50% too high.

- After correcting errors and omissions in the processing codes, and reprocessing the granual at Miami, this error in the average $nL_w(551)$ was reduced to ~ +10%; however, the striping in $nL_w(551)$ remained.

- After an initial attempt by R. Evans and co-workers at flat fielding the imagery, the strongly periodic nature of the striping was removed, but there was still some striping.

- The retrieved $nL_w(551)$ across a scan line showed some limb brightening that could be due to overall calibration errors or to the influence of an unaccounted variability in the system response as a function of scan angle.

- Bands 15 or 16, or both, (used for atmospheric correction) appear to display excessive noise. This may require averaging the atmospheric correction parameter $\varepsilon(15,16)$ over several pixels.

- Sun glint will likely render the eastern half of the scan useless in the tropics unless a correction scheme can be developed.

- The striping in $nL_w(551)$ is not due to atmospheric correction, as $\varepsilon(15,16)$ does not show significant striping.

In addition, it seems reasonable to conclude that

- a significant amount of work will be required to removing the striping from the MODIS derived products, as its root cause is probably spread over several processes, e.g., instrument polarization sensitivity, variability in system response with scan angle, etc. Thus the improvement process will require an incremental resolution and balancing of the individual effects, and

- plans should be made to reprocess MODIS imagery as incremental progress is made.

References

H.R. Gordon and D.K. Clark, Clear water radiances for atmospheric correction of Coastal Zone Color Scanner imagery, *Applied Optics*, **20**, 4175-4180 (1981).

H.R. Gordon and M. Wang, Retrieval of water-leaving radiance and aerosol optical thickness over the oceans with SeaWiFS: A preliminary algorithm, *Applied Optics*, **33**, 443-452 (1994).

H.R. Gordon, Atmospheric Correction of Ocean Color Imagery in the Earth Observing System Era, *Jour. Geophys. Res.*, **102D**, 17081-17106 (1997).

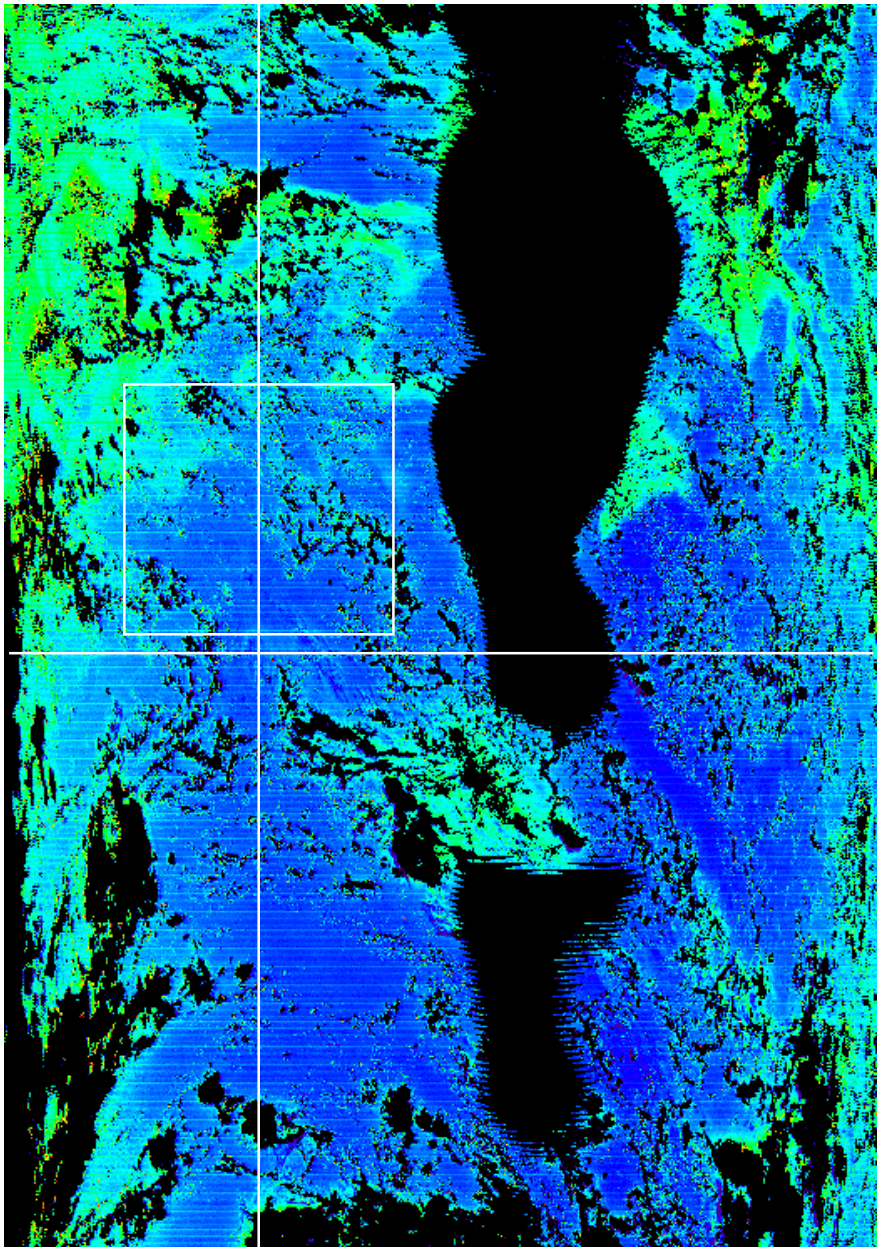

Figure 1(a). Retrieval of $nL_w(551)$ from MODIS granual 20001022115. The subimage in the box is shown in Figure 1(b). Extractions of values are taken along the vertical line(track direction) and the horizontal line (scan direction). The black area through the center is the portion masked for sun glint.

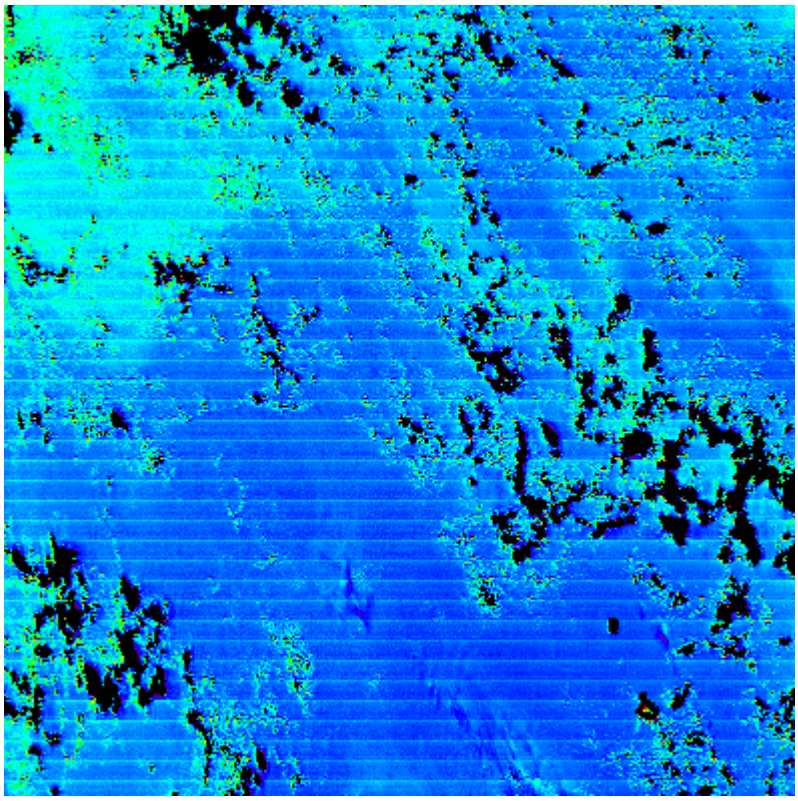

Figure 1(b): Subimage of $nL_w(551)$ from MODIS granual 20001022115 from the box drawn on Figure 1(a).

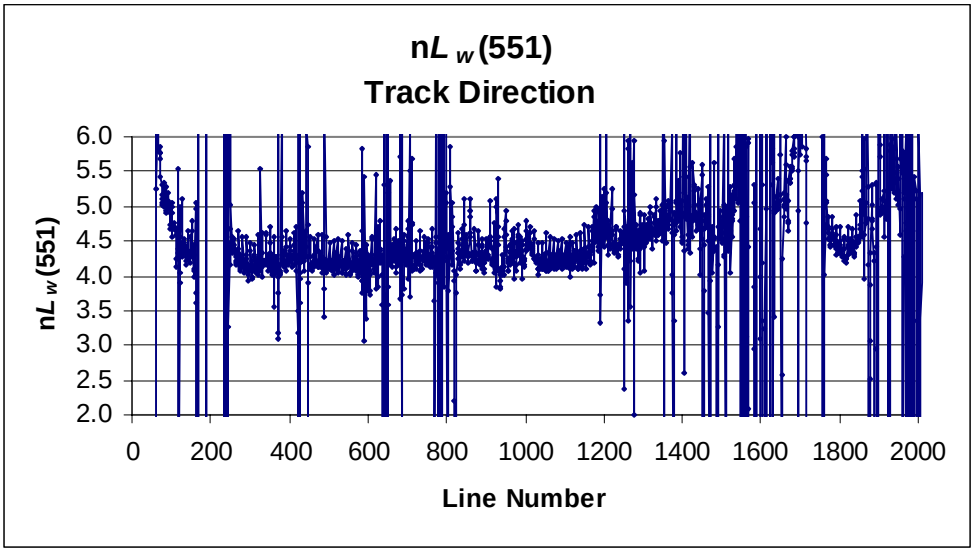

(a)

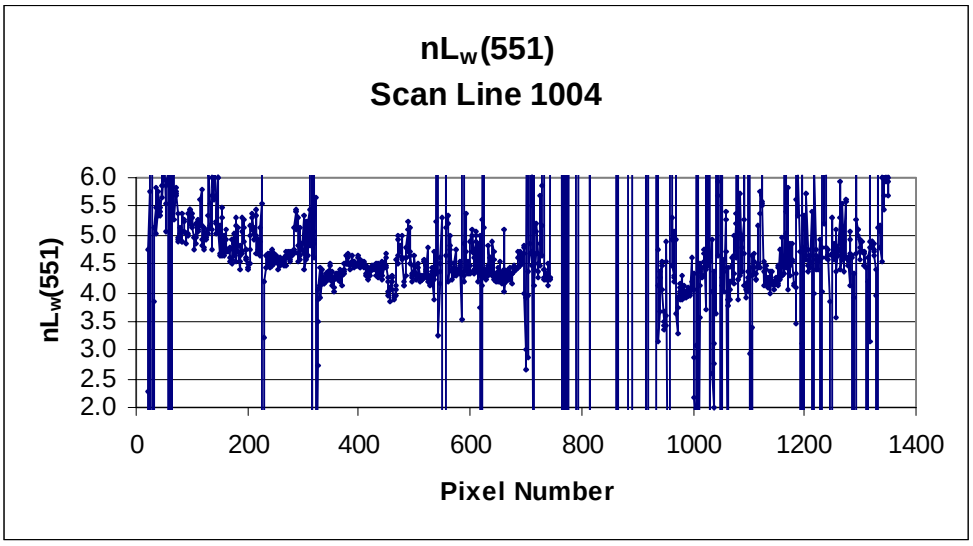

(b)

Figure 2. Extracted values of nLw(551) in W/m^{2}µm Sr, along the track (a) and scan (b) directions on the lines shown in Figure 1(a).

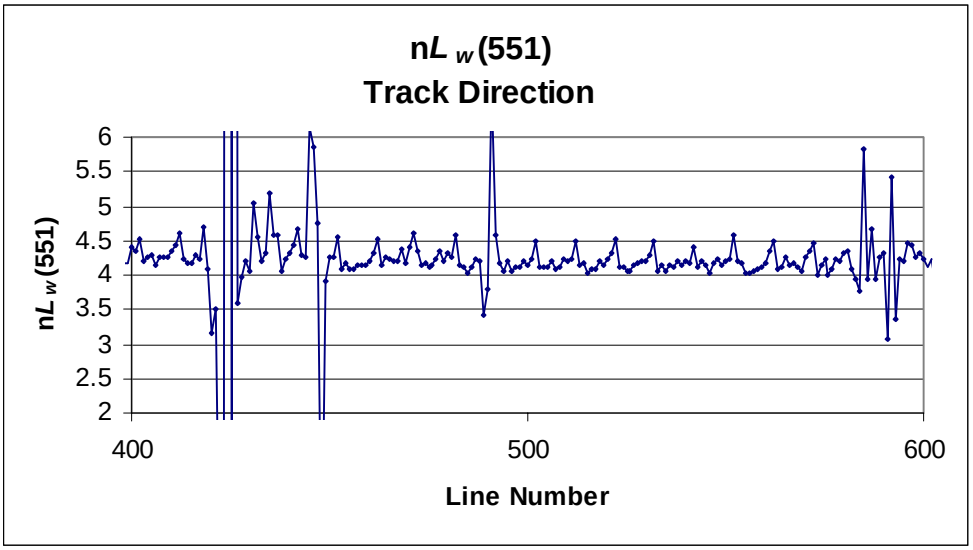

Figure 3. Expanded version of Figure 2(a) from line 400 to line 600.

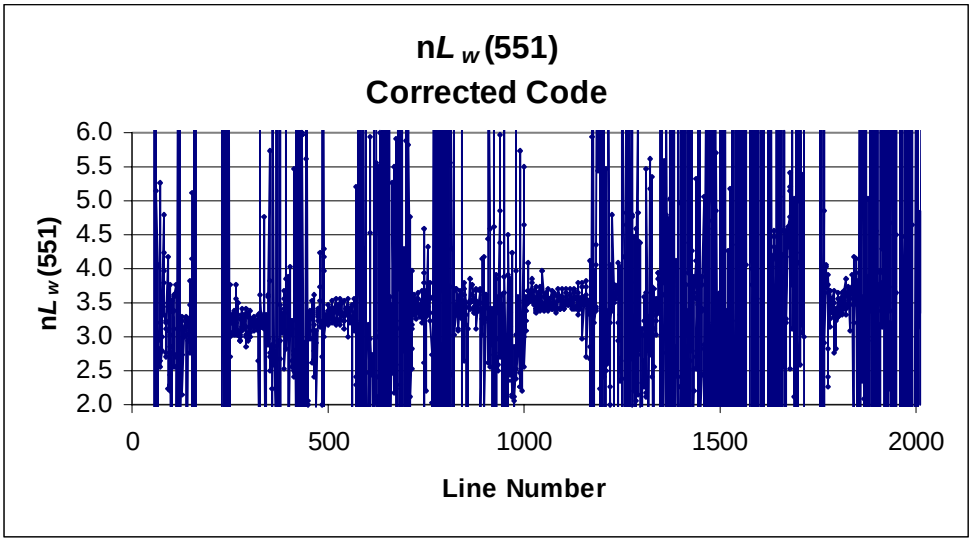

(a)

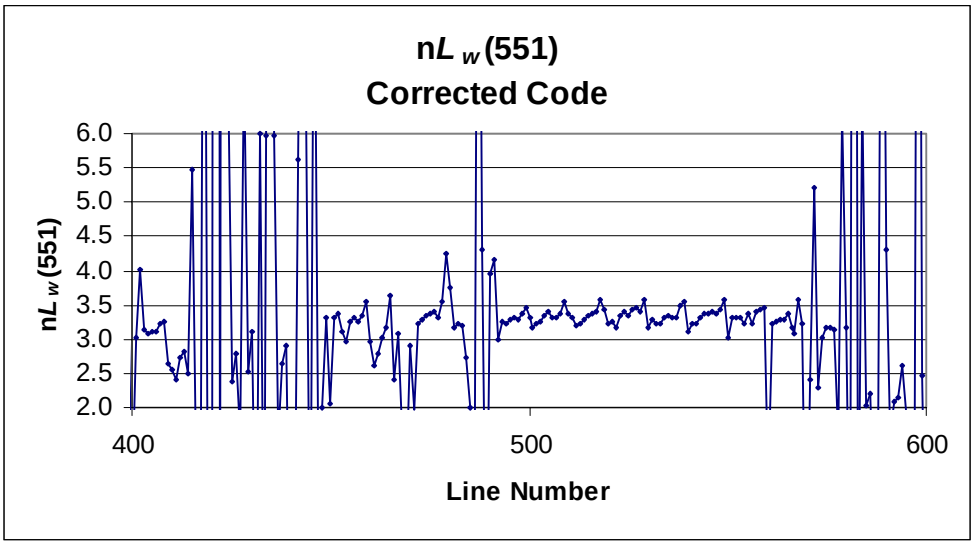

(b)

Figure 4. Extracted values of nLw(551) in W/m^{2}µm Sr, along the track direction shown in Figure 1(a), with the corrected processing code.

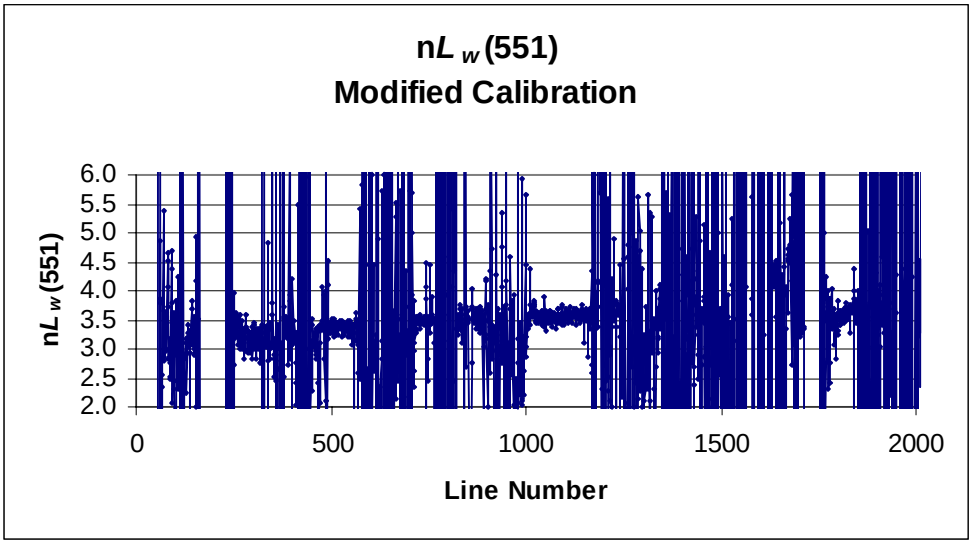

(a)

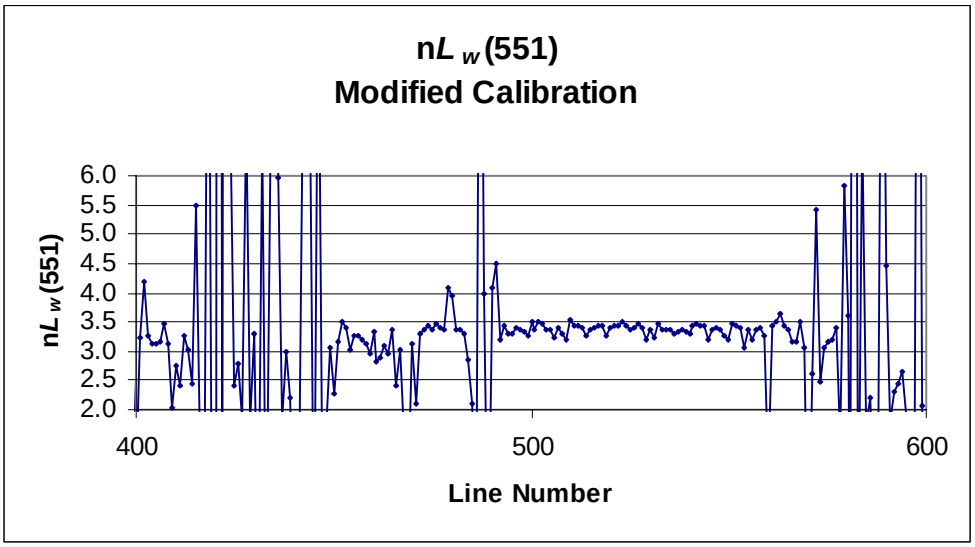

(b)

Figure 5. Extracted values of nLw(551) in W/m^{2}µm Sr, along the track direction shown in Figure 1(a), with the corrected processing code, and a modified calibration to try to reduce the striping.

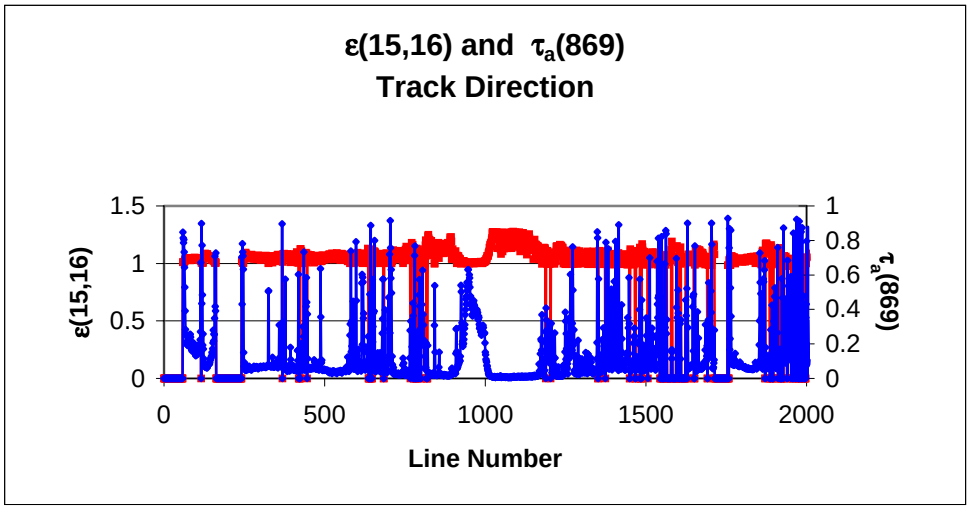

(a)

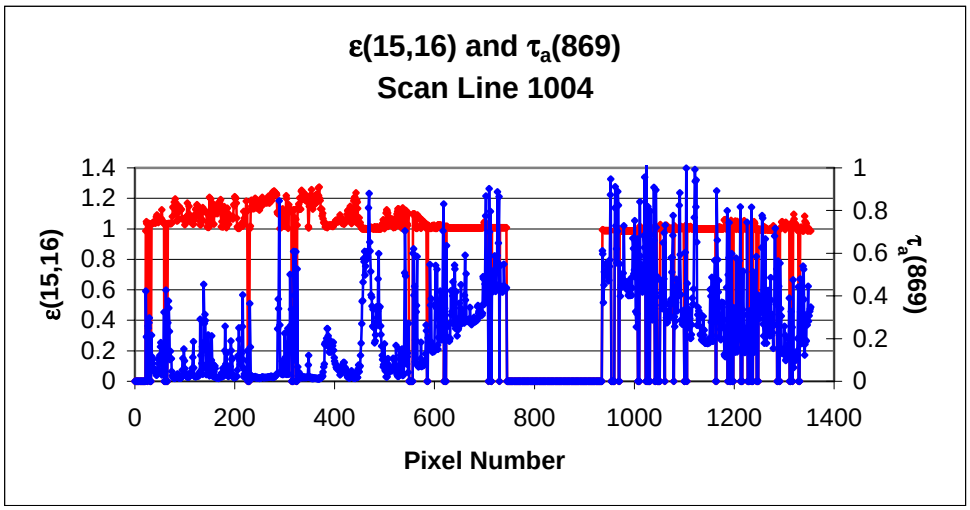

(b)

Figure 6. Variation of $\varepsilon(15,16)$ (upper, red curve) and $\tau_a(869)$ (lower, blue curve) along the track (a) and scan (b) directions shown in Figure 1(a).

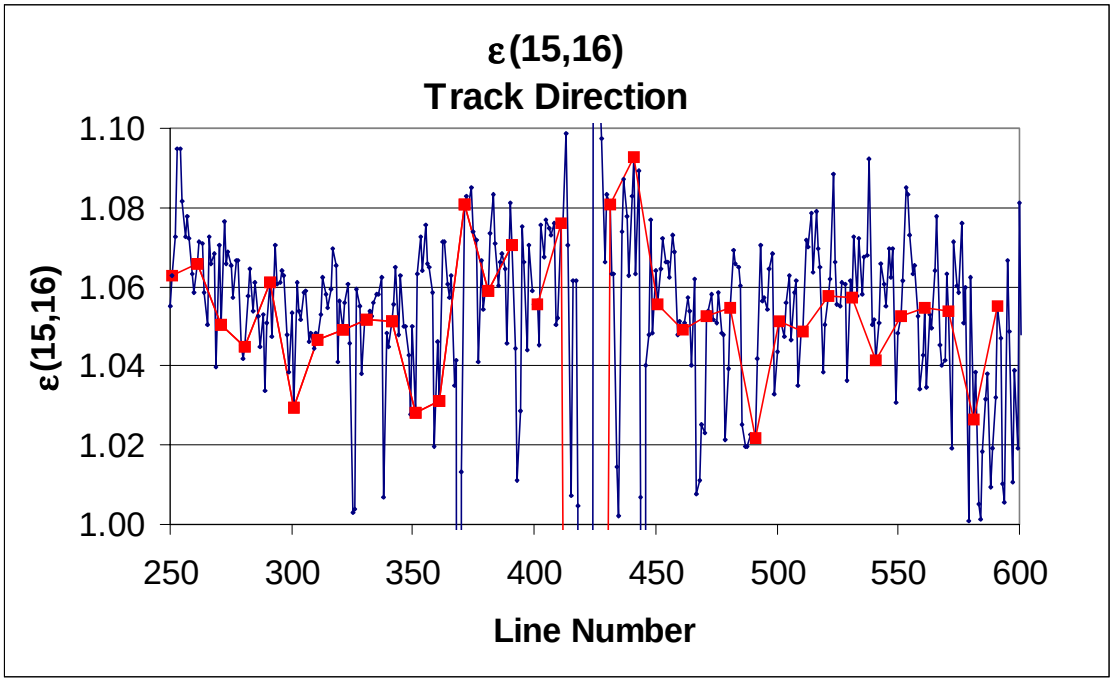

Figure 7. Expanded portion of Figure 6(a). The red line connects every tenth line and therefore corresponds to a single detector and a single AOI on the scan mirror.

Appendix III

Atmospheric correction of ocean color imagery through thick layers of Saharan dust

(Submitted to *Geophysical Research Letters*)

ATMOSPHERIC CORRECTION OF OCEAN COLOR IMAGERY THROUGH THICK LAYERS OF SAHARAN DUST

C. Moulin[1,2], H. R. Gordon[1], R. M. Chomko[1], V. F. Banzon[1,3], and R. H. Evans[3]

[1]Physics Department, UM, Coral Gables, Florida, USA

[2]Lab. des Sciences du Climat et de l'Environnement, CEA-CNRS, Gif-Sur-Yvette, France

[3]Rosenstiel School of Marine and Atmospheric Science, UM, Miami, Florida, USA

ABSTRACT

Airborne plumes of desert dust from North Africa are observable all year on satellite images over the Tropical Atlantic. In addition to its radiative impact, it has been suggested that this mineral dust has a substantial influence on the marine productivity. This effect is however difficult to gauge because present atmospheric correction algorithms for ocean color sensors are not capable of handling absorbing mineral dust. We apply a new approach to atmospheric correction in which the atmosphere is removed and the case 1 water properties are derived simultaneously. Analysis of SeaWiFS images acquired off Western Africa during a dust storm demonstrates the efficacy of this approach in terms of increased coverage and more reliable pigment retrievals.

INTRODUCTION

Phytoplankton, the first link in the marine food chain, can be detected from above the sea surface through the change in water color brought about by virtue of the photosynthetic pigment chlorophyll *a* and various accessory pigments they contain that absorb strongly in the blue portion of the spectrum. The seminal CZCS mission demonstrated that these color variations

could be measured from satellite altitudes [Gordon *et al.* 1980] and led to the launching of several new ocean color sensors, SeaWiFS, MODIS, POLDER, etc.

Of the radiance measured by an in-orbit ocean color sensor (L_t) only a small portion (L_w) exited the ocean, typically < 10% in the blue, less at longer wavelengths, and negligible in the near infrared (NIR). The rest is radiance backscattered from the atmosphere and reflected by the sea surface. This radiance must be removed from L_t (atmospheric correction) in order to retrieve L_w, the only part that contains information regarding marine productivity. The principal difficulty in atmospheric correction lies in removing the effects of aerosols.

Assessment of the aerosol is now effected in a similar manner for all present ocean color sensors (e.g., Gordon and Wang [1994] for SeaWiFS). Aerosol is detected in two NIR bands and the observed spectral variation is compared to that of a set of aerosol models. The most appropriate are then used to remove the aerosol's contribution from L_t in the visible. Such algorithms are presently being successfully applied, except when the aerosol is strongly absorbing, because the aerosol's absorption is not detectable from the observed spectral variation in the NIR [Gordon 1997]. Standard atmospheric correction in the presence of absorbing particles thus underestimates L_w in the blue leading to too-high pigment concentrations.

The predominant absorbing aerosol in the marine atmosphere is the mineral dust coming from the Sahara [Herman *et al.* 1997]. This dust is strongly absorbing in the blue because it contains ferrous minerals [Patterson 1981]. In addition, the impact of this absorption is very dependent on the vertical distribution of the aerosol [Gordon 1997]. This is of primary importance for Saharan dust [Moulin *et al.* 2000]. Because of these difficulties, the present algorithms do not process pixels when high L_t are detected in the NIR. The quasi-permanent presence of dust degrades satellite ocean color products in the Tropical Atlantic where large

areas are not sampled, sometimes for as long as an entire month. This failure of the atmospheric correction also prevents observation of the potential fertilization effect due to the supply of nutrients contained in dust to the surface water [Young *et al.* 1991].

RETRIEVAL ALGORITHM

Our approach to atmospheric correction in the dust zone is the spectral matching algorithm (SMA) proposed by Gordon *et al.* [1997]. Briefly, a set of N candidate aerosol models is used along with a model of the water-leaving radiance as a function of the pigment concentration C and a marine particle-scattering parameter b^0 [Gordon *et al.* 1988]. In this context, an aerosol model is comprised of a particle size distribution and index of refraction, with the radiative properties computed using Mie theory, and a vertical distribution of aerosol concentration. C is defined to be the sum of the concentrations of chlorophyll *a* and its degradation product phaeophytin *a*. It is the bio-optical quantity that was estimated by the CZCS. The Gordon et al. [1988] radiance model was tuned to C using in-situ measurements in case 1 waters in the Eastern Pacific, Gulf of California, Western Atlantic, and Gulf of Mexico.

The aerosol optical depth (AOD) for each aerosol model is adjusted so that the computed top-of-atmosphere (TOA) radiance for the given model exactly reproduces the measured value in the NIR. This allows the contribution of the atmosphere to the TOA radiance to be computed throughout the visible for each aerosol model. The marine contribution for a given C and b^0 is then added to the atmospheric contribution for each of the N models to provide the modeled TOA radiance throughout the visible. For each aerosol model, we then systematically varied C (17 values, from 0.03 to 3 mg/m^3) and b^0 (12 values, from 0.12 to 0.45) over the range characteristic of Case 1 waters to obtain the best agreement, in an root-mean square (RMS) sense, between the modeled and measured TOA radiances at all wavelengths.

Realistic aerosol models are crucial for obtaining accurate estimates for the ocean properties using this approach. We used the set of mineral dust models of Moulin et al. [2000] which is based on earlier work with Meteosat [Moulin et al. 1997]. Comparisons between in-situ and Meteosat-retrieved *AOD* showed that the Shettle [1984] "Background Desert" model was superior to a wide range of other models. The real part of the aerosol's refractive index was set to 1.53 and its imaginary part was set after Patterson [1981]. This provided the basic model from which a set of 18 candidate dust models was developed by using three contributions of the coarse mode to the size distribution, two spectral variations of the absorption index (Patterson's and a lower limit set by examination of several SeaWiFS images), and three thicknesses of the dust layer [Moulin et al. 2000].

We applied the SMA to SeaWiFS on a pixel-by-pixel basis. Since the cloud screening of the standard algorithm removed most of the bright "dusty" pixels, we decided to replace it by a threshold on the standard deviation of the TOA radiance at 865 nm computed on 3x3 pixels [Moulin et al. 1997]. This threshold was set by trial and error to 0.5 $mW/cm^2\mu mSr$. It produces a more conservative, and we believe better, cloud screen than that of the standard algorithm. For the non-cloudy pixels that were then processed using the SMA, we do not report the retrieved pigment concentration when the retrieved *AOD* is greater than 0.8.

SAMPLE RESULTS

We applied the SMA along with the University of Miami implementation of the standard SeaWiFS algorithm to an 8-day period acquired off the West Coast of Africa between September 30th and October 7th, 1997. This time period was chosen because it enables comparison with the standard SeaWiFS 8-day product. During this period, 5 SeaWiFS orbits (October 1st, 3rd, 4th, 5th and 7th) crossed our region of interest (10-30°N; 10-25°W). An intense dust event, shown in

Figure 1, is observable between 10°N and 20°N on all orbits during this period, obscuring the signal from the sea surface. The most interesting region to test our improved atmospheric correction is between 15°N and 20°N where the mean *AOD* ranges mainly from 0.2 to 0.8 since we expect the standard atmospheric correction to be degraded even for relatively low *AOD*. North of the dust zone, between 20°N and 30°N, *AOD* remain low (≤ 0.1) during the period.

Figure 2 provides a comparison of the retrieved pigment concentrations from the SMA and the standard SeaWiFS (STD) chlorophyll product of single orbit retrievals for the nearest "non-dusty" day (September 29th) outside of the dust event. During this clear day, the *AOD* was about 0.1 over the whole region, so that the retrieved pigment concentrations can be used as a reference to describe the actual marine productivity of this entire region. The STD chlorophyll product uses the algorithms of Gordon and Wang [1994] for atmospheric correction and of O'Reilly *et al.* [1997] (OC2) for retrieving the chlorophyll concentration from L_w. In contrast to the Gordon *et al.* [1988] model that was tuned to pigment concentration, the O'Reilly et al. [1997] algorithm is an empirical fit to chlorophyll *a*. *C* is approximately 35% greater than the concentration of chlorophyll *a* [O'Reilly *et al.*, 1997]; however, for the same water-leaving radiances the Gordon et al. [1988] pigment concentration and the O'Reilly et al. [1997] chlorophyll *a* can differ as much as a factor of two, with *C* even lower than chlorophyll *a* over some of the range. Rather than trying to reconcile the existing differences between these two bio-optical algorithms, we decided that for atmospheric correction purposes it is sufficient to compare the pigment concentration from the SMA to the chlorophyll *a* concentration from the STD processing.

At the regional scale, it is obvious that both algorithms lead to very similar results for oligotrophic waters as well as for the very productive Mauritanian upwelling. Indeed, even though the aerosol models used to perform the atmospheric correction are completely different

(i.e., weakly- or non-absorbing for STD and absorbing for SMA), the aerosol contribution to the TOA radiance is small enough so that it does not significantly influence the pigment retrievals. A more detailed analysis however reveals some discrepancies between the two results that are likely due to the difference in the derived product (chlorophyll *a* for STD and pigment for SMA), as well as the bio-optical models used to estimate the pigment concentration from L_w. For instance, there is an overestimate of the pigment concentration compared to chlorophyll *a* in areas between 25°W and 23°W at about 20°N, and between 19°W and 16°W at about 17°N. In the case 2 waters along the African coast at about 20°N, the SMA retrieves very low pigment concentrations because it is based on the case 1 water model of Gordon et al. [1988]. Also, one should note that the maximum pigment concentration that can be reached within our SMA for case 1 waters is 3 mg/m^3, whereas the O'Reilly et al. [1997] empirical algorithm is designed to retrieve chlorophyll *a* concentrations as high as 30 mg/m^3. Despite these differences, the general agreement between the two results is satisfactory for this dust-free image.

Figure 3 shows single orbit retrievals of the pigment concentration for two "dusty" days (October 3rd and 5th). Contrary to what was shown in Figure 2, the two algorithms lead to very different results. The continuity of the SMA algorithm between the two dusty days and the clear day in Figure 2 suggests that it has been successful in removing much of the influence of the dust from the October 3rd and 5th images. In contrast, the standard algorithm shows very high chlorophyll concentrations in the edge of the dust plume, but it retrieves reasonable concentrations away from the plume, although comparison with Figure 2 shows that the STD algorithm returns higher values north of 25°N. This cannot be due to a difference of bio-optical algorithm, but rather to low concentrations of dust. In contrast, the SMA retrieves essentially the same pigment concentration in this region on all three days.

We computed the corresponding concentration means of non-cloudy pixels for the 8-day period from September 30th to October 7th. Both the SMA pigment and the SeaWiFS standard chlorophyll *a* product (acquired from the NASA/GSFC web site) are shown on Figure 4. It is evident that the SMA yields significantly more coverage in the dust region between13°N and 18°N. Furthermore, in the region between 10°N and 13°N, the STD algorithm actually processes the imagery, but yields concentrations that are much too high (compare Figure 4 with Figure 2). Above 25°N, the STD concentrations are also slightly too high, presumably because of a background of dust. In contrast, over most of the area studied, the SMA retrieves approximately the same pigment concentrations over the eight days as it did in the absence of dust (see Figure 2). This suggests that the SMA provides significantly better pigment retrievals and spatial coverage than the STD does in producing the standard SeaWiFS chlorophyll product.

CONCLUDING REMARKS

We have applied an algorithm, developed for atmospheric correction of ocean color imagery in strongly absorbing atmospheres, to SeaWiFS imagery acquired in the region of Saharan dust transport off the coast of Africa. Application required a set of candidate aerosol models, developed by studying SeaWiFS imagery in intense dust storms in the same region. The results indicate that the methodology shows considerable promise for processing ocean color imagery in the presence of mineral dust, and immediately suggests the possibility of estimating other important consequences of the presence of dust, e.g., short-wave radiative forcing, radiative heating and its vertical distribution in the troposphere, etc. The methodology, i.e., developing and tuning candidate aerosol models using SeaWiFS imagery, can be applied to other regions and to other ocean color sensors in the same straightforward manner. The present dust models permit processing close to the African coast. The models need to be validated, or new

models developed, for regions in the dust zone farther off shore, as significant changes in the size distribution and particle characteristics may occur as the dust progresses across the Atlantic.

ACKNOWLEDGEMENTS

The authors are grateful for support for this work under the following grants and contracts: NASA NAS5-31363 (HRG, CM), NASA NAS5-31734 (HRG, VFB), NASA NAS5-31362 (RHE). CM is grateful for the additional support provided by the French Commissariat à l'Energie Atomique (CEA) and Centre National de la Recherche Scientifique (CNRS). This is contribution XXX from LSCE.

REFERENCES

Gordon, H.R., D.K. Clark, J.L. Mueller, and W.A. Hovis, Phytoplankton pigments derived from the Nimbus-7 CZCS: Initial comparisons with surface measurements, *Science*, **210**, 63-66, 1980.

Gordon, H.R., O.B. Brown, R.E. Evans, J.W. Brown, R.C. Smith, K.S. Baker, and D.K. Clark, A Semi-Analytic Radiance Model of Ocean Color, *J. Geophys. Res*., **93D**, 10909-10924, 1988.

Gordon, H.R., and M. Wang, Retrieval of water-leaving radiance and aerosol optical thickness over the oceans with SeaWiFS: A preliminary algorithm, *Appl. Optics*, **33**, 443-452, 1994.

Gordon, H.R., Atmospheric Correction of Ocean Color Imagery in the Earth Observing System Era, *J. Geophys. Res.*, **102D**, 17081-17106, 1997.

Gordon, H.R, T. Du, and T. Zhang, Remote sensing ocean color and aerosol properties: Resolving the issue of aerosol absorption, *Applied Optics*, **36**, 8670-8684, 1997.

Herman, J.R., P.K. Bhartia, O. Torres, C. Hsu, C. Seftor, and E. Celarier, Global distributions of UV-absorbing aerosols from Nimbus 7/TOMS data, *J. Geophys. Res.*, **102D**, 16889-16909, 1997.

Moulin, C., F. Dulac, C.E. Lambert, P. Chazette, I. Jankowiak, B. Chatenet, and F. Lavenu, Long-term daily monitoring of Saharan dust load over ocean using Meteosat ISCCP-B2 data, 2, Accuracy of the method and validation using sunphotometer measurements., *J. Geophys. Res.*, **102**, 16959-16969, 1997.

Moulin, C., H.R. Gordon, R.H. Evans, and V.F. Banzon, Assessment of Saharan dust absorption in the visible to improve ocean color retrievals and dust radiative forcing estimates from SeaWiFS imagery. *J. Geophys. Res.*, 2000 (Submitted).

O'Reilly, J.E., S. Maritorena, B.G. Mitchell, D.A. Siegel, K.L. Carder, S.A. Garver, M. Kahru, C. McClain, Ocean color chlorophyll algorithms for SeaWiFS, *J. Geophys. Res.* **103C**, 24937-24953, 1998.

Patterson, E.M., Optical Properties of Crustal Aerosol: Relation to Chemical and Physical Characteristics, *J. Geophys. Res.,* **86C**, 3236-3246, 1981.

Shettle, E. P. Optical and radiative properties of a desert aerosol model, In *Proc. Symposium on Radiation in the Atmosphere*, ed. G. Fiocco, Hampton, Va.: A. Deepak, 1984.

Young, R.W., K.L. Carder, P.R. Betzer, D.K. Costello, R.A. Duce, G.R. Ditullio, N.W. Tindale, E.A. Laws, M. Uematsu, J.T. Merrill, and R.A. Feeley, Atmospheric Iron Inputs and Primary Productivity: Phytoplankton Responses in the North Pacific, *Global Biogeochem. Cycles*, **5**, 119-134, 1991.

Figure 1. 8-day mean (30 Sept.–7 Oct., 1997) of the *AOD* as retrieved using the SMA.

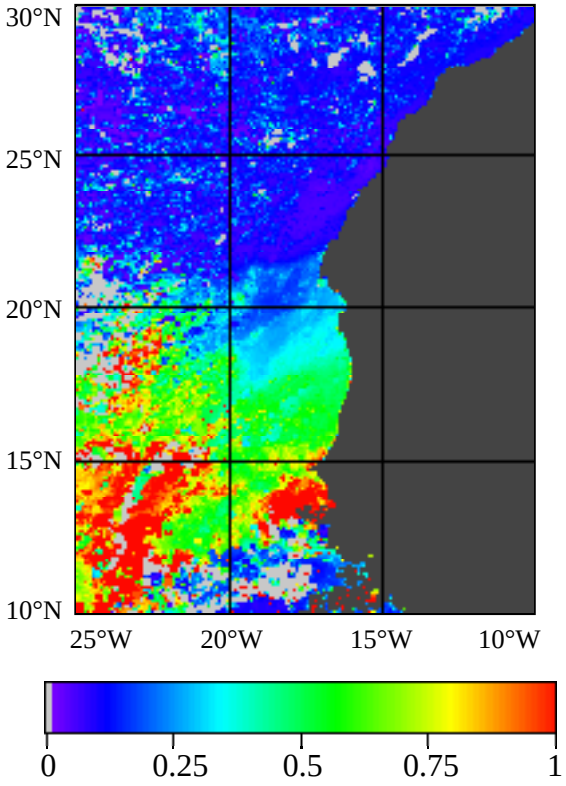

Figure 2. Pigment concentrations for the clear day using the STD and the SMA processings.

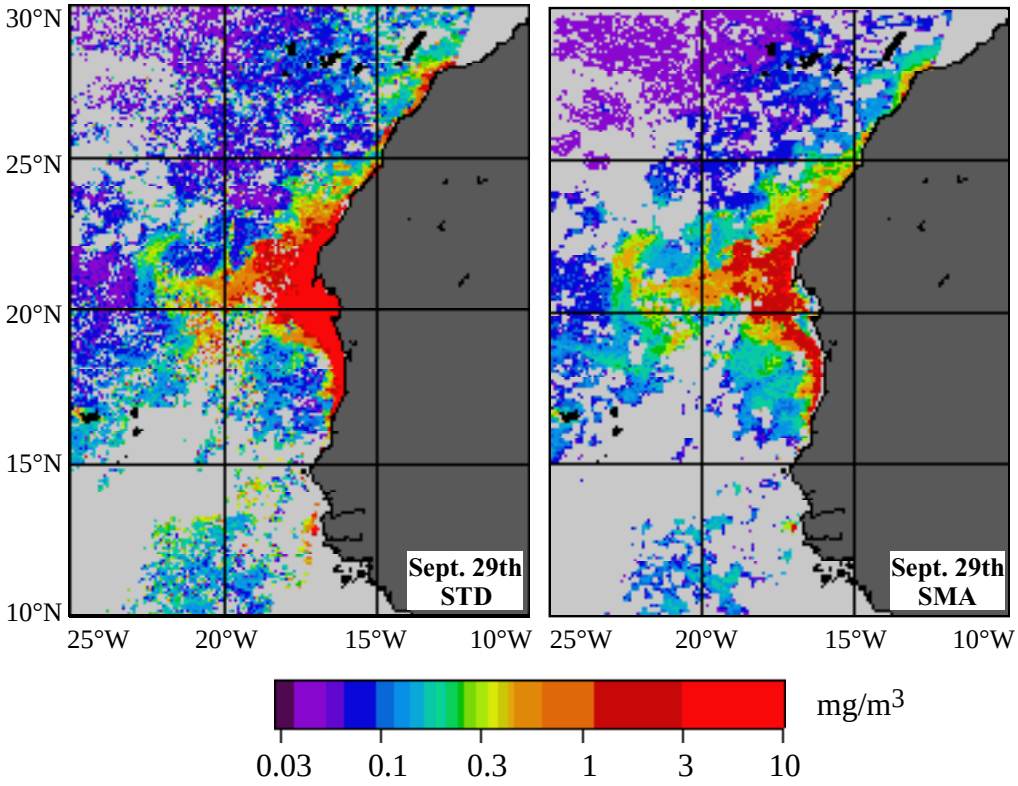

Figure 3. Pigment concentrations for the two "dusty" days using STD and SMA processings.

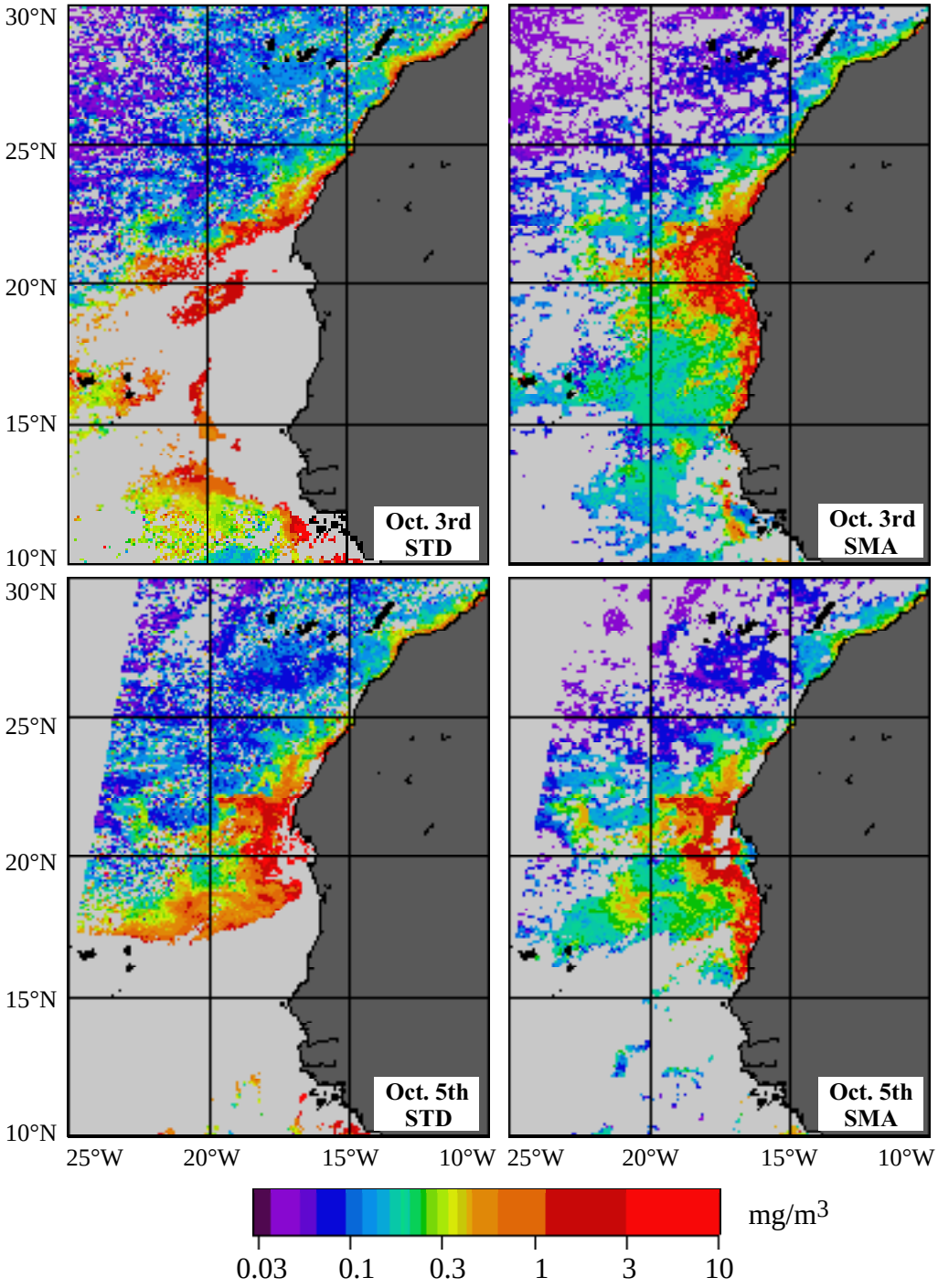

Figure 4. 8-day means (30 Sept.–7 Oct., 1997) of the pigment concentration using STD (left panel) and SMA (right panel) processings.

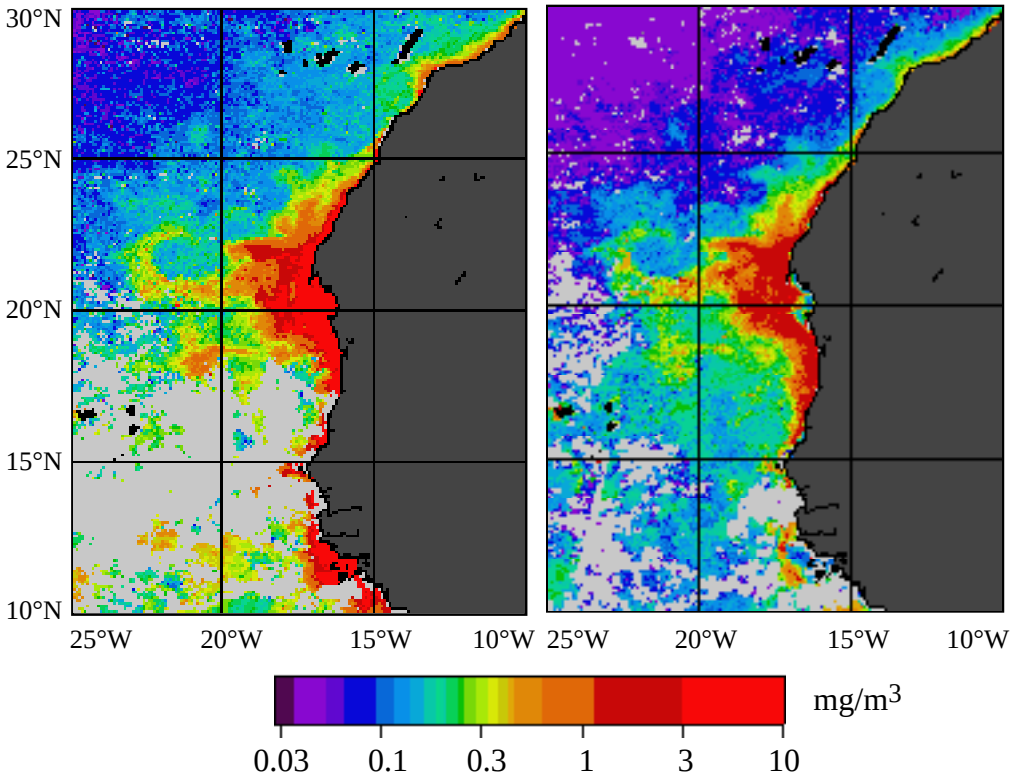

Appendix IV

Atmospheric correction of ocean color imagery: Test of the spectral optimization algorithm with SeaWiFS

Atmospheric correction of ocean color imagery: Test of the spectral optimization algorithm with SeaWiFS

Roman M. Chomko and Howard R. Gordon

Department of Physics

University of Miami

Coral Gables, FL 33124

Submitted to *Applied Optics*

Abstract

We implemented the spectral optimization algorithm [Chomko and Gordon, *Applied Optics*, **37**, 5560-5572 (1998)] (SOA) in an image processing environment and tested it with SeaWiFS imagery from the Middle Atlantic Bight and the Sargasso Sea. We compared the SOA and standard SeaWiFS algorithms (STD) on two days that had significantly different atmospheric turbidities but, because of their location and time of the year, nearly the same water properties. The SOA-derived pigment concentration showed excellent continuity over the two days, with the relative difference in pigments exceeding 10% only in regions characteristic of high advection. The derived water-leaving radiances at 443 and 555 nm were also within $\sim$ 10% and at 555 nm were close to clear water values in the Sargasso Sea. There was no obvious correlation between the relative differences in pigments and the aerosol concentration. In contrast, the standard processing (STD) showed poor continuity in derived pigments over the two days, with the relative differences correlating strongly with atmospheric turbidity. Additionally, the STD-derived pigment concentration showed considerably more noise than the SOA pigments. SOA-derived atmospheric parameters suggested that the retrieved ocean and atmospheric reflectances were decoupled on the more turbid day, but not on the clearer day, where the aerosol concentration was so low that relatively large changes in aerosol properties resulted in only small changes in aerosol reflectance. This implies that SOA-derived atmospheric parameters cannot be accurate in very clear atmospheres.

1. Introduction

Since the proof-of-concept ocean color mission, the Coastal Zone Color Scanner (CZCS),[1–3] monitoring the concentration of phytoplankton pigments (C), the sum of the concentrations of chlorophyll a and phaeophytin a, in the ocean from space-borne sensors has become well established. Such sensors employ a set of discrete spectral bands throughout the visible and into the near infrared region of the spectrum, and scan the earth producing a two-dimensional image of the ocean. Optically, phytoplankton reveal their presence through their influence on the absorption of light by the water body by virtue of the strong absorption in the blue by the photosynthetic pigment chlorophyll a and by various accessory pigments. Thus, in contrast to waters with low concentrations of phytoplankton, that are bright in the blue, waters with high concentration of phytoplankton are usually dark in the blue. The ocean color is a term that generally refers to the spectrum of light backscattered out of the ocean — the "water-leaving radiance." The concentration of chlorophyll a is a proxy for the phytoplankton concentration.

To improve the accuracy of the space-borne estimates, sensors with higher radiometric sensitivity than CZCS have been developed. These include SeaWiFS,[4] which was launched August 1, 1997, and MODIS,[5] launched December 18, 1999. The improvement in radiometric sensitivity necessitated the development of more sophisticated algorithms for both atmospheric correction, to retrieve the water-leaving radiance from the total radiance measured at the top of the atmosphere (TOA), and bio-optical interpretation, for relating the water-leaving radiance to the phytoplankton concentration.

The principal problem in atmospheric correction is to estimate the aerosol contribution to the measured TOA radiance. Aerosols are highly variable in space and time as well as composition, thus their physical-chemical characteristics need to be estimated for each pixel in an image. In contrast to the CZCS single-scattering atmospheric correction,[6,7] the

algorithm developed for SeaWiFS and MODIS[8,9] incorporates the full effects of multiple scattering. This algorithm uses the fact that the water-leaving radiance is negligible in the near infrared (NIR) region of the spectrum to assess the amount and the spectral variation of the aerosol contribution to the TOA radiance in the visible. This is effected by comparing the spectral variation of the aerosol component in the NIR with that of several candidate aerosol physical-chemical models. The most appropriate models are then used to estimate the aerosol contribution in the visible. This technique appears to work well when the aerosol is nonabsorbing; however, it fails completely when the aerosol is strongly absorbing because it is generally impossible to infer the presence of the aerosol's absorption using only measurements in the NIR.[9] Because strongly absorbing aerosol are often transported over the oceans by the winds, e.g., urban pollution transported off the U.S. East Coast, and wind-blown dust from Africa, it is important to be able to make atmospheric corrections in the presence of such aerosols. This can only be effected by incorporating measurements from the visible into the correction process. The difficulty with this is that the water-leaving radiance in the visible depends on the phytoplankton concentration and therefore is unknown *a priori*. Two methods of proceeding have been proposed, and both perform very well with simulated pseudo data. In the first, Gordon et al.[10] proposed (1) expanding the candidate aerosol model set to include strongly absorbing aerosols, (2) modeling the ocean reflectance throughout the visible using the semi-analytic model of Gordon et al.,[11] that relates the water-leaving radiance to the pigment concentration and a particle backscattering scattering coefficient, and (3) systematically varying all the parameters of the water model and the aerosol concentration of each aerosol model until a best fit (in an rms sense) to the measured TOA radiance is determined. This provides both the water properties and the aerosol properties simultaneously. In the second method[12] a very simple one-parameter model is assumed for the aerosol size distribution, a set of aerosol refractive indices that represent a range of absorption properties is used in conjunction with Mie theory to derive the aerosol optical properties, and these models are combined with the

semi-analytic radiance model to determine both the aerosol and water properties through a nonlinear optimization procedure. The drawback for the first method is the requirement that the aerosol models be representative (the closer one of the models is to reality, the better will be the retrieval of aerosol and water properties). In the second method, no attempt is made to use realistic models and this is a definite advantage — if it actually works.

In this paper, we report a series of tests made with the spectral optimization algorithm (SOA), second method in the last paragraph, using SeaWiFS imagery. These tests suggest that the SOA is a viable approach to atmospheric correction, and can retrieve realistic water parameters in cases in which the standard Gordon and Wang[8] algorithm (henceforth referred to as the "STD," i.e., "standard," algorithm) fails.

We begin with a brief review of radiative transfer in the ocean-atmosphere system. Next, we describe the SOA and STD algorithms. Finally, we examine the performance of both algorithms under clear and turbid atmospheric conditions off the U.S. East Coast.

2. Radiative Transfer and Radiative Properties Review

To provide a framework for the discussion in Section 3 below, we briefly review radiative transfer in the atmosphere-ocean system, the size distributions used to derive aerosol models for atmospheric correction, and the water-leaving reflectance in terms of the concentration of phytoplankton pigments.

A. Radiative Transfer

We prefer to use reflectance ρ in place of radiance L. The reflectance is defined by $\rho = \pi L / F_0 \cos\theta_0$, where F_0 is the extraterrestrial solar irradiance and θ_0 is the solar zenith

angle. Eliminating sun-glint contaminated pixels, and correcting for whitecaps, yields the reflectance at the top of the atmosphere $\rho_t(\lambda)$. It includes the following components:[9] the pure Rayleigh (molecular) scattering contribution $\rho_r(\lambda)$, the pure aerosol scattering contribution $\rho_a(\lambda)$, the contribution due to the interaction between air molecules and aerosols $\rho_{ra}(\lambda)$, and the desired water-leaving contribution $t(\lambda)\rho_w(\lambda)$, i.e.,

$$\rho_t(\lambda) = \rho_r(\lambda) + \rho_a(\lambda) + \rho_{ra}(\lambda) + t(\lambda)\rho_w(\lambda), \tag{1}$$

where $t(\lambda)$ is the diffuse transmittance of the atmosphere. Since $\rho_r(\lambda)$ can be computed precisely from an estimate of the surface atmospheric pressure,[13,14] it can be subtracted from $\rho_t(\lambda)$ to form

$$\rho_t(\lambda) - \rho_r(\lambda) = \rho_A(\lambda) + t(\lambda)\rho_w(\lambda), \tag{2}$$

where $\rho_A(\lambda) \equiv \rho_a(\lambda) + \rho_{ra}(\lambda)$. Both SeaWiFS and MODIS have spectral bands in the NIR for which ρ_w is nearly negligible in Case 1 waters,[3] which comprise most of the oceans. Calling λ_s and λ_ℓ the shorter and longer wavelengths of the NIR bands, respectively, we can form

$$\varepsilon'(\lambda_s, \lambda_\ell) \equiv \frac{\rho_A(\lambda_s)}{\rho_A(\lambda_\ell)}. \tag{3}$$

For SeaWiFS, $\lambda_s = 765$ nm and $\lambda_\ell = 865$ nm. If the aerosol optical thickness $\tau_a(\lambda)$ were sufficiently small, single scattering could be employed in the radiative transfer process. In this case Eq. (1) can be written $\rho_t = \rho_r + \rho_{as} + t\rho_w$, where ρ_{as} is the "single-scattered aerosol reflectance." A quantity $\varepsilon(\lambda_s, \lambda_\ell)$ similar to $\varepsilon'(\lambda_s, \lambda_\ell)$ can be formed using the single scattered aerosol reflectances:

$$\varepsilon(\lambda_s, \lambda_\ell) \equiv \frac{\rho_{as}(\lambda_s)}{\rho_{as}(\lambda_\ell)}. \tag{4}$$

$\varepsilon(\lambda_s, \lambda_\ell)$ depends only on the physical-chemical characteristics of the aerosol but not on its concentration. In contrast, $\varepsilon'(\lambda_s, \lambda_\ell)$ includes the effects of multiple scattering and therefore does depend on the aerosol concentration. The virtue of $\varepsilon(\lambda_s, \lambda_\ell)$ and $\varepsilon'(\lambda_s, \lambda_\ell)$

is that they both depend mostly on the particle size distribution and very little on the aerosol refractive index. Unfortunately, this means that these quantities are not helpful in assessing the presence or absence of aerosol absorption.

B. Aerosol Models

Two types of aerosol size distributions have been considered: log-normal distributions and power-law distributions. The multicomponent log-normal distribution given by

$$\frac{dN_i}{dD} = \frac{N_i}{\log_e(10)\sqrt{2\pi}\sigma_i D} \exp\left[-\frac{1}{2}\left(\frac{\log_{10}(D/D_i)}{\sigma_i}\right)^2\right], \tag{5}$$

where, dN_i is the number of particles per unit volume per with diameter between D and $D + dD$ of the i^{th} species or component, D_i, and σ_i are the modal diameter and the standard deviation, respectively, and N_i is the total number density of the i^{th} component. Summing over the components provides the actual size distribution:

$$\frac{dN}{dD} = \sum_{i=1}^{M} \frac{dN_i}{dD}. \tag{6}$$

For the models developed by Shettle and Fenn,[15] $M = 2$, i.e., there are two components. Each component had its own refractive index and the radiative properties were determined using Mie theory.

The Junge power-law size distribution[16] is of the form

$$\begin{aligned} \frac{dN}{dD} &= K, && D_0 < D \leq D_1, \\ &= K\left(\frac{D_1}{D}\right)^{\nu+1}, && D_1 < D \leq D_2, \\ &= 0, && D > D_2, \end{aligned}$$

where dN is the number of particles per unit volume with diameters between D and $D + dD$. In contrast to the log-normal size distribution, given D_0, D_1 and D_2, the power-law distribution is characterized by a single parameter, ν. Chomko and Gordon[12] chose

$D_0 = 0.06$ μm, $D_1 = 0.20$ μm, and $D_2 = 20$ μm, and assigned a single refractive index to the entire distribution to compute the radiative properties using Mie theory.

C. Water-leaving Reflectance

In the CZCS era, the water reflectance was related to the pigment concentration through empirical fits of log-transformed reflectance ratios $[\rho_w(\lambda_1)/\rho_w(\lambda_2)]$ to C.[7,17] The form of these ratios were later explained quantitatively by Gordon and Morel.[3] When individual reflectances are examined as a function of C, they are found to be noisy. This noise is in part due to the natural variation of particle scattering with C.[3] Gordon et al.,[11] developed a model for ρ_w as a function of C and a scattering parameter b^0, that was successful in explaining the variation of ρ_w with water constituents, and in accurately reproducing the empirical reflectance ratio versus C relationships. In preparation for the SeaWiFS launch, a complete review of the empirical algorithms was effected by O'Reilly et al.,[18] leading to new empirical algorithms for SeaWiFS. These algorithms were formulated in terms of chlorophyll a (Chl) as opposed to C, and a C-Chl relationship was determined.

3. The STD and SOA Algorithms

A. The STD Algorithm

The STD algorithm[8] is presently being used to process SeaWiFS imagery. It employs a set of candidate aerosol models, from which it selects two, to extrapolate the NIR behavior of ρ_A into the visible. The basic form of the algorithm is as follows. For each model, the reflectance $\rho_A(\lambda)$ is related to the single scattering reflectance ρ_{as} through a set of look up tables (LUTs) that in essence contain the coefficients a, b, etc., in

$$\rho_A(\lambda) = a(\lambda)\rho_{as}(\lambda) + b(\lambda)\rho_{as}(\lambda)^2 + c(\lambda)\rho_{as}(\lambda)^3 + d(\lambda)\rho_{as}(\lambda)^4, \tag{7}$$

where a, b, etc., are also dependent on the viewing-solar geometry, and the particular aerosol model. They contain all of the multiple scattering effects in $\rho_A(\lambda)$. Given the measured ρ_A in the NIR, Eq. (7) is inverted to give an estimate of ρ_{as}, and thus an estimate of what each model would predict for $\varepsilon(\lambda_s, \lambda_\ell)$. Fortunately, these predictions are all nearly the same, i.e., although $\varepsilon(\lambda_s, \lambda_\ell)$ and $\varepsilon'(\lambda_s, \lambda_\ell)$ may differ considerably, the multiple scattering effects on $\varepsilon(\lambda_s, \lambda_\ell)$ are only weakly dependent on the aerosol model. (Note, however, that this is only true in the NIR, in the visible, the effects of multiple scattering are strongly model-dependent.[8,9]) The resulting $\varepsilon(\lambda_s, \lambda_\ell)$'s derived using the individual models are then averaged, the mean is compared to the actual ε's for each aerosol model, and the two models that are closest to, and bracket, the mean ε are used to the effect the atmospheric correction. For each of the two chosen models, the model ε value, referred to as $\varepsilon^{(M)}$, is used to compute ρ_{as} in the visible through

$$\rho_{as}^{(M)}(\lambda) = \varepsilon^{(M)}(\lambda, \lambda_\ell)\rho_{as}^{(M)}(\lambda_\ell),$$

where $\rho_{as}^{(M)}(\lambda_\ell)$ is the value of $\rho_{as}(\lambda_\ell)$ inverted from the measured $\rho_A(\lambda_\ell)$ with Eq. (7) using the given model. Equation (7) is then used to compute $\rho_A^{(M)}(\lambda)$ from $\rho_{as}^{(M)}(\lambda)$. The

final value of $\rho_A(\lambda)$ is a linear combination of the $\rho_A^{(M)}(\lambda)$'s for the two models, weighted in relation to the closeness of the individual $\varepsilon^{(M)}(\lambda_s, \lambda_\ell)$'s to the mean ε. Given $\rho_A(\lambda)$, we immediately find $t(\lambda)\rho_w(\lambda)$. The value of t for each model is found from a separate set of LUTs[19] and the final value of t is also a linear combination of those for the two models weighted in the same manner as for $\rho_A(\lambda)$. The ocean chlorophyll concentration, Chl, is then estimated using the two-band (490 and 555 nm) OC2 algorithm from O'Reilly et al.[18] The pigment concentration is derived from the chlorophyll concentration using

$$C = 1.34\,\mathrm{Chl}^{0.983}, \tag{8}$$

also from O'Reilly et al.

The STD algorithm uses the Shettle and Fenn[15] aerosol models as modified by Gordon and Wang.[8] These are the Maritime, Coastal, and Tropospheric models at 50, 70, 90, and 99% relative humidity, for a total of 12 candidate aerosol models. The Maritime and Coastal models are essentially nonabsorbing, and the Tropospheric models are weakly absorbing. As expected, the algorithm fails when strongly absorbing aerosols are present.

B. The SOA

The SOA[12] attempts to simultaneously retrieve the water and aerosol parameters. It uses the Junge power-law size distribution for the aerosol. The quantity $\rho_A(\lambda)+t(\lambda)\rho_w(\lambda)$ is computed at each pixel using Eq. (2). The aerosol reflectance ρ_A must be a function of m_r, m_i, ν, and τ_a, the real and imaginary parts of the aerosol's refractive index, the Junge size parameter, and the aerosol optical depth at 865 nm, respectively, i.e., $\rho_A(\lambda) = \rho_A(\lambda; m_r, m_i, \nu, \tau_a)$. In a similar manner, $t(\lambda) = t(\lambda; m_r, m_i, \nu, \tau_a)$. The water-leaving reflectance ρ_w is modeled using the Gordon et al.,[11] semi-analytic model that employs the two parameters C and b^0, so $\rho_w(\lambda) = \rho_w(\lambda; C, b^0)$. Thus,

$$\rho_A(\lambda) + t(\lambda)\rho_w(\lambda) = \rho_A(\lambda; m_r, m_i, \nu, \tau_a) + t(\lambda; m_r, m_i, \nu, \tau_a)\rho_w(\lambda; C, b^0),$$

and there are six parameters to be determined with eight spectral bands. Following Ref. 12, the number of parameters is reduced to four by estimating ν from $\varepsilon'(\lambda_s, \lambda_\ell)$. This is effected by forming the mean ε' over all models and τ_a for a given ν:

$$\overline{\varepsilon}'(\lambda_s, \lambda_l, \nu) = \frac{1}{N_{m_r} + N_{m_i} + N_{\tau_a}} \sum_{r,i,k=1}^{N_{m_r}, N_{m_i}, N_{\tau_a}} \varepsilon'(\lambda_s, \lambda_l;\ m_r^{(r)}, m_i^{(i)}, \tau_a^{(k)}, \nu),$$

where N_{m_r} is the total number of values of $m_r^{(r)}$, N_{m_i} is the total number of values of $m_i^{(i)}$, and N_{τ_a} is the number of values $\tau_a^{(k)}$ used to establish the mean. The value of ν is the found by requiring $\varepsilon'(\lambda_s, \lambda_\ell) = \overline{\varepsilon}'(\lambda_s, \lambda_l, \nu)$. The value of $\varepsilon'(\lambda_s, \lambda_l)$ is established by assuming that ρ_w is negligible in the NIR, which is the same assumption used in the STD algorithm.

Given ν, τ_a can be estimated from $\rho_A(\lambda_\ell)$ for each value of m_r and m_i, so finally, we need to determine only m_r, m_i, C, and b^0. This is accomplished by minimizing the cost function

$$S^2_{\mathrm{LSQ}}(\nu, m_r, m_i, \tau_a, C, b^0) = \frac{1}{N-1} \times \sum_{j=1}^{N} \left[1 - \frac{\rho_A(\lambda_j;\ m_r, m_i, \nu, \tau_a) + t(\lambda_j;\ m_r, m_i, \nu, \tau_a)\rho_w(\lambda_j;\ C, b^0)}{\rho_t(\lambda_j) - \rho_r(\lambda_j)} \right]^2 \tag{9}$$

where the numerator within the square brackets is to be calculated and the denominator is provided by the sensor, using nonlinear optimization. In this work, $N = 5$ with $\lambda_j = 412$, 443, 490, 510, and 555 nm. The SeaWiFS band at 670 nm is not used. The optimization is subject to the constraints $1.33 \le m_r \le 1.50$, $0 \le m_i \le 0.04$, $0.05 \le C \le 1.5$ mg/m^3, and $0.4 \le f \le 1.5$, where $b^0 = 0.3\,f$ in m^{-1} (See Ref. 11 for a precise definition of b^0). The final result provides estimates of m_r, m_i, C, and b^0 at the minimum. These, along with ν and τ_a, also provide estimates of $\rho_A(\lambda)$, $\rho_w(\lambda)$, and the aerosol single scatter albedo $\omega_0(\lambda)$, a measure of aerosol absorption. The retrieved C gives Chl using Eq. (8).

The values of $\rho_A(\lambda; m_r, m_i, \nu, \tau_a)$ used in the operation of the algorithm are obtained by interpolation between discrete values of the appropriate parameters. Radiative transfer simulations were carried out for a two-layer atmosphere (aerosols in the lower layer) for $m_r = 1.33$ and 1.50, $m_i = 0$, 0.001, 0.003, 0.01, 0.03, and 0.04, and $\nu = 2.0$, 2.5, 3.0, 3.5, 4.0, and 4.5 for a total of 72 aerosol models. Typically the computations would be carried out for 33 solar zenith angles from 0 to 80 deg, and, as there are 8 SeaWiFS bands and 9 values of τ_a used, the total number of simulations would be $72 \times 33 \times 8 \times 9 = 171,072$. However, for the purposes of this test, a limited subset of the computations were performed using only 12 solar zenith angles — $22.5°(2.5°)50°$— for a total of 62,208 radiative transfer simulations. These simulations were used to prepare a set of LUTs similar to those used in the STD algorithm, i.e., Eq. (7):

$$\rho_A(\lambda; m_r, m_i, \nu, \tau_a) = a(\lambda; m_r, m_i, \nu)\tau_a(\lambda) + b(\lambda; m_r, m_i, \nu)\tau_a(\lambda)^2 + c(\lambda; m_r, m_i, \nu)\tau_a(\lambda)^3 + d(\lambda; m_r, m_i, \nu)\tau_a(\lambda)^4$$

for each model (a model here is a set m_r, m_i, ν), where a, b, etc., are also functions of the solar-viewing geometry.

The SOA algorithm was placed in an image processing environment to test it on actual ocean-color imagery. In this version, the optimization is accomplished in a manner identical to that described in Ref. 12. Table 1 summarizes the differences and similarities between the SOA and STD algorithms.

4. Test of the SOA with SeaWiFS imagery

A. Imagery used in the test

We tested the SOA using SeaWiFS imagery off the U.S. East Coast (the Middle Atlantic Bight and Sargasso Sea), where the aerosol often originates from the U.S. and is

sometimes absorbing. In this study, we examined two SeaWiFS images from October 1997: days-of-the-year 279 and 281 (October 6 and 8). True color renditions of these images are presented in Figure 1. Images of $\rho_A(865)$, which is roughly proportional to the aerosol optical thickness $\tau_a(865)$, remapped to a standard (Mercator) grid, are provided in Figure 2 for the areas shown in Figure 1. For Day 279, the atmosphere over the area examined is turbid, e.g., along Track 2 $\rho_A(865)$ reaches 0.02. In contrast, Day 281 is characterized by a clear atmosphere, with $\rho_A(865)$ more than a factor of 4–5 lower near the northern portion of Track 2. The Day-281 values of $\rho_A(865)$ are more characteristic of the open ocean far from land, i.e., a pure marine atmosphere. Although we have no surface truth for these images, atmospheric correction in a clear atmosphere is not difficult, and we expect that both the SOA and the Gordon and Wang algorithm (STD) will perform well on Day 281. However, because of the turbid atmosphere, this may not be the on case Day 279.

B. SOA-STD comparison

Here we judge the efficacy of the algorithms under two criteria.

First, both STD and SOA should provide similar pigment concentrations and water-leaving radiances on Day 281. In the Sargasso Sea (southern portion of Tracks 2 and 3), the water-leaving radiances should be characteristic of those in clear ocean water,[20] particularly in the green (555 nm).

Second, the retrieved pigment concentrations and water-leaving radiances for Days 279 and 281 should be very similar, because we do not expect large changes in water properties over this large area at this time of the year over a time period of 48 hours. (However, note that such changes would be possible in the spring.) Local changes are possible through advection, and these should be easily recognized in the imagery, but the gross values of these parameters should not change.

Figure 3 provides remapped imagery of the retrieved phytoplankton pigment concentration for this two days processed with the SOA and the STD algorithms. The color scale is the same for STD and SOA. Black in the image is either clouds or land. [The cover of this issue shows scan coordinate versions of the SOA algorithm enhanced to show the eddy structure in the Sargasso Sea (lower panels), and the finger-like patterns near the north wall of the Gulf Stream (upper panels).]

It is obvious from Figure 3 that the SOA-retrieved pigment concentrations are very similar in all areas for the two days. In contrast, the STD-derived concentrations differ significantly from 279 to 281, especially in the vicinity of the higher aerosol concentrations (Figure 2).

In the SOA, recognizable eddies (see cover) in the Sargasso Sea appear to retain their pigment concentrations over the two days, while in the STD processing it is difficult to even recognize eddies there. (STD-processed imagery with the same enhancement as the SOA on the cover is not shown.)

Figure 4 provides the pigment concentrations for Days 279 and 281 and for the SOA and STD algorithms along the three tracks shown on Figures 2 and 3. It shows that the SOA pigment concentrations are very consistent for the two days except in the regions of high advection (Track 1 and the northern portions of Tracks 2 and 3). In the turbid-atmosphere region (Track 2) the STD algorithm shows approximately a factor of 2 difference in pigment concentration between the two days, while the SOA pigments are consistent over the two days. In contrast, along Track 3, for which the atmosphere is clear over most of the Track (Figure 2) on both days, the SOA and STD algorithms are both consistent over the two days; however, the STD pigments are approximately a factor of two higher than the SOA pigments for low pigment concentrations. This is to be expected because the SOA uses the Gordon et al. radiance model.[11] Given the same spectrum of water-leaving radiances, the radiance model will yield a lower pigment concentration than the OC2 algorithm[18] that is used in the standard processing, when the concentration is low (Figure 5). This difference decreases as the pigment concentration increases. Thus, we believe that the differences in the overall pigment concentrations in the Sargasso Sea are not the result of atmospheric correction, but result from different interpretations of the water-leaving reflectance.

It is interesting that there appears to be much more detail and less noise in the imagery processed with the SOA than the STD algorithm. There are two reasons for this. First, the SOA employs all of the bands to estimate the pigment concentration (and simultaneously perform atmospheric correction) as opposed to only the 490 and 555 nm bands in the standard processing. Using more bands, and wider spacing between bands, results in a

noise reduction [R. Frouin, personal communication]. Second, the bands at 412 and 443 nm are significantly more sensitive to changes in pigment concentration than the 490 nm band, and therefore show more detail in the water. Figure 4 quantitatively shows the reduced "noise" in the pigment concentration produced by the SOA compared to the STD algorithm, especially in the Sargasso Sea (southern ends of Tracks 2 and 3).

Figure 6 provides images of the absolute relative deviation in the pigment concentration between Days 279 and 281:

$$RD = 100\% \left[\frac{|C(279) - C(281)|}{C(281)} \right]. \tag{10}$$

The SOA-derived pigments are remarkably consistent over the cloud-free portions of the combined images, with $RD \lesssim 10\%$. Regions with larger RD (20-35%) typically occur in very dynamic areas, e.g., the North Wall of the Gulf Stream that separates the higher-productivity waters of the Middle Atlantic Bight (MAB) from the low-productivity waters of the Sargasso Sea, where the differences are easily explained by advection. In contrast to the SOA, the STD algorithm shows significant changes in C over the two days: as much as a factor of two. In addition, these are seen to correlate with areas of high atmospheric turbidity (Figure 2) as well as advection features.

The fact that the SOA-derived pigments are consistent over the two days, although highly suggestive, does not prove that the atmospheric correction is successful. A more definitive test is the consistency of the derived water-leaving reflectances, and their approach to the clear-water values,[20] independent of atmospheric turbidity. Figures 7 and 8 compare the normalized water-leaving radiances[20] (nLw) at 443 and 555 nm. retrieved by the two algorithms for the two days. Figure 7 shows the nLw differences (Eq. (10) with C replaced by nLw) for 443 and 555 nm, and Figure 8 provides the nLw values along Tracks 2 and 3. Figure 7 shows excellent agreement over the two days for the SOA, with errors

$\lesssim$ 10% except in the regions of high advection. The STD algorithm again shows large errors that mimic the pattern of atmospheric turbidity (especially at 555 nm).

Figure 8 shows that the SOA algorithm provides values of nLw at 555 nm in the Sargasso Sea that are independent of the atmospheric turbidity and close to the clear-water value[20] $\sim$ 0.28 mW/cm$^2\mu$mSr. The two algorithms retrieve similar values in low turbidity regions, but not high-turbidity areas.

The comparisons in this subsection show that the SOA out performs the STD algorithm in recovering C and nLw in the more turbid atmosphere (279). In the following subsection we examine the retrieval of parameters unique to the SOA — aerosol absorption, ν, b^0, and S_{LSQ}.

C. Additional parameters estimated with the SOA

For a given value of C, which largely determines the spectral shape of the water-leaving radiance, b^0 controls the actual magnitude of the water-leaving radiance at each wavelength. Figure 9 provides the retrieved values of b^0 (actually f) for the two days. The values are realistic in the sense that b^0 is somewhat lower in the Sargasso Sea than in the MAB. This was also observed in Ref. 11. They are usually within the range set within the program ($0.4 \leq f \leq 1.5$) and only occasionally at the boundaries of the range (an exception being in the vicinity of the coast where b^0 would be expected to be outside the range). Gross consistency in b^0 is evident for the two days, although differences are apparent in some regions. In particular, in the vicinity of Track 1 (Figures 2 and 3) the values of b^0 appear to be somewhat lower on Day 279 compared to Day 281. This is paradoxical in the sense that the retrieved pigment concentrations are consistent here for the two days (Figures 4 and 6), and the most turbid region of Day 279 is over the western portion of the track, while on Day 281 its over the eastern portion. As one expects that the better values of b^0 are obtained in the clear atmosphere, the conclusion must be that the b^0 is higher along the western part of the slope waters in the MAB and smaller in the eastern part. If this is true, the error in b^0 in the turbid regions is ~ 0.2 to 0.3 in f.

Figure 10 provides the retrieved aerosol Junge power-law parameter ν and the aerosol single scattering albedo (ω_0) — the ratio of aerosol scattering to aerosol scattering *plus* aerosol absorption — at 865 nm. $\omega_0 = 1$ for a nonabsorbing aerosol and zero for a nonscattering aerosol. We consider the aerosol to be strongly absorbing if $\omega_0 \lesssim 0.9$. The values of ω_0 used in the STD algorithm were in the range 0.92 to 1.0.

For the turbid day $\nu > 3$ almost everywhere, suggesting a size distribution favoring small particles. South of the cloud front at the bottom of the image $\nu \lesssim 2.5$ suggesting a maritime aerosol. On the clearer Day 281, the value of ν is seen to decrease from $\gtrsim 3$ in

the MAB to maritime values far off shore. Note that ν is determined solely from the bands at λ_s and λ_ℓ, which are not influenced by water properties (except close to the coast), and therefore do not correlate with features clearly in the water.

Concerning ω_0, in the case of the more turbid atmosphere, $\omega_0 \approx 1$ throughout the image, which implies a weakly absorbing aerosol. Some water features appear in ω_0, but only close to the coasts where the assumption that $\rho_w(\lambda) = 0$ at 765 and 865 nm may not be valid. The fact that the aerosol is nearly nonabsorbing, along with $\nu > 3$, suggests that it is composed of mostly sulfate[21] and may originate in the mid-western U.S. (Figure 1). In contrast, on Day 281 water features are clearly evident in ω_0. The unrealistically low values north of the Gulf Stream suggest that ω_0 is not correctly obtained there. This problem occurs because the aerosol concentration is extremely low. In such cases, the algorithm in effect focuses in on the correct water properties and then tries to minimize S_{LSQ} by varying the aerosol properties (m_r and m_i), which varies ω_0. Because the aerosol concentration is so low, large variations in properties can take place with only modest variations in $\rho_A^{(c)}(\lambda)$. (Note that $\tau_a(865)$ is chosen so that $\rho_A^{(c)}(865)$ is correct.) The result is a very imprecise estimate of the aerosol's absorption properties. Thus, the retrieved aerosol absorption can only be trusted at sufficiently large aerosol concentrations. Similar conclusions were reached using simulated data.[12]

Figure 11 shows the retrieved images of $\tau_a(865)$ along with the parameter S_{LSQ} that determines the quality of the final solution. As discussed by Chomko and Gordon[12] $\tau_a(865)$ can be in error by as much as $\pm 50\%$ because the scattering phase functions derived from Junge power-law distributions may not be adequate in the backward directions (however, this is irrelevant for atmospheric correction). We provide $\tau_a(865)$ for completeness. Note that for Day 281 some water features are observed in $\tau_a(865)$. This is consistent with similar features in ω_0.

The S_{LSQ} images are almost almost mirror images of $\rho_A(865)$. This is to be expected as S_{LSQ} is the rms *relative* error in $\rho_A(\lambda)+t(\lambda)\rho_w(\lambda)$. For a similar absolute error in $\rho_w(\lambda)$ (Figure 7), S_{LSQ} will be inversely related to the aerosol concentration. If the atmosphere is very clear, i.e., $\rho_A(\lambda) \ll t(\lambda)\rho_w(\lambda)$, S_{LSQ} should indicate the ability of the semi-analytic ocean color model to represent $\rho_w(\lambda)$. Figure 11 suggests that the rms error in this ability is $\sim 10\%$ (near 38°N and 72°W).

5. Discussion

In this paper, we have tested the performance of an implementation of our SOA in an image processing environment with SeaWiFS imagery. We consider this to be a proof-of-concept exercise, in that our goal was the evaluation of the performance of the algorithm, not the advocacy of its use in its present form for routine SeaWiFS processing.

We compared the SOA and STD algorithms on two days that had significantly different aerosol concentrations but, because of their location, nearly the same water properties. The SOA showed excellent continuity over the two days in the derived pigment concentrations, with the relative difference in pigments exceeding 10% only in regions expected to have high advection. The derived water-leaving radiances (nLw) at 443 and 555 nm were also within $\sim 10\%$ and at 555 nm were close to clear water values[20] in the Sargasso Sea. There was no obvious correlation between the relative differences in pigments (and nLw) and the aerosol concentration (as delineated by $\rho_A(865)$).

In contrast, the standard processing (STD) showed poor continuity in derived quantities (C and nLw) over the two days, with the relative differences correlating strongly with the atmospheric turbidity. This implies a poor atmospheric correction. Furthermore, the STD derived pigment concentration showed considerably more noise than the SOA pigments.

The other SOA-derived water quantity b^0 (with some exceptions) showed good consistency over the two days; however, the atmospheric parameters ω_0 and $\tau_a(865)$ did not. The atmospheric parameters showed little or no correlation with C and b^0 for the turbid day (279), suggesting that the atmospheric correction was excellent. Both ω_0 and $\tau_a(865)$ showed obvious water patterns for the clear day indicating that the ocean and atmosphere were not totally decoupled on Day 281. The reason suggested for this is that the aerosol

concentration was so low that relatively large changes were possible in ω_0 with only small changes in $\rho_A(\lambda)$. Thus SOA-derived atmospheric parameters are only to be trusted when $\rho_A(865)$ is sufficiently large. We have not studied the minimum magnitude of $\rho_A(865)$ for which the SOA can yield adequate atmospheric parameters.

Based on the above, we believe we have demonstrated the efficacy of the SOA for processing ocean color imagery in Case 1 waters. However, it is important to recognize the SOA limitations. In the version used here, the pigment concentration is limited to the range 0 to 1.5 mg/m^3 and to Case 1 waters. These limitations are based on the fact that the semi-analytic model of ocean color[11] employed here has been validated only over this range. (As an aside, it should be pointed out that a significant fraction of the data used develop and validate the semi-analytic model were collected in 1979 in the area discussed in this paper.) Colored dissolved organic matter (CDOM) is only implicitly included[11] in the SOA and therefore cannot be explicitly retrieved. The algorithm in its present version is too slow to use in routine processing. We are presently studying approaches for reducing the SOA processing time.

We believe that the simultaneous retrieval of ocean and atmospheric properties, that forms the heart of the SOA, is the preferred approach for processing ocean color imagery. Although it requires a model of the ocean reflectance as a function of constituents, this should not be considered a blemish. The STD algorithm already requires models of the atmospheric reflectance, and ocean reflectance models are arguably as well developed as atmospheric models. Improvements in both ocean and aerosol models will yield a concomitant improvement in ocean color retrievals.

Acknowledgment

The authors are grateful for support from the National Aeronautics and Space Administration, Goddard Space Flight Center, under Contracts NAS5-31363 and NAS5-31734.

References

1. H. R. Gordon, D. K. Clark, J. L. Mueller and W. A. Hovis, "Phytoplankton pigments derived from the Nimbus–7 CZCS: initial comparisons with surface measurements," Science **210**, 63–66 (1980).

2. W. A. Hovis, D. K. Clark, F. Anderson, R. W. Austin, W. H. Wilson, E. T. Baker, D. Ball, H. R. Gordon, J. L. Mueller, S. Y. E. Sayed, B. Strum, R. C. Wrigley and C. S. Yentsch, "Nimbus 7 coastal zone color scanner: system description and initial imagery," Science **210**, 60–63 (1980).

3. H. R. Gordon and A. Y. Morel, *Remote Assessment of Ocean Color for Interpretation of Satellite Visible Imagery: A Review* (Springer-Verlag, New York, 1983), 114 pp.

4. S. B. Hooker, W. E. Esaias, G. C. Feldman, W. W. Gregg and C. R. McClain, *SeaWiFS Technical Report Series: Volume 1, An Overview of SeaWiFS and Ocean Color* (NASA, Greenbelt, MD, Technical Memorandum 104566, July 1992).

5. V. V. Salomonson, W. L. Barnes, P. W. Maymon, H. E. Montgomery and H. Ostrow, "MODIS: Advanced Facility Instrument for Studies of the Earth as a System," IEEE Geosci. Rem. Sens. **27**, 145–152 (1989).

6. H. R. Gordon, "Removal of Atmospheric Effects from Satellite Imagery of the Oceans," Applied Optics **17**, 1631–1636 (1978).

7. H. R. Gordon, D. K. Clark, J. W. Brown, O. B. Brown, R. H. Evans and W. W. Broenkow, "Phytoplankton pigment concentrations in the Middle Atlantic Bight: comparison between ship determinations and Coastal Zone Color Scanner estimates," Applied Optics **22**, 20–36 (1983).

8. H. R. Gordon and M. Wang, "Retrieval of water-leaving radiance and aerosol optical thickness over the oceans with SeaWiFS: A preliminary algorithm," Applied Optics **33**, 443–452 (1994).

9. H. R. Gordon, "Atmospheric Correction of Ocean Color Imagery in the Earth Observing System Era," Jour. Geophys. Res. **102D**, 17081–17106 (1997).

10. H. R. Gordon, T. Du and T. Zhang, "Remote sensing of ocean color and aerosol properties: resolving the issue of aerosol absorption," Applied Optics **36**, 8670–8684 (1997).

11. H. R. Gordon, O. B. Brown, R. H. Evans, J. W. Brown, R. C. Smith, K. S. Baker and D. K. Clark, "A Semi-Analytic Radiance Model of Ocean Color," Jour. Geophys. Res. **93D**, 10909–10924 (1988).

12. R. Chomko and H. R. Gordon, "Atmospheric correction of ocean color imagery: Use of the Junge power-law aerosol size distribution with variable refractive index to handle aerosol absorption,," Applied Optics **37**, 5560–5572 (1998).

13. J. E. Hansen and L. D. Travis, "Light Scattering in Planetary Atmospheres," Space Science Reviews **16**, 527–610 (1974).

14. H. R. Gordon, J. W. Brown and R. H. Evans, "Exact Rayleigh Scattering Calculations for use with the Nimbus-7 Coastal Zone Color Scanner," Applied Optics **27**, 862–871 (1988).

15. E. P. Shettle and R. W. Fenn, *Models for the Aerosols of the Lower Atmosphere and the Effects of Humidity Variations on Their Optical Properties* (Air Force Geophysics Laboratory, Hanscomb AFB, MA 01731, AFGL–TR–79-0214, 1979).

16. C. Junge, "Atmospheric Chemistry," Advances in Geophysics **4**, 1–108 (1958).

17. H. R. Gordon and D. K. Clark, "Atmospheric effects in the remote sensing of phytoplankton pigments," Boundary-Layer Meteorology **18**, 299–313 (1980).

18. J. E. O'Reilly, S. Maritorena, B. G. Mitchell, D. A. Siegel, K. L. Carder, S. A. Garver, M. Kahru and C. McClain, "Ocean color chlorophyll algorithms for SeaWiFS," Jour. Geophys. Res. **103C**, 24937–24953 (1998).

19. H. Yang and H. R. Gordon, "Remote sensing of ocean color: Assessment of the water-leaving radiance bidirectional effects on the atmospheric diffuse transmittance," Applied Optics **36**, 7887–7897 (1997).

20. H. R. Gordon and D. K. Clark, "Clear water radiances for atmospheric correction of coastal zone color scanner imagery," Applied Optics **20**, 4175–4180 (1981).

21. J. T. Kiehl and B. P. Briegleb, "The relative roles of sulfate aerosols and greenhouse gases in climate forcing," Science **260**, 311–314 (1993).

Table 1: Comparative Methodology of the SOA and STD algorithms.

	Method or Structure	
Function	STD Algorithm	SOA
Aerosol Assumptions*	12 models: M,C,T at 4 relative humidities	72 Junge Power-Law models: 6 values of ν, 2 of m_r, 6 of m_i
Vertical Structure	Two-layer Aerosol in lower layer	Two-layer Aerosol in lower layer
NIR Water Properties	$\rho_w(765) = 0$ $\rho_w(865) = 0$	$\rho_w(765) = 0$ $\rho_w(865) = 0$
Data Storage	LUT for $\rho_A(\rho_{as})$ and $t(\tau_a)$	LUT for $\rho_A(\tau_a)$ and $t(\tau_a)$
Aerosol Properties:	Bands 7 and 8 are used to determine $\varepsilon(765, 865)$. LUTs are used to bracket the best 2 models. Further interpolation provides an "average" model.	Bands 7 and 8 are used to determine ν given $\overline{\epsilon}'(765, 865)$. $\tau_a(865)$ is determined for each m_r, m_i set.
Aerosol Reflect. $\rho_A(\lambda)$	Based on extrapolation of the "average" model into the visible	Non-linear optimization using Bands 1 through 5 (Band 6 is optional)
Water-Leaving Reflect. $\rho_w(\lambda)$	Computed directly	Non-linear optimization using Bands 1 through 5 (Band 6 is optional)
Diffuse Transmit. $t(\lambda)$	Bidirectional effects not included	Bidirectional effects not included

*M, C, T, stand for Maritime, Coastal, and Tropospheric models.

Figure Captions

Figure 1. "True" color rendition of the SeaWiFS imagery from October 6 and October 8, 1997.

Figure 2. The aerosol reflectance at 865 nm ($\rho_A(865)$) along with three tracks from which processed data will be extracted. Note the significant difference in $\rho_A(865)$ between the two days.

Figure 3. Pigment concentration retrieved for Days 279 and 281 using the SOA (left panels) and the STD (right panels). The image has been remapped to a Mercator grid. The color scale is linear and runs from 0 to 1.5 mg/m^3.

Figure 4. The retrieved pigment concentrations along the three tracks on Figures 2 and 3: (a) Track 1; (b) Track 2; (c) Track 3.

Figure 5. Comparison of the normalized water-leaving reflectance ratio (490 to 555 nm) between the model used in the SOA ("Semi-analytic model") and the model used in the STD ("OC2"). Note that for given water reflectances, the Semi-analytic model predicts a smaller pigment concentration than OC2 for $C \lesssim 1$ mg/m^3.

Figure 6. Relative difference (in %) between the pigment concentrations computed for the two days, e.g., Eq. (10). The left panel is for the SOA and the right panel for the STD.

Figure 7. Same as Figure 6 for nLw: top panels 443 nm; bottom panels 555 nm.

Figure 8. The retrieved nLw's for two of the three tracks on Figures 2 and 3: (a) Track 2; (b) Track 3.

Figure 9. SOA-retrieved b^0 (actually f). The color scale is linear and runs from $f = 0.4$ to $f = 1.5$.

Figure 10. SOA-retrieved ν (upper panels) and ω_0 at 865 nm (lower panels). Both color scales are linear and run from $\nu = 2.0$ to 4.5 and $\omega_0 = 0.6$ to 1.0.

Figure 11. SOA-retrieved $\tau_a(865)$ (upper panels) and the SOA cost function S_{LSQ} (lower panels). Both color scales are linear and run from $\tau_a = 0$ to 1 and $S_{LSQ} = 0$ to 40%.

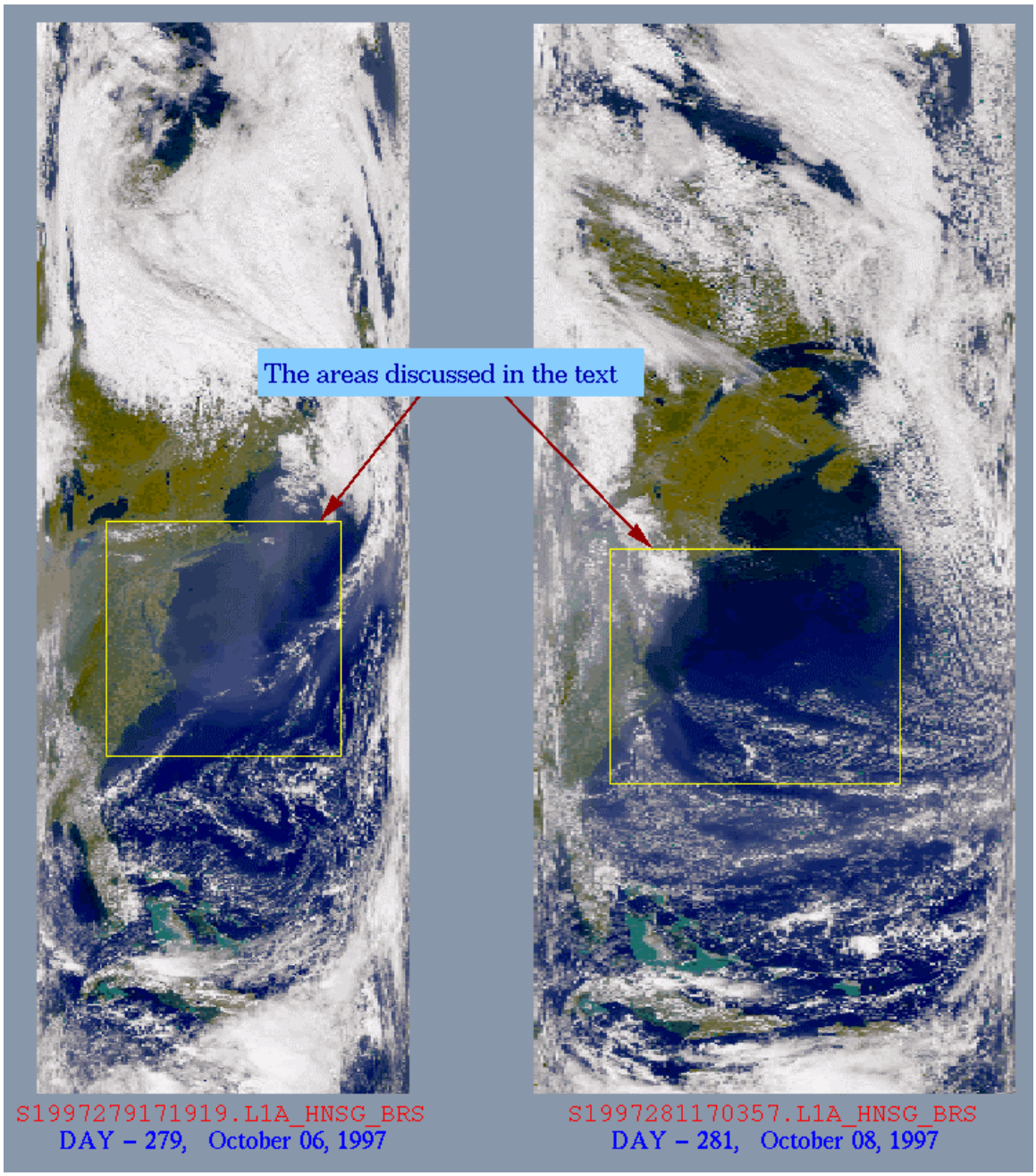

Figure 1. “True” color rendition of the SeaWiFS imagery from October 6 and October 8, 1997.

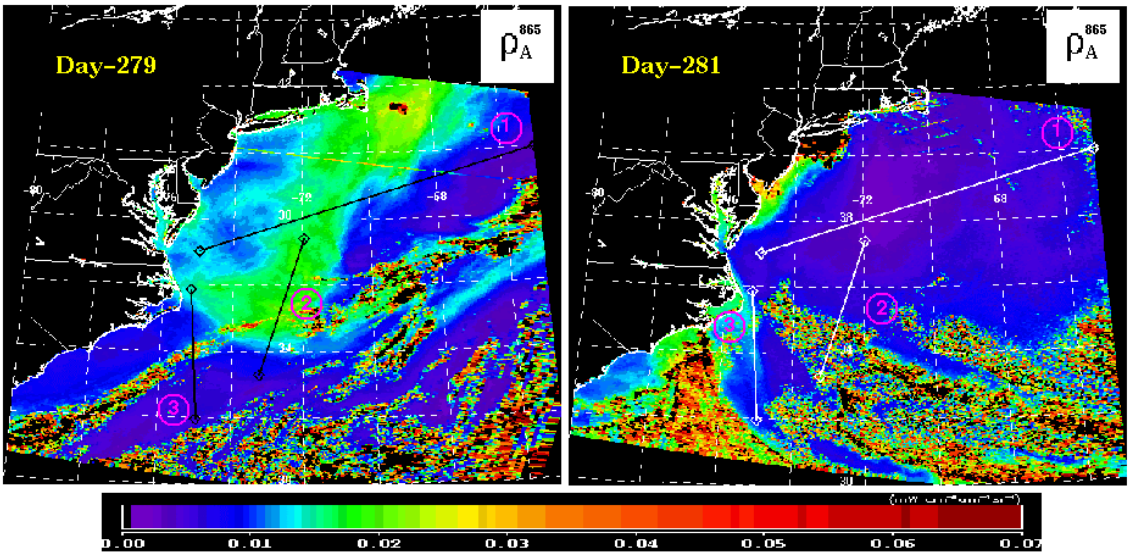

Figure 2. The aerosol reflectance at 865 nm [$\rho_A(865)$] along with three tracks from which processed data will be extracted. Note the significant difference in $\rho_A(865)$ between the two days.

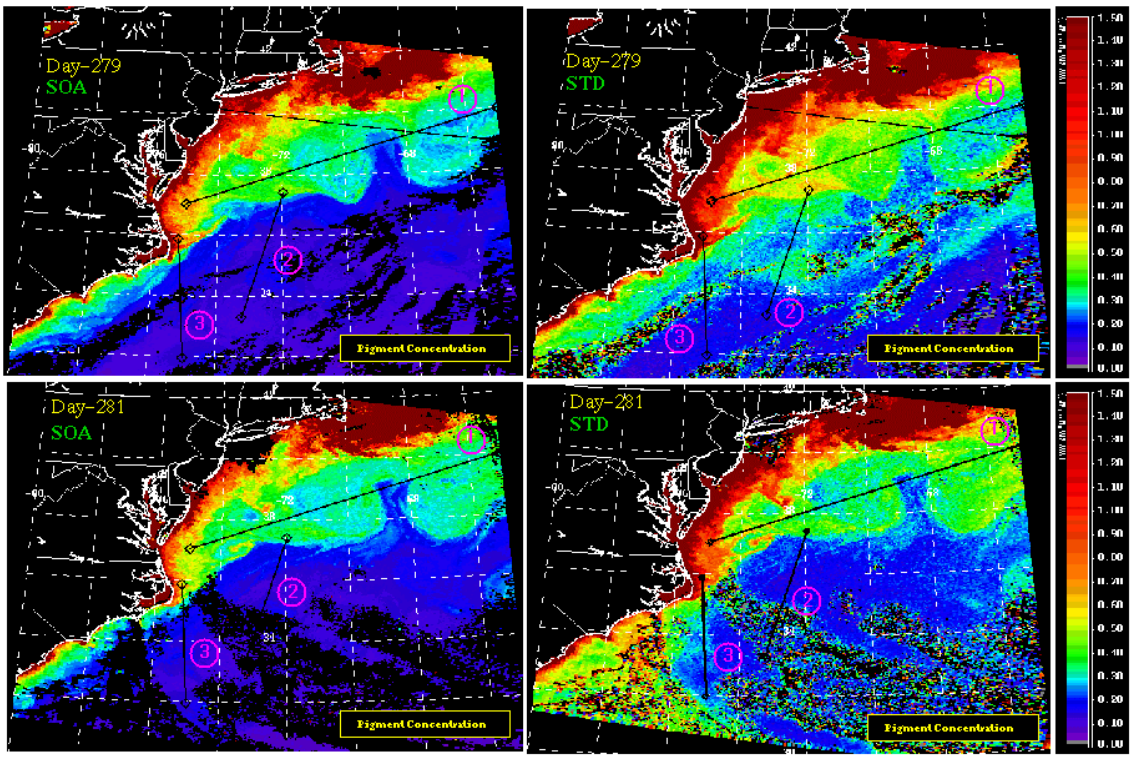

Figure 3. Pigment concentration retrieved for Days 279 and 281 using the SOA (left panels) and STD (right panels). The image has been remapped to a Mercator grid. The color scale is linear and runs from 0 to 1.5 mg/m^3.

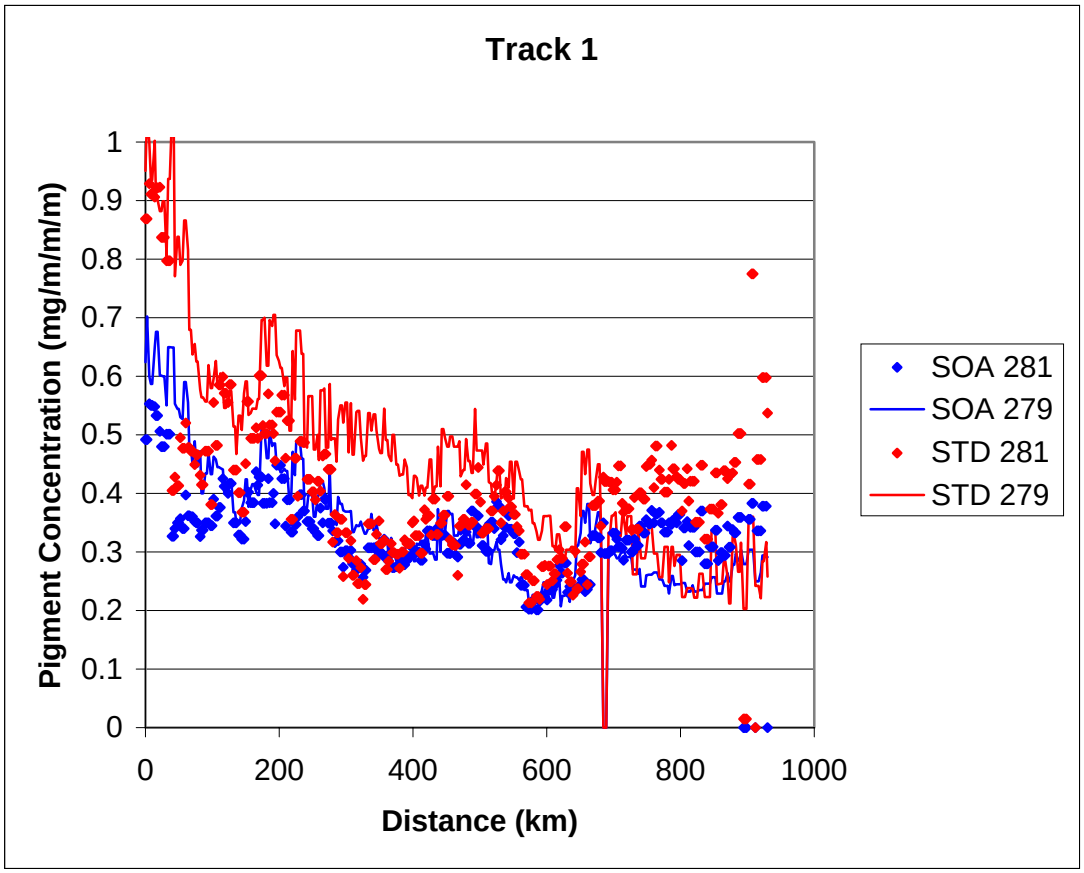

Figure 4(a). The retrieved pigment concentration along the three tracks on Figures 2 and 3. (a) Track 1, (b) Track 2, (c) Track 3.

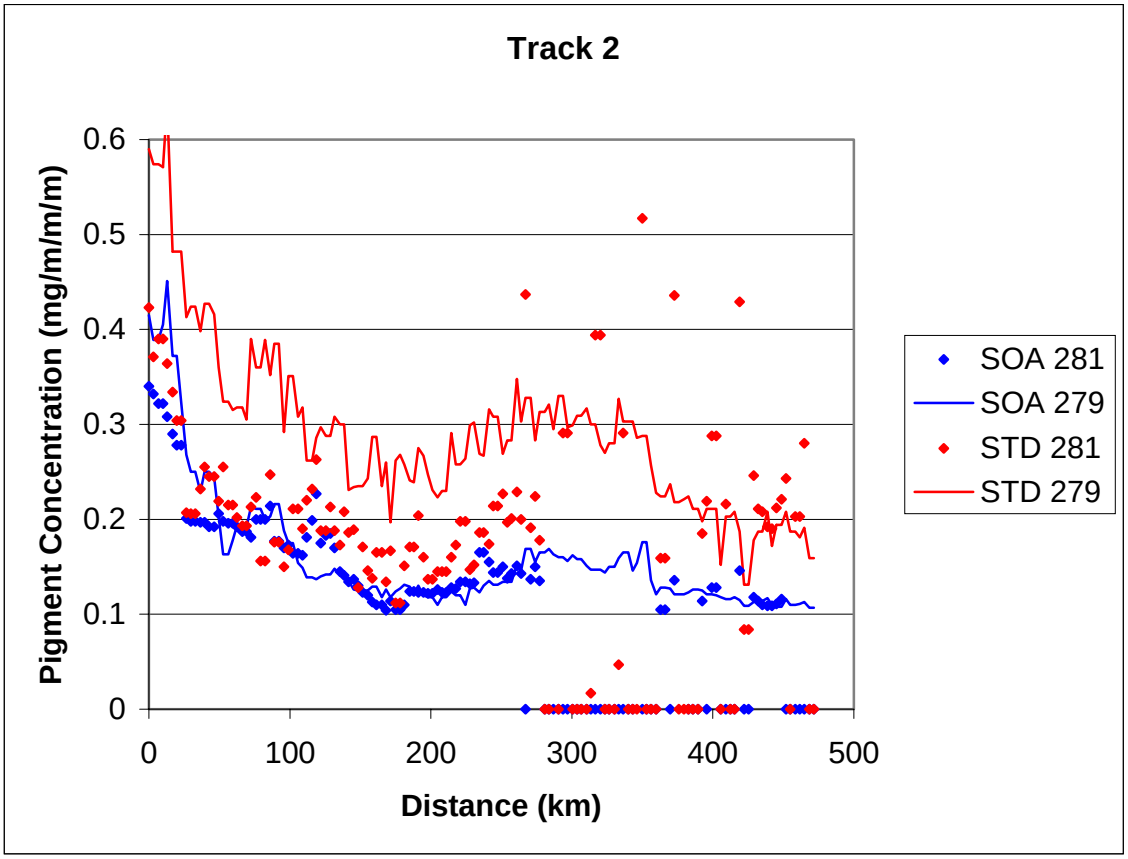

Figure 4(b). The retrieved pigment concentration along the three tracks on Figures 2 and 3. (a) Track 1, (b) Track 2, (c) Track 3.

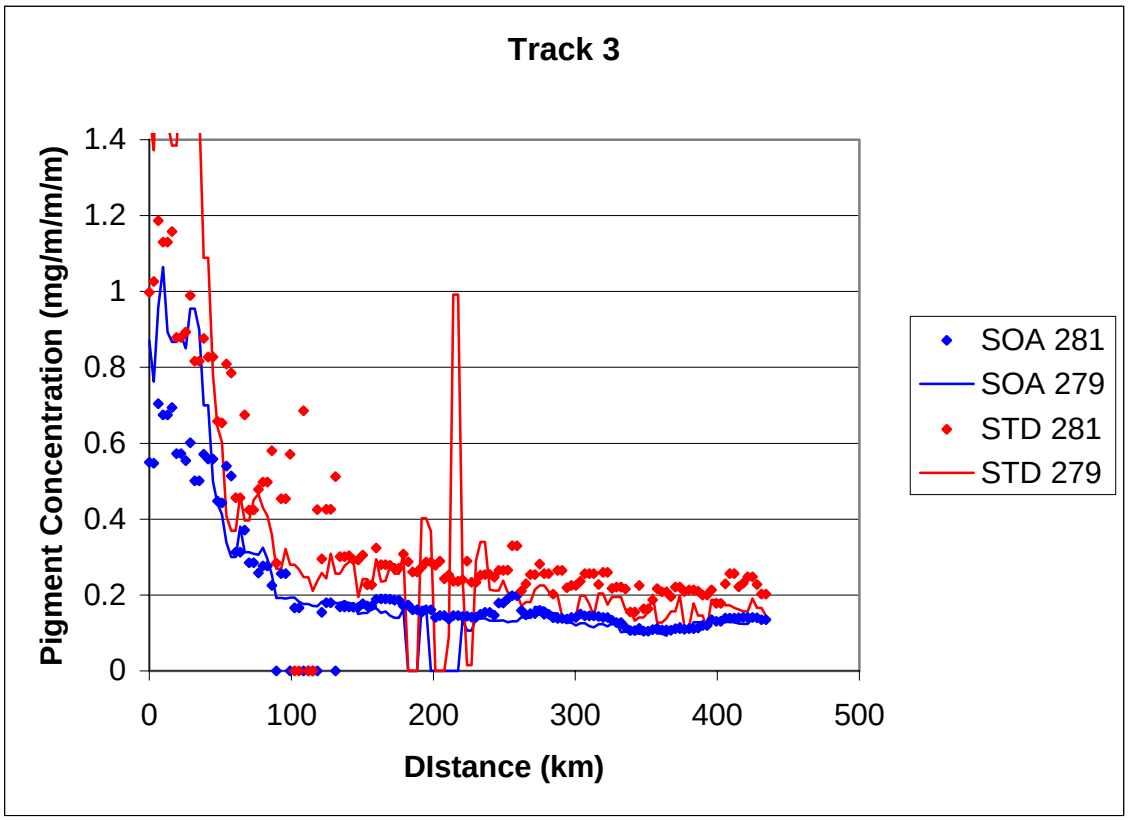

Figure 4(c). The retrieved pigment concentration along the three tracks on Figures 2 and 3. (a) Track 1, (b) Track 2, (c) Track 3.

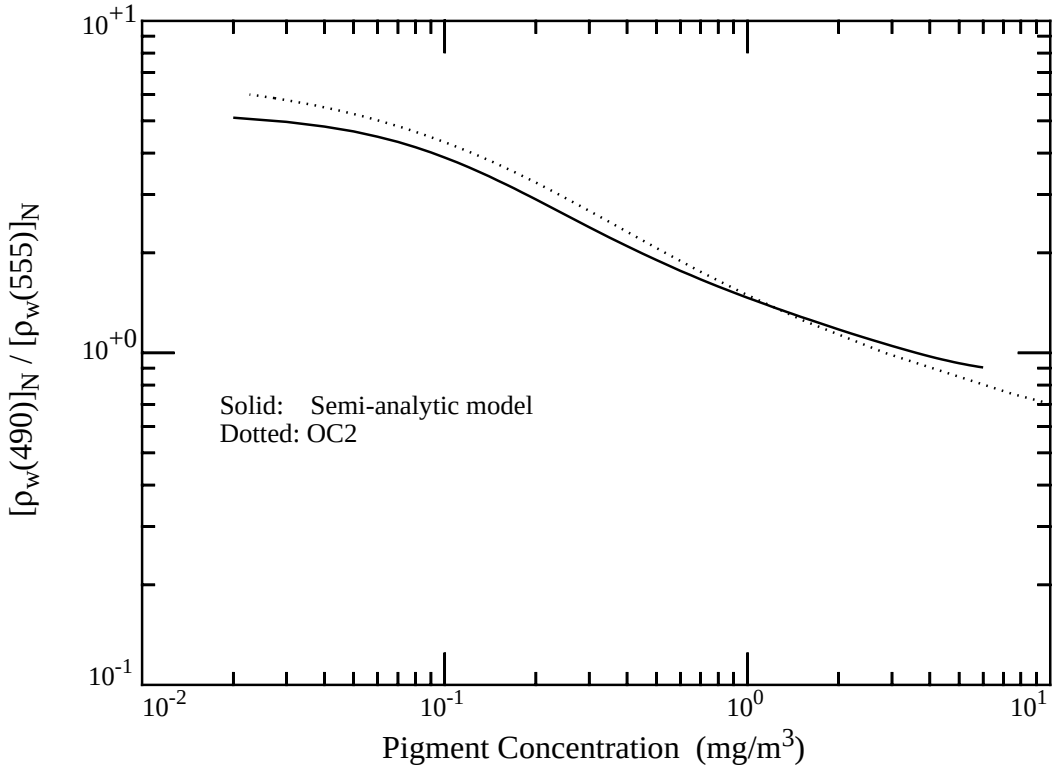

Figure 5. Comparison of the normalized water-leaving reflectance ratio (490 to 555 nm) between the model used in the SOA ("Semi-analytic model") and the model used in the STD ("OC2"). Note that for given water reflectances, the Semi-analytic model predicts a smaller pigment concentration than OC2 for $C \lesssim 1$ mg/m^3.

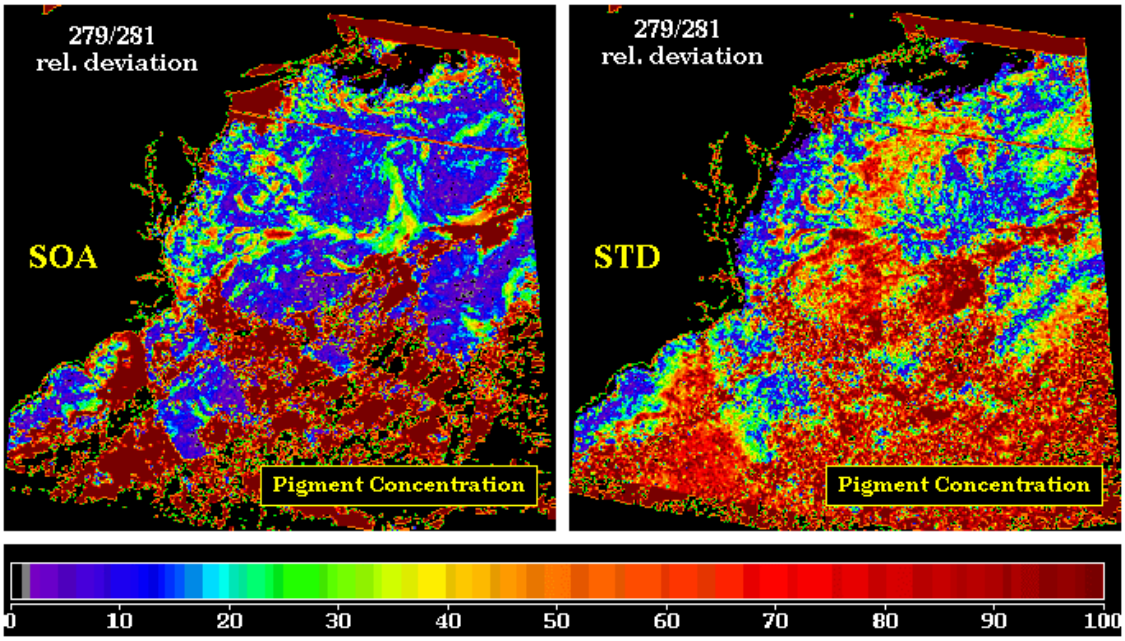

Figure 6. Relative difference (in %) between the pigment concentration computed for the two days, i.e., Eq. (10). The left panel is for the SOA and the right panel for the STD.

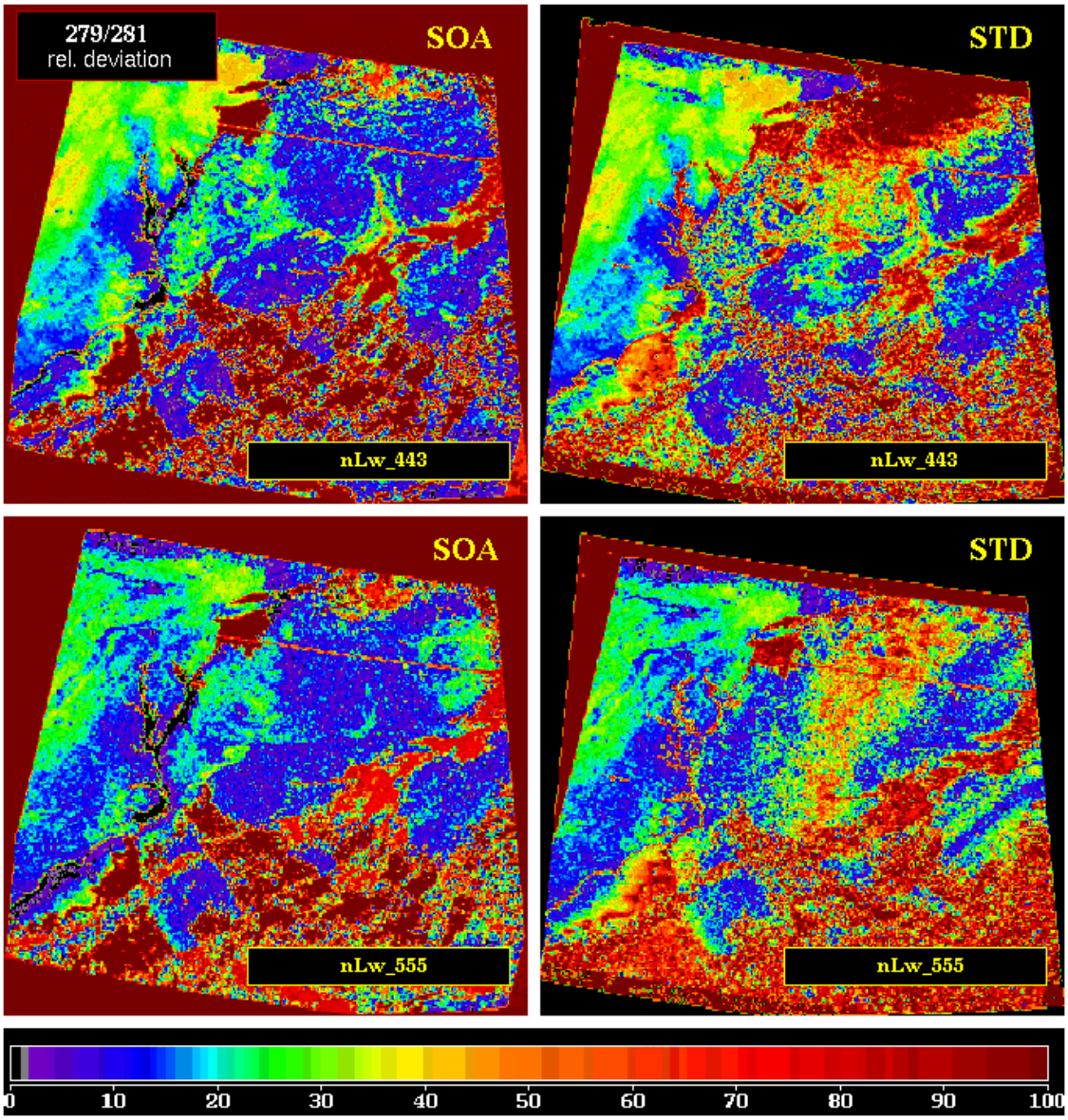

Figure 7. Same as Figure 6 for *nLw*: top panels 443 nm; bottom panels 555 nm.

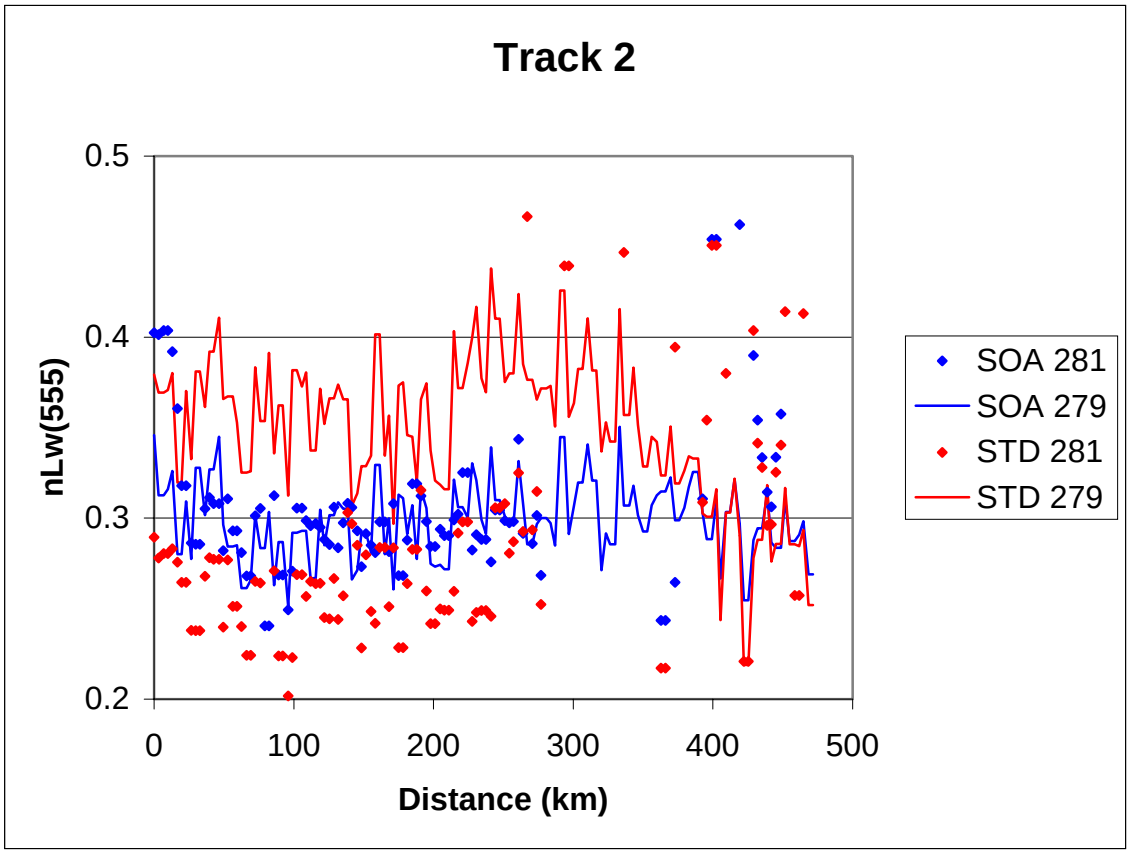

Figure 8(a). The retrieved *nLw*'s for two of the three tracks on Figures 2 and 3: (a) Track 2; (b) Track 3.

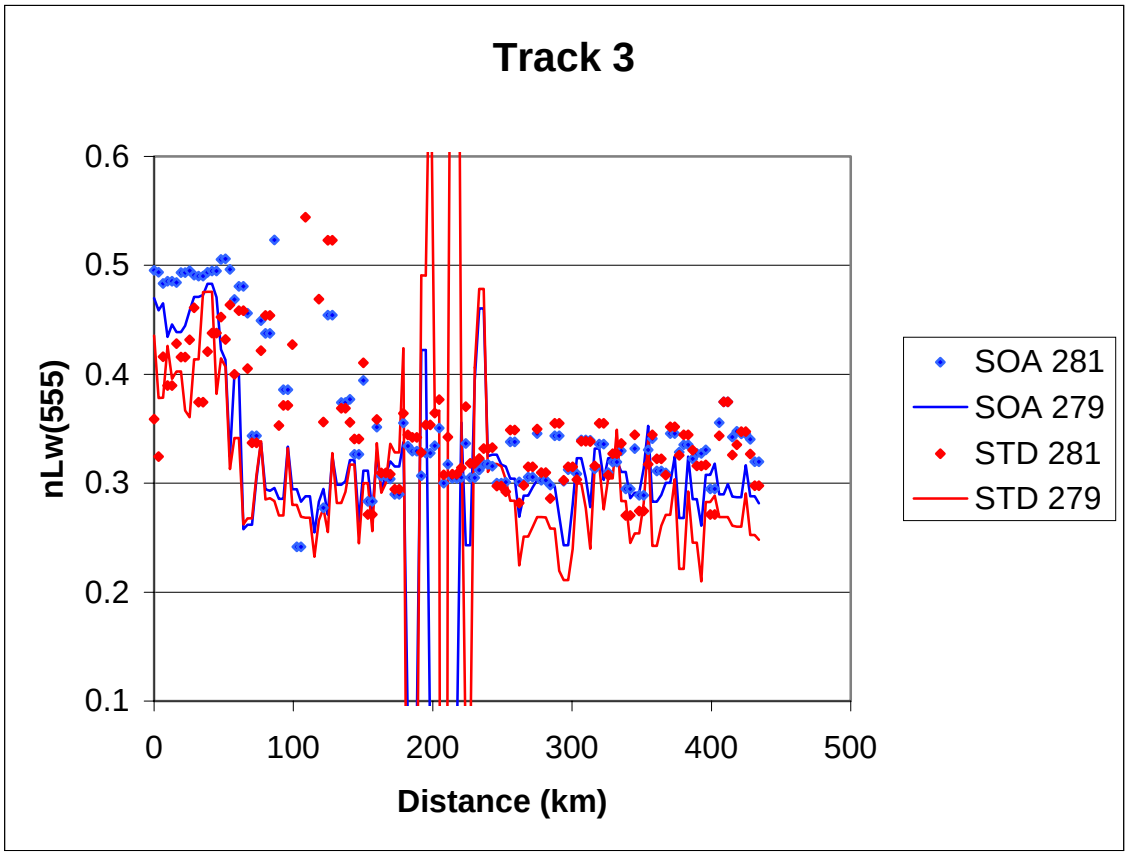

Figure 8(b). The retrieved *nLw*'s for two of the three tracks on Figures 2 and 3: (a) Track 2; (b) Track 3.

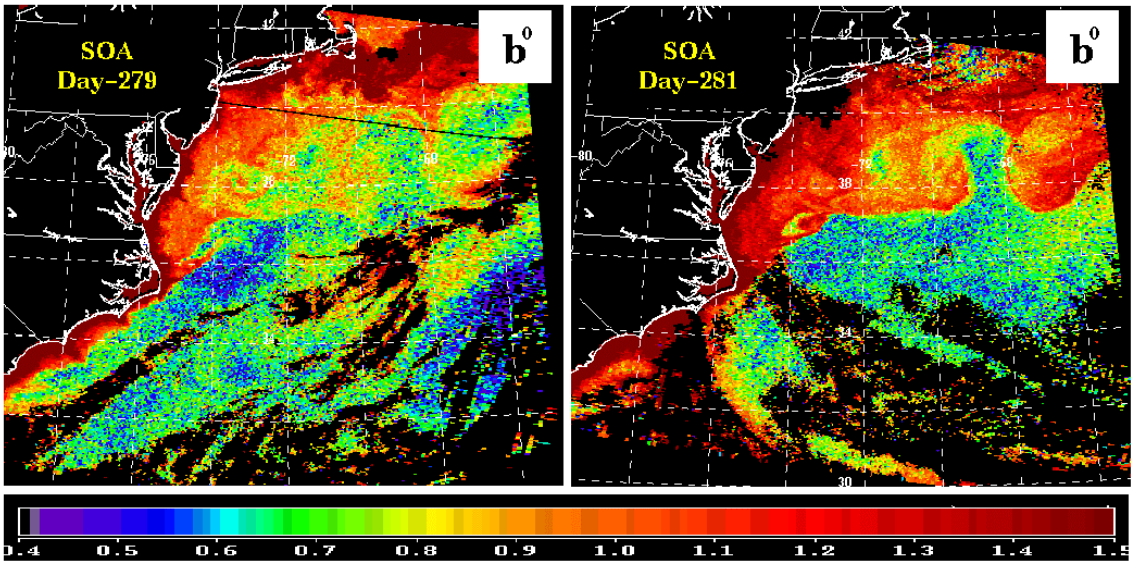

Figure 9. SOA-retrieved b^0 (actually f). The color scale is linear and runs from $f = 0.4$ to 1.5.

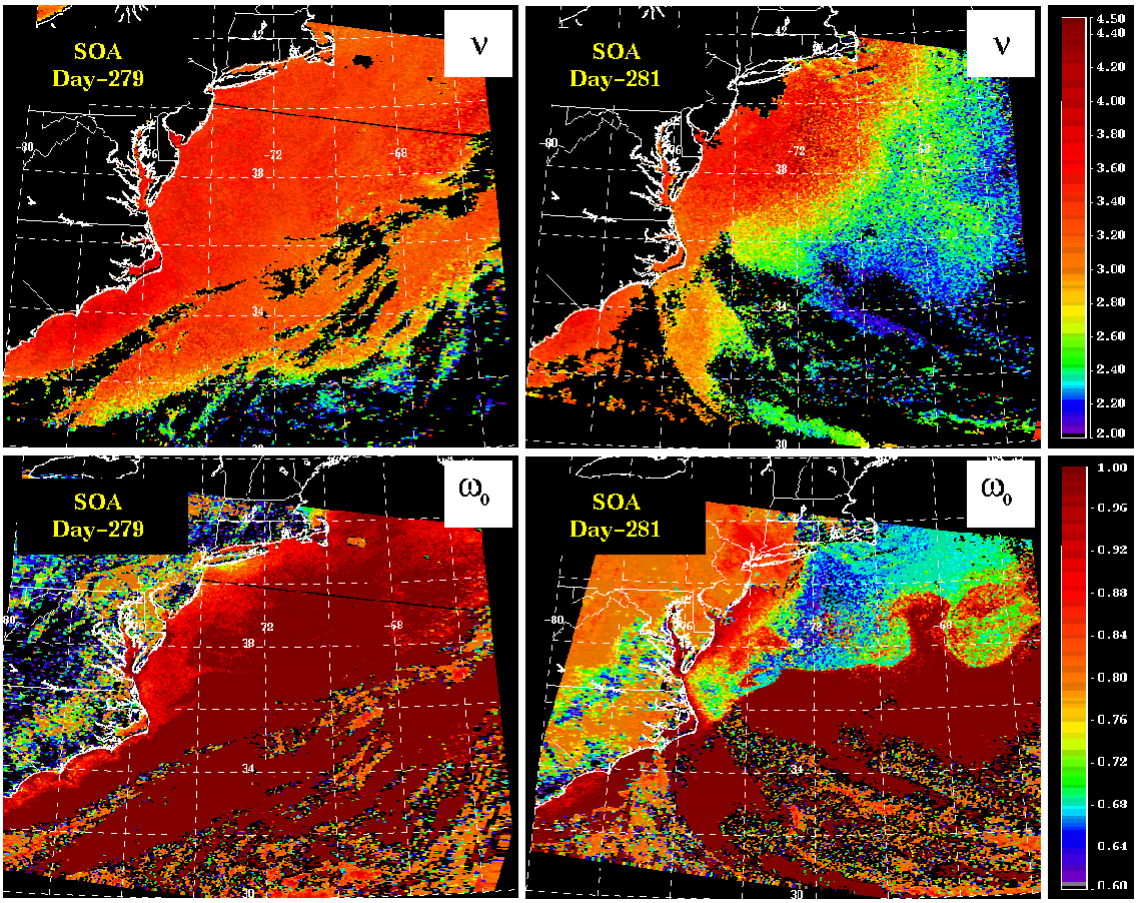

Figure 10. SOA-retrieved ν (upper panels) and ω_0 (lower panels). Both color scales are linear and run from ν = 2.0 to 4.5 and ω_0 = 0.6 to 1.0.

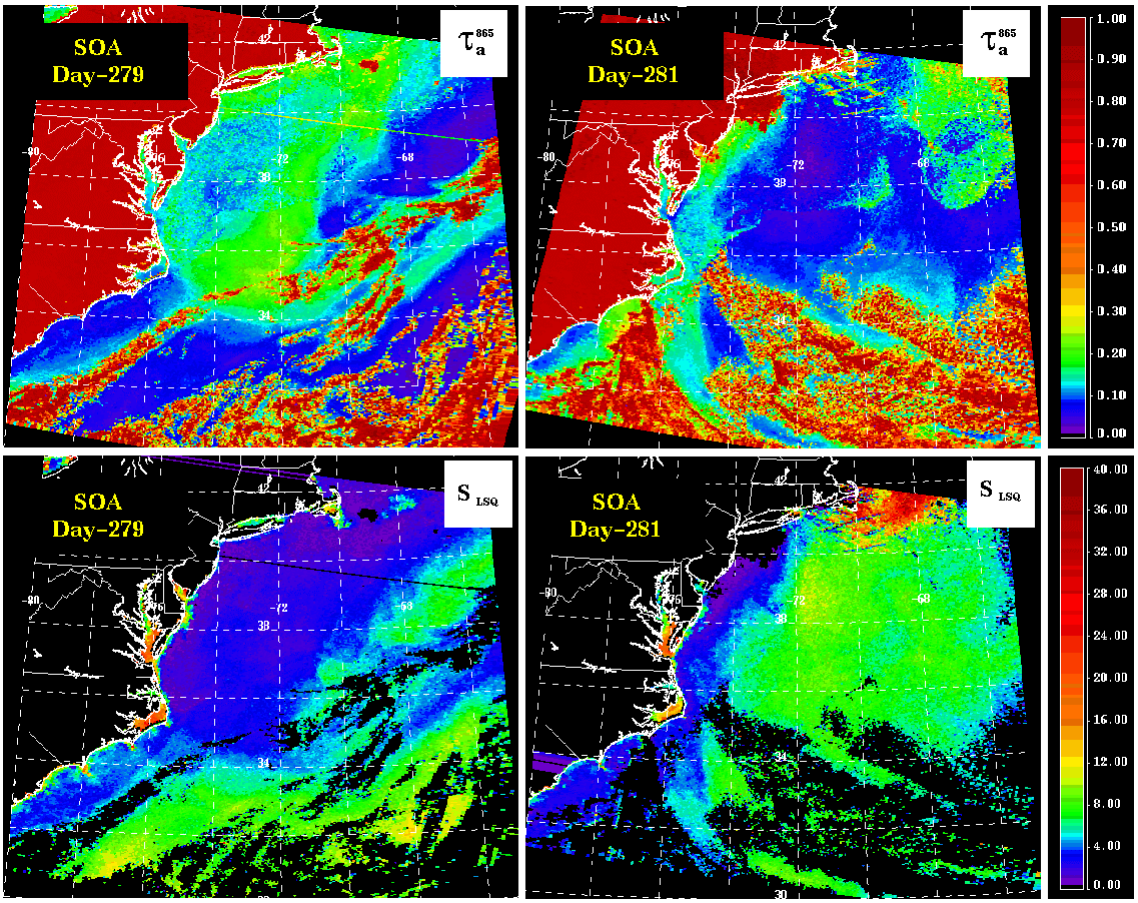

Figure 11. SOA-retrieved $\tau_a(865)$ (upper panels) and the SOA cost function S_{LSQ} (lower panels). Both color scales are linear and run from $\tau_a(865) = 0$ to 1, and $S_{LSQ} = 0$ to 40%.

Appendix V

Aerosol Optical Depth Measurements During the Aerosols99 Experiment

(Submitted to *Journal of Geophysical Research*)

Aerosol Optical Depth measurements during the Aerosols99 experiment

Kenneth J. Voss*(1), Ellsworth J. Welton(2), Patricia K. Quinn(3,4), Robert Frouin(5), Mark Miller(6), and R. Michael Reynolds(6)

(1) Department of Physics, University of Miami, Miami, Fl.

(2) SSAI, NASA-GSFC, Code 912, Greenbelt, Md.

(3) Pacific Marine Environmental Laboratory, NOAA, Seattle, Wa.

(4) Joint Institute for the Study of Atmosphere and Ocean, University of Washington, Seattle,Wa.

(5) Scripps Institution of Oceanography, University of California San Diego, La Jolla, California

(6) Environmental Sciences Department, Brookhaven National Laboratory, Upton, NY.

Running title: AOD during Aerosols99

*Corresponding author email address: voss@physics.miami.edu

GAP index numbers: 0305, 0394, 0649, 3360, 9325

Submitted to J. Geophysical Res., 6/28/00, Aerosols99 special issue

Abstract

The Aerosols99 cruise took place during the period from January 14 to February 8, 1999 on the R/V Ron Brown. The cruise track was almost a straight line from Norfolk, Va. to Cape Town, South Africa and afforded the opportunity to sample several different aerosol regimes over the North and South Atlantic. Handheld sunphotometers, a shadowband radiometer (FRSR), and a LIDAR were used to measure the Aerosol Optical

Depth (AOD) during the cruise. The AOD and angstrom exponent (spectral dependence of the AOD) varied strongly between regimes. Maritime regions typically had AOD (500nm) of approximately 0.10± 0.03, with angstrom exponents around 0.3± 0.3. An African dust event was encountered in which the AOD(500nm) averaged 0.29± 0.05 with an angstrom exponent of 0.36± 0.13. At the ITCZ, no measurements were obtained because of cloudiness, however after the ITCZ we encountered a biomass burning aerosol with high average AOD(500nm) of 0.36± 0.13, and a high angstrom exponent (0.88± 0.30). Further south the aerosol went back to the low levels of a typical marine aerosol.

1. Introduction

The Aerosols99 cruise took place during the period from January 14, to February 8 1999 on the R/V Ron Brown, and on a cruise track from Norfolk, Va. to Cape Town, South Africa. This track afforded the opportunity to sample several different aerosol regimes over the North and South Atlantic. A suite of chemical and optical instrumentation was used during this cruise to measure the physical, chemical, and optical properties of the aerosols over this region. This paper will concentrate on the Aerosol Optical Depth (AOD) measurements obtained during the cruise.

There were many different instruments making measurements of the spectral AOD during this cruise. Three groups used Microtops Sunphotometers (Solar Light Co., Philadelphia, PA): the Brookhaven National Laboratory[BNL], Pacific Marine Environmental Laboratory [PMEL], and the University of Miami group used a Microtops on this leg supplied by the SIMBIOS [Mueller et al., 1998] instrument pool. The Microtops sunphotometers are hand held instruments which, when manually aimed at the sun, make measurements of the direct solar irradiance to derive the AOD. There was

another combination sunphotometer and radiometer, the Simbad instrument operated by a group from Scripps which was also was manually operated and, for the AOD measurements, operated in the same way as the Microtops instruments. BNL also had a FRSR shadowband radiometer on board [Reynolds et al., 2000]. This instrument operates automatically throughout the day making measurements of the indirect and direct solar irradiance which are individually averaged at 2-minute intervals. Finally there was a Micropulse LIDAR operating continuously throughout this cruise making vertical profiles of the backscattering/attenuation profile at 1 minute intervals. Each of these instruments has distinct advantages and disadvantages.

To measure the AOD with a radiometer, there must be a cloudfree line of site to the sun. Since the handheld instruments (Microtops and Simbad radiometer) are manually operated, the operator can select cloudfree periods to perform the measurements, visually avoiding cloud contamination. However the need for an operator results in fewer measurements than is possible with an automated instrument. The FRSR takes measurements throughout the day automatically, thus any cloud free periods during the day will be sampled. However since there is no operator continually monitoring the measurements, algorithms must be developed to screen the processed data for cloudy periods. A calibrated Micropulse LIDAR (MPL) allows measurements of the boundary layer AOD even during periods of cirrus clouds. In addition, since this is an active measurement, the AOD can also be measured during the night, while all the other methods require the sun. However this method also requires an algorithm to avoid periods of lower level clouds and requires a clean, aerosol free layer be defined above the

aerosol. The MPL also only supplies the AOD at one wavelength, thus there is no information on the spectral variation of the AOD.

In this paper we will present an overview of the methods used to obtain the AOD with each of these instruments. In addition we will look at how the AOD and the spectral variation of the AOD was influenced by the different aerosol optical depth regimes sampled during this cruise. Other associated papers will look at the relationship between the AOD and surface measured aerosol properties [Quinn et al., this issue] and at the vertical profile information from the LIDAR [Voss et al., this issue].

2. Methods

There are a few definitions, which are common to all the measurements, that can be detailed first. The aerosol optical depth (AOD) is defined as the attenuation for a vertical path through the atmosphere due to the aerosols and is a portion of the total optical depth. The total optical depth, τ, is defined as:

$$\tau = -\frac{1}{m}\ln(\frac{E}{E_o}) \qquad (1)$$

where E_o is the extraterrestrial solar irradiance (solar irradiance that would be measured in the absence of an atmosphere), E is the surface measured direct solar irradiance, and m is the airmass or relative pathlength over which the measurement was performed. m is related to the solar zenith angle, θ_s, and at small solar zenith angles is equal to $1/\cos(\theta_s)$. Note at large zenith angles (greater than 70 degrees), because of the effect of earth curvature, the relationship between solar zenith angle and air mass is more complicated (Kasten and Young, 1989).

Once τ is determined, the AOD can be determined by subtracting the contributions to τ from molecular scattering (Rayleigh scattering, τ_R) [Penndorf, 1957] and molecular absorption. The spectral regions measured are usually chosen to avoid regions of strong molecular absorption, but the broad Chappius band absorption of O_3 requires that corrections be made for O_3 absorption [Shaw, 1979]. Once O_3 absorption, τ_{O3}, is determined the AOD can be found by:

$$AOD = \tau - \tau_R - \tau_{O3}. \quad (2)$$

These parameters vary with the wavelength of light, hence the measurement wavelength must be taken into account. The spectral variation of the AOD can be characterized by the angstrom exponent, α, defined as:

$$\alpha = -\frac{\ln(\frac{AOD(\lambda_1)}{AOD(\lambda_2)})}{\ln(\frac{\lambda_1}{\lambda_2})} \quad (3)$$

λ_1 and λ_2 are two measurement wavelengths. The angstrom exponent is related to the size distribution of the aerosol, small values imply a low spectral variation and large particles, large α implies high spectral variation and more smaller particles. Measurement of the AOD is a column averaged measurement, thus α derived from the AOD is determined by the column averaged aerosol size distribution.

Details of the specific instrumentation and the methods used to calibrate and reduce the data from these instruments will now be described.

2.1 Microtops

The 5-channel handheld Microtops sunphotometer (Solar Light Co.) used by NOAA PMEL operated at 380, 440, 500, 675, and 870 nm. The full angular field of view is 2.5 deg. The instrument has built in pressure and temperature sensors and was operated with a GPS connection to obtain position and time of the measurements. A MATLAB routine, also used by the NASA SIMBIOS program and Brookhaven National Laboratory, was used to convert the raw signal voltages from the Microtops to aerosol optical depths. Included in the conversion is a correction for Rayleigh scattering [Penndorf, 1957], ozone optical depth, and an air mass that accounts for the Earth's curvature [Kasten and Young, 1989]. Ozone column amounts used to calculate the ozone optical depth were based on ozonesonde measurements made during the cruise [Thompson et al., 2000] and, to fill in data gaps, TOMS level 3 data. The instrument was calculated using a Langley plot approach [Shaw, 1983] by the manufacturer prior to the cruise and again at Mauna Loa 5 months after the cruise. Calibration constants for the 5 wavelengths differed by less than 0.9% between the two calibrations, which corresponds to approximately 0.01 in optical depth.

2.2 Simbad

The Simbad radiometer was designed to collect data on aerosol optical depth and water-leaving radiance, the basic satellite ocean-color variables [Schwindling et al., 1998]. Radiance is measured in five spectral bands centered at 443, 490, 560, 670, and 870 nm, total field-of-view is 3 degrees, and frequency of measurements is 10 Hz. In sun-viewing mode, the instrument functions like a standard sun photometer, the only difference being that the optics are fitted with a vertical polarizer. This polarizer reduces

reflected skylight and sunglint in the field-of-view when the instrument is operated in sea-viewing mode. The polarizer is not an issue for sun intensity measurements, because direct sunlight is not polarized. It takes 10 seconds to acquire a data set in sun-viewing mode. Only the highest intensity during one-second (i.e., out of 10 measurements) is stored automatically, to avoid pointing errors on a moving platform. Measurements were made systematically from the bow of R/V Ron Brown when the solar path was free of clouds, and repeated three times to reduce experimental errors.

Radiometric calibration was performed four times before and twice after the experiment at Stevenson Peak (1,896 m), California using the Bouguer-Langley method. No significant trend was detected in the calibration coefficients. The average log-transformed numerical counts and standard errors after correction for Earth-Sun distance are 12.656 ± 0.008, 13.014 ± 0.021, 12.906 ± 0.007, 12.920 ± 0.005, and 12.596 ± 0.008 at 443, 490, 560, 670, and 870 nm, respectively. The standard error is a measure of the expected error on aerosol optical thickness due to calibration for an air mass of unity. This error is inversely proportional to air mass. Except for the 490 nm spectral band, the standard error is below 0.01 in optical depth.

Errors in molecular optical depth and ozone absorption will reduce the accuracy of aerosol optical depth retrievals. Also, some scattered light may reach the detectors because of the relatively large field-of-view (3 degrees), artificially increasing atmospheric transmittance and, thus, decreasing aerosol optical depth. A 1% error on the molecular optical depth at standard pressure and a 10hPa error on surface pressure would give, for an air mass of 1, a 0.005 error in aerosol optical depth at 443 nm, decreasing to practically zero at 870 nm. To compute ozone absorption, vertical ozone amount was

taken from ozone sondes deployed during the cruise [Thompson et al., 2000]. A 10% error in ozone amount would translate into optical depth errors of 0.003 at 560 nm and 0.001 at 670 nm, and negligible (or nil) in the other spectral bands. These errors, computed for an air mass of unity, increase with air mass. Regarding scattered light, contamination is small in the presence of continental aerosols (i.e., <0.001 and 0.003 at 443 nm for an optical thickness of 0.05 and 0.2, respectively), but may be five to ten times larger in the presence of maritime aerosols, due to the more pronounced forward peak of the phase function. Although some errors may compensate, the absolute error on aerosol optical depth is probably of the order of 0.02 (0.03 at 490 nm). Since the absolute error is independent of optical depth, the relative error is inversely proportional to optical depth, and becomes very large at low optical depth (e.g., about 50% at 443 nm for an optical depth of 0.04).

2.3 Fast-Rotating Shadowband Radiometer

A shadowband radiometer measures the diffuse and global (upper hemispheric) irradiance and computes E as the difference between the two. The device gets its name from the hemispherical metal strip that rotates around the detector (the shadowband) and blocks the direct solar beam to yield a signal that is from the sky only (after the effect of the arm is included).

The multiple wavelength rotating shadow-band radiometer [Harrison et al.,1994] uses independent interference-filter-photodiode detectors and an automated rotating shadow-band technique to make spatially resolved measurements at seven wavelength pass-bands. A marine version of the multiple wavelength rotating shadow-band radiometer has been developed at the Brookhaven National Laboratory (BNL). The BNL

marine version uses a slightly modified version of the detector used for continental applications. It has seven channels: one broadband silicon detector and six ten-nm-wide channels at 415, 500, 610, 660, 870, and 940 nm. Modifications to the detector circuitry used for continental applications are necessary because the response time of the original circuitry is too slow for use on a moving ship. If the response time of the detector is too slow, wave action may cause the orientation of the radiometer to change appreciably during the time the shadow-band is occulting the sun. The rotation of the shadow-band itself must be sufficiently fast for the same reason. The marine version of the shadow-band radiometer is hereafter referred to as the BNL Fast-Rotating, Shadow-band Radiometer (FRSR).

The shadow-band radiometer must properly measure the global and diffuse irradiances from which the direct-beam irradiance is derived by the subtraction

$$E_H = E_G - E_D \qquad (4)$$

where E_H is the direct-beam irradiance projected onto a horizontal plane, E_G is the global irradiance on the horizontal plane, and E_D is the diffuse irradiance from non-forward scattering. The global irradiance, E_G, is measured when the band is out of the field of view and the sensor is exposed to full sunlight while E_D is measured with the sensor shadowed by the band. The irradiance normal to the incident beam, E in Eq. 1 is computed by

$$E = E_H / \cos(\theta_s). \qquad (5)$$

Corrections for the sky blocked by the occulting band and for roll and pitch of the sensor head are made and discussed in detail in Reynolds et al. [2000]. The instrument

calibration coefficients for Aerosols99 were determined using the Langley technique at Mauna Loa. Additional calibrations were performed during the cruise that showed good agreement with the Mauna Loa data. The accuracy of the calibration coefficients is thought to be about 5% and the accuracy of the irradiance measurements about 6%. While the uncertainty in the AOD measurement also depends on the air mass, for typical conditions, measurements of the AOD of sea-salt aerosol (due to its low AOD) are the most uncertain.

Cloud filtering is the most important challenge for FRSR data processing. Because the FRSR operates autonomously, cloud observations are naturally part of the signal that must be processed to obtain τ. The cloud filter that is currently used is based on two steps: computing signal statistics over windows of periods of less than two hours and using these statistics to judge the quality of the observation under consideration. If the standard deviation of the observations in a two-hour moving window is less than 0.05, a subjectively defined threshold, and the observation at the center of the window is also less than 0.05, the central observation is accepted. The underpinning of this cloud filtering technique is that τ is relatively constant over a period of two hours, while the cloud signal is highly variable. This approach has proven relatively successful, although improvements in the filter are expected in the future.

2.4 Micropulse LIDAR

The Micropulse LIDAR (SESI, Burtonsville, MD) is a small compact LIDAR system which averages high repetition, low energy pulses to obtain a profile of attenuation/backscattering in the atmosphere [Spinhirne et al.,1995]. The Micropulse

LIDAR used during the cruise operated at 523 nm, with a pulse repetition rate of 2500 Hz, the vertical resolution was 75m, and data was collected to 30km. During the day the signal above 10km became increasingly noisy due to a combination of attenuation in the boundary layer and background sunlight at 523 nm, but during the night low noise data could be obtained to 20km in the absence of clouds. The details of the algorithm to derive the AOD from the micropulse LIDAR are detailed elsewhere [Welton, 1998, Welton et al., 2000]. However an overview of the technique will be presented here.

The basic equation governing LIDAR propagation, when the LIDAR is vertically oriented is:

$$Er(t) = CEo(\beta_r(180,z) + \beta_a(180,z))\exp(-2 * \int_0^z [c_r(z') + c_a(z')]dz') / z^2 \quad (6)$$

Where *Er* is the received energy, *Eo* is the outgoing pulse energy, $\beta_r(180,z)$ is the Rayleigh (molecular) backscattering, $\beta_a(180,z)$ is the aerosol backscattering, c_r is the Rayleigh attenuation, c_a is the aerosol attenuation, and *C* is an instrument calibration constant. The time the signal is received is related to the altitude, *z*, by the time it takes for the LIDAR pulse to travel up to that altitude and back ($z = tc/2$, where c is the speed of light). By using time resolved return signals, profiles of the backscattering and attenuation can be obtained. *C* contains information on system parameters such as throughput, solid angle acceptance of the receiver, divergence of the laser beam and other parameters. While in principal this could be calculated [Spinhirne et al., 1980] in practice it is much simpler and accurate to derive this parameter from measurements in the field, as will be discussed below. For a practical LIDAR system such as the MPL,

there are other important affects which must be taken into account, namely the overlap function and afterpulse function. The overlap function describes the loss in signal strength at close range. Signal loss is due to poor focusing to the detector by the MPL telescope and optical design at close range (less than 4 km). Signals greater than the overlap range are not effected by this problem. The afterpulse function is a result of cross-talk between the laser pulse and detector, as well as dark noise in the system. Both of these effects were corrected for in this data set in the manner described by Welton et al.[2000].

If the calibration coefficient is known, and a clean layer above the aerosol layer can be found where the backscattering and attenuation is dominated by Rayleigh scattering then the returned energy from that altitude is simply:

$$Er(t) = CEo\beta_r(180, z)\exp(-2 * \int_0^z [c_r(z') + c_a(z')]dz') / z^2 \tag{7}$$

Or

$$Er(t) = CEo\beta_r(180, z)\exp(-2 * AOD)\exp(-2 * \int_0^z c_r(z')dz') / z^2 \tag{8}$$

The later integral can be calculated, thus:

$$AOD = -\frac{1}{2}\ln[\frac{Er(t)z^2}{CEo\beta_r(180, z)}] - 2 * \int_0^z c_r(z')dz') \tag{9}$$

The measurement of the AOD with the LIDAR only requires finding a clean layer above the aerosols and accurate calculation of the system calibration constant *C*. It is important to note that this product does not depend on any assumption of the extinction/backscatter ratio (*S*).

When the AOD is known from independent measurements (such as with a handheld sunphotometer), the above equations can be turned around to determine the system calibration constant *C*. During this cruise, during cloud free periods during the day, episodic measurements of the AOD were made with an independent Microtops sunphotometer (the data from this instrument are not included in this paper). Thus the calibration coefficient was determined at intervals throughout the cruise. The calibration coefficient was fit to a linear equation and varied during the cruise by 20%. The accuracy of our calibration procedure is estimated to be +-6%, while the accuracy of the AOD calculation is effected by this calibration coefficient, and the accuracy with which the overlap and afterpulse corrections were made. The accuracy of the AOD determined from the LIDAR is estimated to be + -0.05 in optical depth. The LIDAR AOD calculation has the advantage that for boundary layer aerosols, it is the only method that can determine the AOD during the night and in the presence of high cirrus. Care must be taken in determining the level chosen to represent a clean atmosphere above the aerosol [Welton et al., 2000]. This is usually obvious from the range corrected LIDAR signal by looking for a region for which $\ln[Er(t)*z^2]$ is decaying at the rate appropriate for Rayleigh scattering.

2.5 Derivation of the angstrom exponent

Other than the LIDAR, all of the instruments measure the AOD at multiple wavelengths close to simultaneously. For each of these instruments the angstrom exponent was calculated using all the usable channels for that instrument (some channels in specific instruments were not calibrated well, and were not included). The angstrom exponent was calculated by determining the least squares fit to the line:

$$\ln(\mathrm{AOD}(\lambda)) = B - \alpha \ln(\lambda), \tag{10}$$

for each measurement set (a set being the available wavelengths for a single instrument at a given time). This was done throughout the data set, for each instruments AOD measurement.

2.6 Compilation to averages for the days.

All the independent measurements of the AOD were compiled into a single data set as shown in Figure 1, choosing the AOD at the wavelength of each instrument closest to 500nm. No effort was made to correct for the small wavelength differences between the instruments. The largest wavelength difference was from 490nm to 523 nm, and with the highest average angstrom exponent (1.2) this is only a 5% effect. As can be seen the AOD varied strongly throughout the cruise depending on the atmospheric influences. The divisions into regions were determined by the meterological data, calculated back trajectories, trace gas distributions, and surface aerosol chemical and physical data [Bates et al, this issue]. These regions will be discussed in more detail in the next section. For comparison with the other data sets obtained, an average AOD and α for 1/4 day intervals during the cruise had to be determined. For Region 4 and 1/28/99, because of almost

constant cloud cover, there was virtually no opportunity to measure the AOD with any technique. For the rest of the cruise the average AOD and angstrom exponent were calculated at 1/4 day intervals centered on Midnight, 0600, 1200, and 1800 UTC.

To determine the average AOD for a period, a 3rd order polynomial was fit to 1.5 days of data centered on the desired time. This polynomial was then used to interpolate the AOD for the desired 1/4 day interval in increments of 1/200 day. For each period this interpolated function was averaged to determine the AOD and is shown in Figure 1. For noon and midnight (even and 0.5 day increments) the AOD is listed in Table 1. This method was chosen to provide a true time average during that period and to avoid biasing the average towards periods of many measurements. To get an estimate of the accuracy of these averages, the standard deviation of the difference between this average and the original data was determined. This standard deviation is shown in the figure as the error bars on the average AOD data, and in Table 1.

The Angstrom exponent, α, was determined by simply averaging the data during the relevant period, and is shown in Fig. 2. We chose to do this, rather than the method chosen for AOD because the differences between separate measurements of α appeared random. The errors bars on these graphs are determined by the standard deviation between this average and the original data. The angstrom exponents and standard deviation are also shown in Table 1. There are more periods without α data than for the AOD since there were times when only the LIDAR obtained AOD measurements (for example at night), and the LIDAR does not obtain α.

3. Results and discussion

We will first look at a comparison of the different instruments, then look at specific regions of the cruise.

3.1 Instrument comparison

To investigate the variation in measurements between the different instruments, we looked at three different days when the AOD appeared stable throughout the day. We chose to do this so that we could get representative samples of each instrument. It was difficult to find a time when all the instruments were working at exactly the same time, because the handheld sunphotometers were most active at noon when the LIDAR was turned off because of the low solar zenith angle. The three periods chosen were Day-of-Year (DOY) 25, 30, and 37 (this corresponds to latitude ranges of 9.8° N – 6.9° N, 5.6° S – 8.9° S, and 27.8° S – 30.4° S respectively).

Figure 3 shows the comparison between the instruments. In this figure the AOD(500nm) is displayed for each instrument along with the standard deviation for the individual instrument. We also show the average of the measurements during each day. The averages, and standard deviations for each day are: 0.31 $\pm$0.03, 0.13$\pm$0.02, and 0.10 $\pm$ 0.02. It is interesting that the more standard handheld sunphotometers (the Scripps Simbad, and the BNL and PMEL Microtops) had a constant difference (to within $\pm$0.01) between them, as would be expected with small calibration offsets. The relationship between these instruments and the non-traditional LIDAR and FRSR varied between the days chosen however. It should be pointed out that the LIDAR and FRSR were averages

over longer periods (throughout the day for the LIDAR, and during daylight with the FRSR). But overall the instruments agreed fairly well.

This uncertainty may affect the predictions of radiative forcing. In cloud-free regions, the direct radiative forcing due to aerosols can be expressed as [e.g., Iacobellis et al., 1999]:

$$F = \mu_0 E_0 T_a^2 G \tag{11}$$

with

$$G = R + T^2 A_s/(1 - A_s R) - A_s \tag{12}$$

$$R = \omega_o \beta[1 - \exp(-AOD/\mu_0)] \tag{13}$$

$$T = \exp(-AOD/\mu_0) + \omega_o (1 - \beta)[1 - \exp(-AOD/\mu_0)] \tag{14}$$

where μ_0 is the sun zenith angle, E_0 is the extraterrestrial solar flux, T_a is the transmittance of the atmosphere above the aerosols, A_s is the albedo of the underlying surface, R and T are the fraction of sunlight scattered and transmitted by the aerosol layer, respectively, ω_o is the single scattering albedo of aerosols, and β is the fraction of scattering by aerosols which goes upwards.

The relative error on F, $\Delta F/F$, due to error on AOD, ΔAOD, can be estimated from Eq. (11) as:

$$\Delta F/F \approx (1/G)(\partial G/\partial AOD)\Delta AOD \tag{15}$$

Figure 4 displays $\Delta F/F$ as a function of AOD for $\mu_0 = 0.8$, $\beta = 0.3$, $A_s = 0.1$, $\Delta AOD = 0.03$, and three values of ω_o, from 1 (non-absorbing aerosol) to 0.6 (absorbing aerosol). Also

in Fig. 4 we show the ratio of $\Delta G/(G+A_s)$, which is effectively the error in reflectance/(total reflectance), as a function of AOD and $\omega_{o.}$ At small AOD (0.1) $\Delta F/F$ is practically equal to $\Delta AOD/AOD$. $\Delta F/F$ is only weakly dependent on ω_o. If one looks at $\Delta G/(G+ A_s)$ (the error in surface +aerosol reflectance), because the aerosol adds little at low AOD, the error in the combined surface/aerosol reflectance is less than 6% in all cases.

3.2 Specific Regional Analysis

Bates et al. [this issue] separated the aerosol regions sampled on this cruise into 7 areas based on surface chemical and optical data and meteorological data. These regions are shown in Figures 1 and 2 as Regions 2-7. The AOD and angstrom exponents with their associated standard deviations are detailed in Table 2. In Region 1 there were very few AOD measurements because of clouds and rain. The other Regions will now be discussed.

3.2.1 Region 2: North Atlantic Marine airmass (31° N – 15.5° N)

In this Region the calculated 6 day back trajectories [Bates et al, this issue] were mostly over the open ocean. This area was characterized by a very clean atmosphere (AOD = 0.09 $\pm$0.02). The angstrom exponent was also low (0.27$\pm$0.27) indicating a dominance by large particles. While the AOD measured by all instruments were fairly consistent, the angstrom exponent had large variation. To some extent this is because at low AOD, the angstrom exponent is difficult to determine and very dependent on the accuracy of the individual instruments absolute calibration.

3.2.2 Region 3, African dust air mass (15.5° N – 8° N)

In this Region the chemical signature of the surface aerosols and the back trajectories indicated that the major source of the aerosols was Northwest African dust. Aerosol optical depth increased, with a lot of variability in the AOD. Average AOD was 0.29 ($\pm$ 0.05). The angstrom exponent remained low (0.36 $\pm$ 0.13), as seen previously in dust aerosols [Welton, 1998: Smirnov et al., 1998]. The variability in the angstrom exponent between instruments was much lower with the increased AOD, indicating that much of the earlier variability was probably caused by small calibration errors in the individual instruments *Eo*.

3.2.3 Region 4, Mixed African dust and biomass burning (8° N – 3° N)

This Region was the beginning of the ITCZ. In this region we experienced almost continuous boundary layer clouds, thus there were virtually no AOD measurements in this region.

3.2.4 Region 5, Biomass burning in the ITCZ (3° N – 5° S)

This Region had the largest values and range of AOD. The AOD was 0.36 $\pm$ 0.13. Figure 1 shows the large excursions in the AOD experienced in this region. The angstrom exponent was much larger (0.88 $\pm$ 0.30) indicating a dominance by small particles. The calculated back trajectories indicated that the source of the aerosol was burning regions in southwestern North Africa [Bates et al., this issue]. After a peak at the equator, the AOD slowly decreased as we moved south.

3.2.5 Region 6, South Atlantic Tropical Marine airmass (5°S – 24.5°S)

In this Region the surface concentrations of ozone and CO reached clean Southern Hemisphere levels [Thompson et al. 2000]. However the column averaged measurement of the AOD indicated that there was still an elevated signature of aerosols. The presence of upper layer aerosols was confirmed in the LIDAR profile data [Voss et al., this issue]. The average AOD in this region was low (0.10 $\pm$ 0.03), however there was definite structure to the AOD with change in latitude. The angstrom exponent decreased from its high in region 5 to 0.45 $\pm$0.20, however it had not decreased all the way to the values seen in the Northern hemisphere marine airmass of region 2.

3.2.6 Region 7, South Atlantic temperate marine air mass (24.5°S – 33°S)

At this point the airmass trajectories indicated that the aerosols were dominantly coming over the South Atlantic. Average AOD values were similar to the Northern Hemisphere clean values (region 2) (0.10 $\pm$0.01), with angstrom exponents also similar to Region 2 (0.35 $\pm$ 0.07).

4.0 Conclusion

This cruise afforded the opportunity to sample a variety of aerosol regions with an extensive set of chemical, physical, and optical instrumentation. The AOD and angstrom exponent measured with the variety of instruments and techniques agreed fairly well and afforded an opportunity to compare the various techniques. The handheld sunphotometers and the FFRSR allowed the AOD and angstrom exponent to be measured during completely cloudfree periods. The FFRSR, with the automatic sampling, could measure the AOD during any daytime cloudfree period, but then depended on post-

processing to select valid measurements. The operators of the handheld instruments could select cloudfree periods to measure, but obviously would not make measurements continuously throughout the day. The LIDAR could obtain boundary layer AOD during the night and in periods of high cirrus, however since it was only at one wavelength it could not provide any measure of the angstrom exponent. However the extinction/backscattering parameter, derived from the LIDAR inversion is related to the size distribution, see Voss et al., [this issue]). Each instrument has it's own advantages and disadvantages and the combination of the techniques allows a more complete data set to be obtained.

5. Acknowledgements

We thank the officers and crew of the NOAA Research Vessel Ron Brown. We would like to acknowledge the support of NASA under contract #NAS5-31363 (KJV and EW), NAS5-97135 (RF) and SIMBIOS # 52-210.91 (MM and RJR). Part of this work (PKQ) was funded by the Aerosol Program of the NOAA Climate and Global Change Program.

6. Reference

Angstrom, A., The parameters of atmosphere turbidity, *Tellus*, 16, 64 – 75, 1964.

Bates, T. S., P. K. Quinn, D. J. Coffman, J. E. Johnson, T. L. Miller, D. S. Covert, A. Wiedensohler, S. Leinert, A. Nowak, and C. Neus, Regional Physical and Chemical properties of the Marine Boundary Layer Aerosol across the Atlantic during Aerosols99: An overview, submitted to *J. Geophysical Researc*h, this issue.

Harrison, L., J. Michalsky, and J. Berndt, Automated multi-filter rotating shadow-band radiometer: an instrument for optical depth and radiation measurements, *Applied Optics*, 33, 5126—5132, 1994.

Iacobellis, S. F., R. Frouin, and R. C. J. Somerville, 1999: Direct radiative forcing by biomass-burning aerosols: impact of correlations between controlling variables. *J. Geophys. Res*., 104, 12,031-12,045.

Kasten, F. and A. T. Young, Revised optical air mass tables and approximation formula, *Applied Optics*, 28, 4735 – 4738, 1989.

Mueller J., C. McClain, R. Caffrey, and G. Feldman, The NASA SIMBIOS Program, *Backscatter*, May, 29 – 32, 1998.

Penndorf, R. , Tables of refractive index for standard air and the Rayleigh scattering coefficient for the spectral region between 0.2 and 20 um and their application to atmospheric optics, *J. Opt. Soc. America*, 47, 176 - 182, 1957.

Quinn, P. K., D. J. Coffman, T. S. Bates, T. L. Miller, J. E. Johnson, K. J. Voss, E. J. Welton, C. Neususs, Dominant Aerosol Chemical Components and their contribution to extinction during the Aerosols99 Cruise across the Atlantic, submitted to *J. Geophys. Res*., this issue.

Reynolds, R. M., M. A. Miller, and M. J. Bartholomew, Design, Operation, and Calibration of a Shipboard Fast-Rotating Shadow-band Spectral Radiometer, *Jour. Atmos. Oceanic. Technology* (accepted), 2000.

Schwindling, M., P.-Y. Deschamps, and R. Frouin, Verification of aerosol models for satellite ocean color remote sensing. *J. Geophys. Res*., 103, 24,919-24,935, 1998.

Shaw, G. E., Atmospheric Ozone: Determination by Chappuis Band Absorption, *J. Appl. Met.*, 18, 1335 – 1339, 1979.

Shaw, G. E., Sun Photometry, *Bull. Am. Met. Soc*., 64, 4-9, 1983.

Smirnov, A., Holben, B. N., Slutsker, I., Welton, E. J. and Formenti, P., Optical properties of Saharan dust during ACE-2, *J. Geophys. Res.* 103, 28079 – 28092, 1998.

Spinhirne, J. D., Rall, J., and V. S. Scott, Compact eye-safe LIDAR systems, *Rev. Laser Eng*., 23, 26 – 32, 1995.

Spinhirne, J. D., J. A. Reagan, and B.M. Herman, Vertical Distribution of Aerosol Extinction Cross Section and Inference of Aerosol Imaginary Index in the Troposphere by LIDAR Technique, *J. Appl. Meteorol*., 19, 426-438, 1980.

Thompson, A. M., B. G. Doddridge, J. C. Witte, R. D. Hudson, W. T. Luke, J. E. Johnson, B. J. Johnson, S. J. Oltmans, R. Weller, Shipboard and Satellite views of a tropical Atlantic tropospheric ozone maximum and wave-one in January-February 1999, *Geophysical Res. Letters*, submitted 2000.

Voss, K. J., E. J. Welton, J. Johnson, A. Thompson, P. Quinn, and H. Gordon, LIDAR measurements during Aerosols99. Submitted, *J. Geophys. Res.* this issue.

Welton, E. J. Measurements of Aerosol Optical Properties over the Ocean using Sunphotometry and LIDAR, Ph. D. Dissertation. University of Miami, Coral Gables, 1-150, 1998.

Welton, E. J., J. R. Campbell, J. D. Spinhirne, and V. S. Scott, Aerosol and Cloud measurements using micropulse LIDAR systems, *J. Atmos. Oceanic Tech*. Submitted, 2000.

Figure Captions

Figure 1) Aerosol optical depth at approximately 500nm for each instrument and the average values. Error bars are displayed on the average values, derived from the standard deviation between the average and the measurements. Regions 2-7 are displayed on graph as discussed in section 3.2.

Figure 2) The variation in angstrom exponent throughout the cruise. Regions are displayed as in Figure 1. Average angstrom exponent and standard deviation between this average and the data are displayed.

Figure 3) Comparison between instruments for three days, DOY 25, 30, and 37. Each instruments average measurement for the period is displayed, along with the standard deviation. The line in each segment is the average of all the instruments for that day.

Figure 4) Error in calculated forcing with $\Delta AOD = 0.03$ vs. AOD. Also displayed is the fractional error in the total (surface +aerosol) reflectance due to this 0.03 error in AOD. In the calculation $\mu_0 = 0.8$, $\beta = 0.3$, and $A_s = 0.1$.

Table 1) AOD(500nm) and angstrom exponent

DOY	Latitude	AOD	std	angstrom	std
18	29.27	0.08	0.01		
18.5	27.84	0.08	0.06	0.65	0.02
19	26.43	0.08	0.01		
19.5	25.05	0.08	0.01	0.32	0.17
20	23.68	0.08	0.03		
20.5	22.32	0.09	0.02	0.06	0.15
21	20.96	0.09	0.02		
21.5	19.61	0.10	0.02	0.21	0.29
22	18.25	0.10	0.02		
22.5	16.89	0.10	0.50	-0.25	0.17
23	15.52	0.15	0.02		
23.5	14.13	0.28	0.08	0.38	0.15
24	12.73	0.31	0.02		
24.5	11.31	0.28	0.05	0.18	0.11
25	09.87	0.32	0.03		
25.5	08.42	0.32	0.04	0.49	0.11
26	06.94				
26.5	05.44				
27	03.91				

27.5	2.37	0.42	0.03	1.21	0.12
28	0.80	0.37	0.04		
28.5					
29	-02.38	0.41	0.04		
29.5	-04.01	0.22	0.02	0.74	0.12
30	-05.64	0.17	0.02		
30.5	-07.28	0.13	0.02	0.70	0.31
31	-08.94	0.10	0.01		
31.5	-10.60	0.08	0.02		
32	-12.26	0.07	0.02		
32.5	-13.92	0.09	0.02		
33	-15.57	0.15	0.02		
33.5	-17.21	0.10	0.01		
34	-18.83	0.07	0.02		
34.5	-20.42	0.07	0.05	0.46	0.28
35	-21.99	0.08	0.02		
35.5	-23.52	0.11	0.02	0.32	0.20
36	-25.01	0.11	0.03		
36.5	-26.44	0.10	0.03		
37	-27.82	0.10	0.03		
37.5	-29.13	0.10	0.02	0.44	0.13
38	-30.37	0.09	0.02		
38.5	-31.52	0.07	0.02	0.28	0.08

Table 2 AOD and Angstrom exponent broken down by region

Region	AOD	std	Angstrom exponent	std
2	0.09	0.02	0.27	0.28
3	0.29	0.05	0.36	0.13
4	0.41	0.16	0.52	
5	0.36	0.13	0.88	0.30
6	0.10	0.03	0.45	0.20
7	0.10	0.01	0.35	0.07

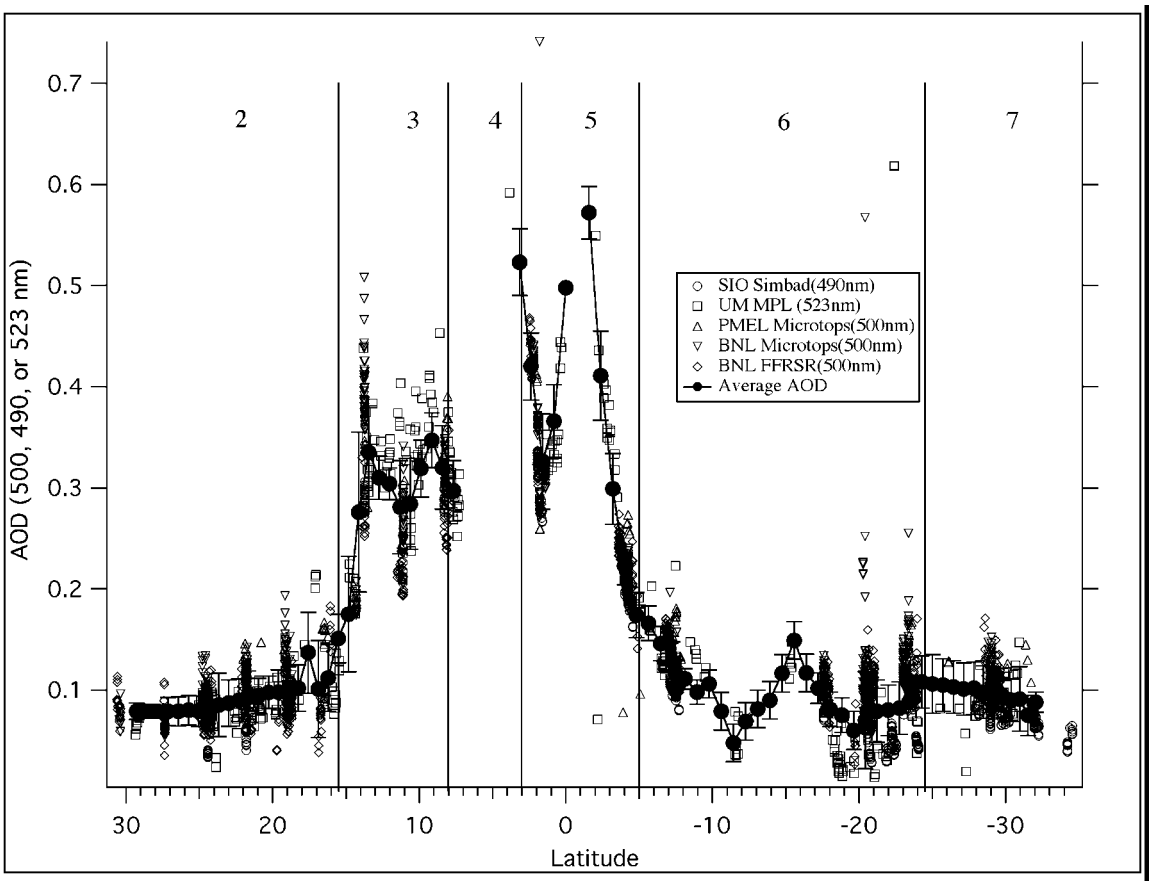

Figure 1) Aerosol optical depth at approximately 500nm for each instrument and the average values. Error bars are displayed on the average values, derived from the standard deviation between the average and the measurements. Regions 2-7 are displayed on graph as discussed in section 3.2.

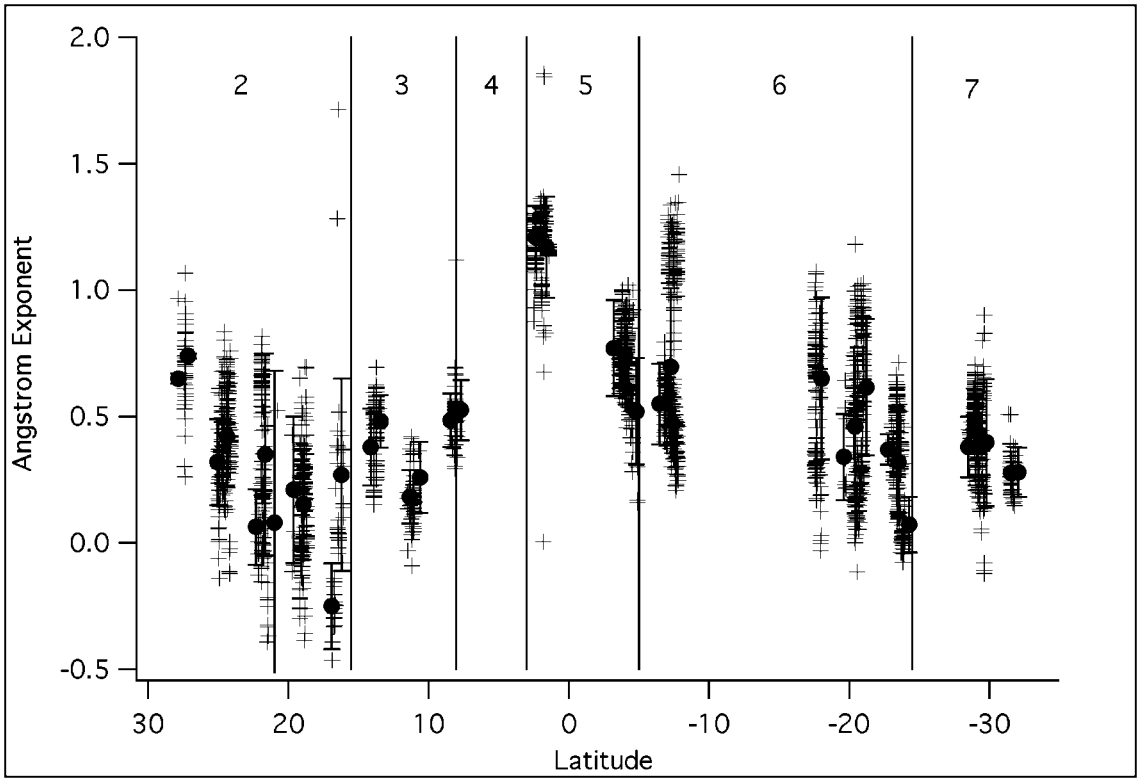

Figure 2) The variation in angstrom exponent throughout the cruise. Regions are displayed as in Figure 1. Average angstrom exponent and standard deviation between this average and the data are displayed.

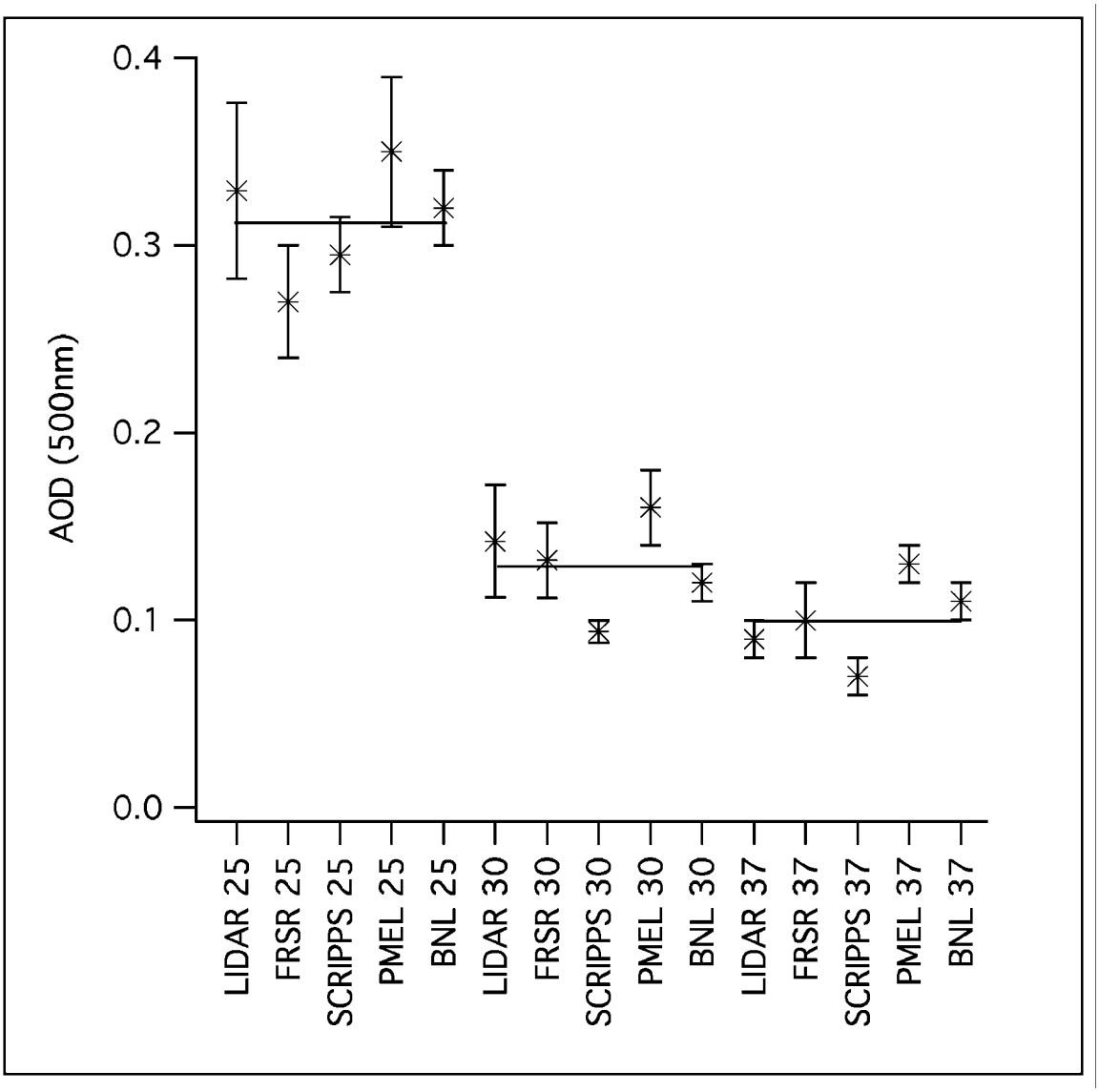

Figure 3) Comparison between instruments for three days, DOY 25, 30, and 37. Each instruments average measurement for the period is displayed, along with the standard deviation. The line in each segment is the average of all the instruments for that day.

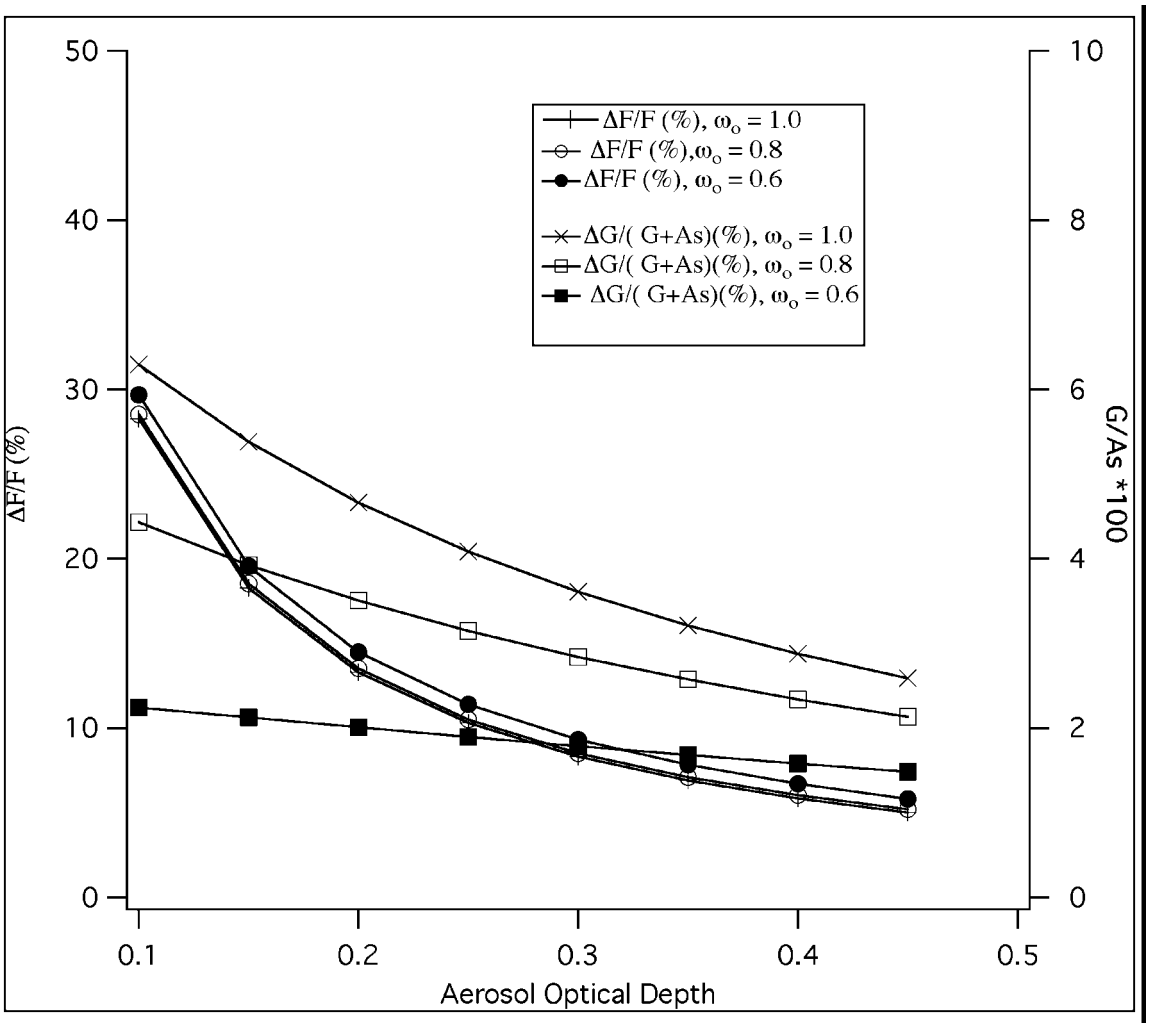

Figure 4) Error in calculated forcing with ΔAOD = 0.03 vs. AOD. Also displayed is the fractional error in the total (surface +aerosol) reflectance due to this 0.03 error in AOD. In the calculation $\mu_0 = 0.8$, $\beta = 0.3$, and $A_s = 0.1$.

Appendix VI

Lidar Measurements During Aerosols99

(Submitted to *Journal of Geophysical Research*)

LIDAR measurements during Aerosols99

Kenneth J. Voss[(1)], Ellsworth J. Welton[(2)], Patricia K. Quinn[(3,4)], James Johnson[(3,4)], Anne Thompson[(5)], and Howard R. Gordon[(1)]

(1) Department of Physics, University of Miami, Miami, Fl.

(2) SSAI, NASA-GSFC, Code 912, Greenbelt, Md.

(3) Pacific Marine Environmental Laboratory, NOAA, Seattle, Wa.

(4) Joint Institute for the Study of Atmosphere and Ocean, University of Washington, Seattle,Wa.

(5) Atmospheric Chemistry and Dynamics Branch, NASA/Goddard Space Flight Center, Greenbelt, Md.

Running title: LIDAR during Aerosols99

*Corresponding author email address: voss@physics.miami.edu

GAP index numbers: 0305, 0649, 0315, 3360, 9325

Submitted J. Geophysical Res., 6/29/00, Aerosols99 Special Section

Abstract

The Aerosols99 cruise took place during the period from January 14, to February 8 1999 on the R/V Ron Brown. The cruise track was almost a straight line from Norfolk, Va. to Cape Town, South Africa and afforded the opportunity to sample several different aerosol regimes over the North and South Atlantic. A Micro Pulse LIDAR system was used continually during this cruise to profile the aerosol vertical structure. Inversions of this data illustrated a varying vertical structure depending on the dominant air mass. In clean maritime aerosols in the Northern and Southern Hemispheres the aerosols were capped at 1 km. When a Dust event from Africa was encountered the aerosol extinction increased its maximum height to above 2 km. During a period in which the air mass was dominated by biomass burning from Southern Africa, the aerosol layer extended to 4 km. Comparisons of the aerosol optical depth derived from LIDAR inversion and surface sunphotometers showed an agreement within $\pm$0.05 RMS. Similar comparisons between the extinction measured with a nephelometer and particle soot absorption photometer (at 19 m altitude) and the lowest LIDAR measurement (75 m) showed good agreement ($\pm$0.014 km^{-1}). The LIDAR underestimated surface extinction during periods when an elevated aerosol layer was present over a relatively clean surface layer, but otherwise gave accurate results.

1. Introduction

The Aerosols99 cruise took place during the period from January 14, to February 8 1999 on the R/V Ron Brown. The cruise track was almost a straight line from Norfolk, Va. to Cape Town, South Africa and afforded the opportunity to sample several different aerosol regimes over the North and South Atlantic. A multidisciplinary group participated on this cruise allowing for the measurement of an extensive suite of chemical, physical, and optical properties of the surface aerosol [Bates et al. this issue]. Along with these surface measurements a Micropulse LIDAR system [SESI, Burtonsville, MD] [Spinhirne et al., 1995] was operated continually to provide vertical profile information on the aerosol distribution. Ozonesondes and Radiosondes provided profiles of the temperature, humidity, and ozone distribution, which gave additional information on the structure of the atmosphere. Finally 5-day meteorological back trajectories provided information on the sources of the sampled aerosols. All of this information, when combined, gives a more complete picture of the aerosol structure over the Atlantic.

The cruise track presented a chance to look at many of the aerosol regimes over the Atlantic. This cruise track was impacted by aerosols from the North American continent, by Saharan Dust, by biomass burning on the African continent, and by clean maritime air in the regions between. There is very little information on the vertical distribution of the aerosols over the ocean, yet the vertical distribution of these aerosols can impact the accuracy of climate models and atmospheric corrections needed for retrieving ocean color. The Saharan Dust and biomass burning aerosols typically absorb

light. While atmospheric correction of ocean color imaging can be done for non-absorbing aerosols without knowledge of the aerosol vertical structure [Gordon, 1997)] the optical effect of absorbing aerosols is very dependent on the vertical structure [Gordon et al., 1997]. Aerosol models for atmospheric correction of ocean color imagery must account for this vertical structure when dealing with absorbing aerosols, yet there is little data available on this problem. This cruise offered an excellent opportunity to measure the aerosol vertical structure and have an extensive set of correlated measurements of the boundary layer aerosol.

In addition to atmospheric correction, it is important to have information on the vertical structure to understand how the surface measurements of the aerosol properties are related to the aerosols in the rest of the atmospheric column. A LIDAR gives direct information on the vertical distribution of aerosols. At times the surface measurements can be very different from the column above [Welton et al., 2000]. The LIDAR provides additional information that can be used to extend the surface measurements or show the presence of other layers above the surface.

During this cruise a micro pulse LIDAR [Spinhirne et al., 1995] was used to provide the vertical structure information. This LIDAR is a very compact system and was operated continuously during the cruise. With careful calibration and data reduction, accurate information on the aerosol vertical structure of the atmosphere can be obtained. This cruise allowed us to look at the relationship between the vertical structure of the aerosols, relative humidity (RH), temperature, surface physical and chemical aerosol properties, and back trajectories.

2 Methods

2.1 LIDAR

The Micropulse LIDAR [SESI, Burtonsville, MD] is a small compact LIDAR system which averages high repetition, low energy pulses to obtain a profile of attenuation/backscattering in the atmosphere [Spinhirne et al.,1995]. The Micropulse LIDAR used during the cruise operated at 523 nm, with a pulse repetition rate of 2500 Hz, the vertical resolution was 75m, and data was collected to 30 km. During the day the signal above 10 km became increasingly noisy due to a combination of attenuation in the boundary layer and background sunlight at 523 nm, but during the night low noise data could be obtained to 20 km in the absence of clouds. The details of the algorithm to retrieve the AOD and vertical profile of extinction or backscattering from the Micropulse LIDAR are detailed elsewhere [Welton, 1998, Welton et al., 2000b], however an overview of the technique will be presented here.

The basic equation governing LIDAR propagation, when the LIDAR is vertically oriented is:

$$Er(t) = CEo(\beta_r(180,z) + \beta_a(180,z))\exp(-2 * \int_0^z [c_r(z') + c_a(z')]dz') / z^2 \quad (1)$$

Where *Er* is the received energy, *Eo* is the outgoing pulse energy, $\beta_r(180,z)$ is the Rayleigh (molecular) backscattering, $\beta_a(180,z)$ is the aerosol backscattering, c_r is the Rayleigh attenuation, c_a is the aerosol attenuation, and *C* is an instrument calibration

constant. The time the signal is received is related to the altitude, *z*, by the time it takes for the LIDAR pulse to travel up to that altitude and back ($z = tc/2$, where c is the speed of light). By using time resolved return signals, profiles of the backscattering and attenuation can be obtained. *C* contains information on system parameters such as throughput, solid angle acceptance of the receiver, divergence of the laser beam and other parameters. While in principal this could be calculated [Spinhirne et al., 1980], in practice it is much simpler and more accurate to derive this parameter from measurements in the field, as will be discussed below. For a practical LIDAR system such as the MPL, there are other important effects which must be taken into account, namely the overlap and afterpulse functions. The overlap function describes the loss in signal strength at close range. Signal loss is due to optical design and to poor focusing to the detector by the MPL telescope at close range (less than 4 km). Signals at ranges greater than the overlap range are not effected by this problem. The afterpulse function is a result of cross-talk between the laser pulse and detector, as well as dark noise in the system. Both of these effects were corrected for in this data set in the manner described by Welton et al.[2000b].

When the AOD is known from independent measurements (such as with a handheld sunphotometer) the system calibration constant *C* can be determined [Welton et al., 2000b]. During cloud free periods during the cruise, episodic measurements of the AOD were made with a Microtops sunphotometer (Solar Light Co., Philadelphia, PA). For the LIDAR profile corresponding to the AOD measurement, a clean aerosol free layer above the boundary layer is found (for this cruise this was typically 6-7 km). This is usually obvious from the range corrected LIDAR signal by looking for a region for which

ln[$Er(t)*z^2$] is decaying at the rate appropriate for Rayleigh scattering. The returned energy from that altitude is simply:

$$Er(t) = CEo\beta_r(180, z)\exp(-2 * \int_0^z [c_r(z') + c_a(z')]dz') / z^2 \quad (2)$$

Or

$$C = Er(t)z^2[Eo\beta_r(180, z)\exp(-2 * AOD)\exp(-2 * \int_0^z c_r(z')dz')]^{-1} \quad (3)$$

All of the factors on the right hand side of Eq. 3 are measured (AOD) or calculated, thus C can be determined. The calibration coefficient was fit to a linear equation and decreased linearly during the cruise by 20%.

Once the LIDAR calibration coefficient is determined, for each period a clean aerosol free layer above the boundary layer is found. With the calibration coefficient and this clean layer, the returned energy is given by Eq. 2 above, and Eq. 3 can be rewritten to obtain the AOD. It is important to note that this product does not depend on any assumption of the extinction/backscatter ratio. The accuracy of our calibration procedure is estimated to be $\pm$3%. The accuracy of the AOD calculation is affected by this calibration coefficient, and the accuracy with which the overlap and afterpulse corrections were made. The accuracy of the AOD determined from the LIDAR is estimated to be $\pm$0.02 in optical depth, but this error can increase due to other factors such as system noise.

With the AOD determined, an inversion must be made of the LIDAR return signal to obtain the extinction or backscattering profile. Since the LIDAR return depends on both the backscattering and extinction of the aerosols and molecules this leads to 4 variables to find from one input. The molecular (Rayleigh) backscatter and extinction coefficients can be calculated, reducing the unknowns. To reduce the number of free variables an assumption is made about the ratio between the extinction and backscatter coefficient, otherwise known as *S* (units are sr). We use a top-down inversion with a constant *S* for aerosols [Fernald et al., 1972, Fernald, 1984, Welton et al., 2000b], our exact method is described in detail in Welton [1998] and Welton et al.[2000b]. In this method the LIDAR equation is re-written in the form:

$$Er(t) = CEo(\beta_r(180,z) + c_a(z)/S_a)\exp(-2*\int_0^z [c_r(z') + c_a(z')]dz')/z^2 \quad (4)$$

Where S_a is *S* for aerosols. An inversion of the LIDAR return signal is performed, with an initial guess for S_a, to determine the profile of $c_a(z)$. This profile is then integrated and compared with the AOD obtained from Eq.. 3. S_a is adjusted with this result, and the procedure is iterated. This process is continued until the AOD and the integrated profile of $c_a(z)$ agree within 0.5%. Since S_a is assumed to be constant, $\beta_a(180,z)$ is just $c_a(z)/S_a$.

The final accuracy of this inversion depends on the assumption of a constant S_a through the aerosol layer. With additional information this constraint could be removed, but without this errors are introduced. Even without changes in aerosol composition, changes in RH can effect S_a by changing the size distribution and index of refraction of

the aerosols [Ackermann, 1998]. The radiosonde data (discussed below) indicated that the variation in RH through the aerosol layer changed between the different regions along the cruise track(defined below). The constant S_a that is determined from the LIDAR inversion is a column averaged S_a. The errors introduced by this assumption will be discussed in more detail in the discussions of the individual regions and a comparison with the surface extinction measured with a nephelometer and a PSAP.

2.2 Radiosonde

Radiosondes, [Vaisala, RS80-15GH] were launched from the deck of the ship at 10:45 and 22:45 UTC each day. This launch time ensured that each radiosonde would be in the middle of its profile during the synoptic times of 0000 and 1200 UTC. The radiosondes measured vertical profiles of temperature, relative humidity, and horizontal winds. The winds were calculated from GPS measurements of the sonde horizontal position. Most radiosonde profiles extended to at least 15 km altitude. The sondes transmitted one data point every 10 seconds so that the raw data from the sondes (used here) had a vertical resolution of 20 to 40 meters.

To help define the variation of temperature with altitude, the rate of change of the temperature with altitude, $\Delta T/\Delta z$, was derived from the temperature data. $\Delta T/\Delta z$ (°C/km) was calculated by using a sliding five point least-squares-fit to the temperature data ($\pm$ 2 points around the specific altitude). This altitude interval is approximately 100-200 m.

2.3 Back-trajectories

Five day back-trajectories were made using the isentropic trajectory model at Goddard Space Flight Center/NASA [Schoeberl et al., 1992]. These trajectories were

initialized from the position of the ozonesonde launches along the cruise track. Clusters of back-trajectories were run from each launch to capture the uncertainties associated with analyzed winds (Numerical Center for Environmental Prediction (NCEP) 2.5 X 2.5 deg).

3 Results

The first discussion will compare LIDAR-derived AOD and extinction to AOD and extinction derived from independent measurements. We will then look at the overall LIDAR cruise data and investigate the results of the LIDAR and other vertical profile information for specific cruise regions.

3.1 AOD comparison

Voss et al. [this issue] shows the complete data set of AOD measurements obtained during the cruise, including the LIDAR measurements. This data set included a set of 3 Microtops Sunphotometers [Solar Light Co., Philadelphia, PA] independent of the one used to calibrate the LIDAR. To investigate the agreement between the LIDAR derived AOD and the sunphotometer AOD we grouped the LIDAR data and Sunphotometer data into common 72-minute measurement periods. In Fig. 1 the comparison between the two data sets are shown for all periods which have measurements with both techniques. The error bars for the sunphotometer measurement is the standard deviation of the distribution of sunphotometer measurements during the specific interval. The LIDAR error bars are due to the uncertainty in the LIDAR calibration constant, and signal noise (including afterpulse and overlap noise). The line in the figure is the 1:1 line. The agreement between the two methods is good, the RMS difference is 0.05 (optical depth). For larger

AOD the LIDAR AOD appears slightly higher than the sunphotometer AOD. The difference could be due to the LIDAR technique, to different measurement volumes (the LIDAR is vertical, the sunphotometer measures along the solar path), or differences in the specific measurement time in the 72 minute period. In general though the LIDAR derived AOD agrees with the standard sunphotometer technique to within the stated errors.

3.2 Surface extinction comparison

We did not have simultaneous measurements of the vertical extinction profile from an independent source (such as an aircraft) during this cruise, however we have done this in the past and compared this data with the LIDAR inversion with good results (Welton et al., 2000). During this cruise we had surface scattering and absorption measurements [Quinn et al., this issue] with which to compare the lowest altitude bin of the LIDAR. The aerosol was sampled at 19 m altitude with an integrating nephelometer (TSI Model 3563) and a particle soot absorption photometer (PSAP, Radiance Research). The scattering coefficient (measured at 55% RH and 550nm) was adjusted to ambient RH using the RH measured on the ship and previously measured f(RH) relationships. For the marine air mass regions, f(RH) for the light scattering coefficient was based on measurements during onshore flow at Cape Grim, Tasmania [Carrico et al., 1998]. In continentally-influenced regions f(RH) from continental air masses at Sable Island, Nova Scotia [McInnes et al., 1998] was used. For the light absorption coefficient (measured at 55% RH and 565 nm), f(RH) was assumed to equal one.

These surface extinction measurements were compared with the extinction retrieved from the LIDAR inversion at the lowest altitude bin (75 m). The comparison through the cruise is shown in Fig. 2. The agreement is generally very good, but there are specific regions for which the agreement is not as good. Figure 3 shows the comparison of the two measurements more quantitatively. The RMS difference between the two measurements was 0.014 km^{-1}. In this figure the measurements are broken into regions as defined later in the text (section 3.4). The most pronounced bias between the two measurements occurs during portions of Region 5 and at the beginning of Region 6 (to approximately 13° S). The extreme of this is near 5°-10° S when the surface values of the LIDAR are set to zero. During this period we had an elevated aerosol above a clean marine boundary layer (MBL) (MBL properties were determined from the surface chemistry measurements [Quinn et al., this issue]). In the portions of Region 5 (the lower surface extinction areas) and in Region 6a, the total column AOD did not decrease as much as the surface extinction did. When there is an elevated aerosol layer above a clean (or relatively clean) lower layer, the lidar inversion underestimates the extinction in the lower layer. It could also be that this difference is simply due to the different sampling altitudes and this effect is most important in this region. In general the LIDAR inversion worked well even in the near field, which has the most difficulties due to calibration difficulties. However, this analysis shows a case where the surface LIDAR data may be suspect because of the presence of an elevated aerosol layer over the relatively clean surface layer

3.3 LIDAR data through cruise

Figure 4 shows the contour plot of the extinction profile during the cruise. The contour plot is built from the LIDAR data, with 75m vertical resolution and at the data points marked at the bottom of the graph. Gaps in data were predominately due to clouds; however, during periods of high sun angle (solar noon) the LIDAR was turned off to avoid direct sunlight entering the detector (this also had to take into account possible ship roll, as direct sunlight would cause a complete failure of the system). Also delineated in the figure is the division into regions, discussed in detail below. As can be seen there was a large variation in both vertical structure and magnitude of the extinction, which was dependent on both location and recent meteorological transport.

While the aerosol obviously reached higher levels near the equator, it is also interesting to see how the aerosol is distributed, proportionately, for a given profile. Figure 5 shows a contour of the integrated extinction coefficient. This was calculated as:

$$IntegratedExtinction(z) = \frac{\int_{0}^{z} c_a(z')dz'}{\int_{0}^{6km} c_a(z')dz'} * 100 \qquad (5)$$

Once again the data points on which the contours were produced are shown at the bottom of the graph. Before 8 N and after 15 S, 25% and 50% lines (the altitude at which 25 and 50% of the AOD has been accounted for already) are fairly constant at 0.5 km and 0.8 km. The 75% and 90% lines, during this time, show periods for which more aerosol (relative to the rest of the column) was added at 1-1.5km (approximately 14 N and 20S). Between 8 N and 15S the surface layer is cleaner than the elevated layers. Thus all the contours rise during this period. In particular at the beginning of region 6 the 90% level

was the highest of the cruise. At this time there was a very clean lower level, and an elevated aerosol. While the optical depth [Voss et al, this issue] and extinction (Figure 4) were not maximum here, the clean lower level had the effect of making the upper aerosols a more important contribution to the column properties.

Figure 6 shows S_a derived from the LIDAR inversions through the cruise, also shown are the error bars on this derived parameter [method described in Welton et al., 2000b]. These will also be discussed in the specific regional discussions below, but the main feature is that during the periods of low total column extinction and low AOD, in regions 2 and late 6, S_a tended to have low values characteristic of maritime aerosols. During the periods of high AOD and high total column extinction, S_a was higher, typical of smaller particles and continental aerosols.

3.4 Specific regional vertical structure features

We will now discuss the differences in vertical structure of the lower atmosphere (<7 km) defined for the different regions. These regions were defined by surface trace gas concentrations, aerosol chemical and physical properties, and trajectories at the 500 m arrival height, [Bates et al., this issue], and may be somewhat different than those defined by other information with vertical profiles such as LIDAR or ozonesondes [Thompson et al. 2000]. The five day back-trajectories are shown in Fig. 7 and 8. The trajectories shown correspond to the weighted central point in each cluster at 1km and 4km levels. Time of trajectory initiation is 12Z with crosses marking every 24hr. For each region a typical radiosonde/LIDAR profile is shown. In each case the figure shows the radiosonde data (RH and $\Delta T/\Delta z$) along with the average of three LIDAR extinction coefficient

profiles obtained within 1 hour of the radiosonde profile. Because of intense clouds there are no LIDAR data for Region 1, so we begin our discussion with Region 2.

3.4.1 Region 2: Northern Hemisphere clean (31° N – 15.5° N)

In this region back trajectories at 1km and 4 km indicated that the airmass origin was over the North Atlantic (Figs. 7 and 8). Surface measurements of the aerosol chemistry indicated that the aerosol was clean maritime aerosol [Bates et al., this issue]. Example radiosonde and LIDAR profiles from this region (for DOY 18.5, N 27.7°) are shown in Figure 9.

In the example shown there is a strong temperature inversion at 1 km, and another at 2 and 4.5 km. The RH, in this example, stayed relatively constant at 80±10% up to 3 km. The aerosol was capped by the 1 km inversion, as witnessed by the LIDAR extinction coefficient. In general the extinction coefficient was low throughout this region (less than 0.2 km^{-1} peak), and the peak extinction coefficient was below 1 km, with very little extinction above 1 km (this example had the largest extinction above 1 km). The extinction profiles indicated that 90% of the AOD occurred below 2-3 km. The temperature structure seemed to vary, with strong inversions often occurring between 1-1.5 km. These temperature inversions were typically associated with the top of the aerosol layer. Relative humidity was generally above 80% throughout the aerosol layer.

Since the surface chemistry and back trajectories all indicated that this was a maritime atmosphere, there is no indications that there were drastic changes in aerosol composition in the aerosol layer. With the RH limited between 80 and 100%, Ackermann's model [Ackermann, 1998] for S_a for a maritime atmosphere, indicates that

the value should be approximately 25, with RH effects only indicating a range from 23-27. Thus our assumption of a constant S_a is a reasonable approximation in this region. We found that the S_a average for this region was 32±6 sr, which is near the values derived above. As discussed elsewhere [Voss et al, this issue] the AOD was low in this region (around 0.09±0.02) with a low angstrom exponent (0.27±0.27). The low angstrom exponent correlated with the low S_a indicating that the aerosol size distribution was weighted towards larger particles.

One final feature in this region was that initially the RH stayed high (>60%) throughout the column below 7 km. At 25° N the structure changed, becoming dryer above 3 km. By 23.7° N the humidity was less than 10% between 3 and 6 km, with some excursions above 10% occurring between 6 and 7 km. Since this was above the aerosol layer, there was no visible effect on the aerosol vertical structure. A more complete picture of the vertical profile of RH through the cruise is shown in Bates et al. [this issue].

3.4.2 Region 3: Dust (15.5° N – 8° N)

During the next portion of the cruise we had a significant dust event that changed the surface and vertical aerosol structure. Back trajectories at 1 km showed the aerosol source switching to the coast of Africa, with 4 km trajectories still coming from the North Atlantic.

A typical example of the vertical structure is shown in Fig. 10 for Day 24.5, N 11.2°. The radiosonde data throughout this period indicated a strong temperature inversion at 1.5 km and another temperature feature at 4-5 km. The RH was relatively

constant at 80-100% in the lower layer, below the 1.5 km temperature inversion. However at this inversion the RH decreased rapidly to 20-40%. The RH stayed constant at this level to the upper temperature feature (4-5 km) where it seemed to decrease to near 0%RH for a 1 km layer, after which it would increase back to 20-40%.

The LIDAR profile data showed two distinct layers, with a sharp minimum in extinction between them. The lower layer was capped by the temperature inversion at 1.5 km. The upper layer peaked at 2 km, with a subsequent gradual decrease with altitude. By 4 km the aerosol extinction was very low (<0.02 km^{-1}). The peak extinction in the lower layer was approximately 0.3 km^{-1}, while the peak extinction in the next layer was approximately 0.1 km^{-1}, so most of the AOD occurred in the lower layer. During this period, 90% of the AOD occurred below 2-3 km.

The column averaged S_a during this period was 41$\pm$8 sr. This is significantly higher than the S_a predicted by Ackermann (1998) for desert aerosols. Ackermann's work assumed spherical particles, however dust particles are often non-spherical which increases S_a by decreasing the backscattering at 180 degrees. This value for S_a agrees with earlier measurements by Welton et al. [2000]. In this region while the RH in each layer was relatively constant, the RH changed significantly between the upper and lower layer (80-100% to 40%). However because desert aerosol responds only weakly to RH, this change effects S_a very weakly (less than 10% change in S_a [Ackermann, 1998]). Thus changes in the S_a due to humidity are not expected. With the upper layer being very distinct, it is possible that a different aerosol was in the upper layer, however we have no in-situ chemical information on this layer to say what the layer might be. We also note that the earlier comparison in Fig. 3 showed no definite bias for this region. Thus the

constant S_a algorithm for the LIDAR inversion is the best we can use with the available information.

3.4.3 Region 4: Mixed Dust and Biomass burning (8° N – 3° N)

This period was characterized by the surface chemistry to be changing from the previous dust event to a biomass-burning aerosol. Back trajectories at 1 and 4 km indicated that the column aerosol was coming from Africa.

Radiosonde data indicated very strong and varying temperature and humidity structure through this period, and it is difficult to pick a representative profile. Figure 11 is an example of the structure during this period, for day 26, N 7.5°. In all of the radiosondes there was a strong temperature inversion near 1 km. At times there were other inversions above this with varying strength. The humidity was typically high (above 80%) below the lower inversion, but in the lower 7 km the RH decreased irregularly to 20-40%.

There was always a large LIDAR derived extinction peak near 1 km, with extinction values on the order of 0.3 km^{-1}. Additionally a peak occurred near 2 km with significant extinction (near 0.2 km^{-1}). The aerosols continued higher, with significant extinction to near 4 km. The 90% level for the AOD extinction was at 2.7 km, somewhat higher than in previous regions. The minimum between the lower and upper peak was not as distinct, or at as low an altitude, in this region as in the previous indicating there may have been more mixing between the layers.

The average S_a in this region increased to 52 $\pm$10 sr, which is between Ackermann's continental and desert aerosols, possibly reflecting the mix of aerosols at this location.

With the large peaks in aerosol extinction the AOD was significantly higher with the average AOD being 0.41. The angstrom exponent was also higher here, reaching 0.52, but because of clouds there were few sunphotometer measurements on which to base this angstrom exponent.

3.4.4 Region 5: Biomass burning (3° N – 5° S)

The next region reached during the cruise had surface aerosol chemistry characteristics of biomass burning. Back trajectories at 1km were mostly over the south Atlantic, however 4 km trajectories were from central Africa and the 8 km trajectories were also from the African coast.

Typical radiosonde and LIDAR data are shown in Fig. 12 and are from DOY 29, S 2.3°. In this region there were typically temperature inversions at 1.5 – 2 km, then other inversions above this (3, 4, 5 km and above). The RH varied between staying above 80% all the way to 4.5 km, to having a minimum of 40% at 2 km. It is difficult to find a general trend.

The aerosol extinction profile also varied over this region. In all cases significant aerosol extinction extended to 4 km. The 90% AOD level in this region averaged 3.3 km. The peak extinction reached >0.20 km^{-1}, with broad (>2 km) peaks. At times the peak moved off of the 1 km level to 2-3 km, but was typically at 1 km. The aerosol also seemed to decrease at 2 km, but then maintained a significant extinction to 4 km.

The S_a during this period was relatively high, 60$\pm$ 6 sr, which is a little lower than the value predicted for continental aerosol at this RH (>80%) by Ackermann[1998]. The average AOD was high, 0.36, with a very high average angstrom exponent of 0.882. This

indicates that the aerosol particles were probably relatively small, which agrees with the high measured S_a.

3.4.5 Region 6: Southern hemisphere clean (5° S – 24.5° S) and Region 7: South Atlantic temperate marine air mass (24.5° S – 33° S)

After going through these intense aerosol events, the surface chemistry again indicated a clean maritime situation [Bates et al., this issue]. Interestingly, while the surface measurements indicated a change at 5° S, the back trajectories did not switch as rapidly. The 1km trajectories were over the south Atlantic, however early in the Region (between 5° S and 12° S) 4 km trajectories were still over southern Africa and only switched to the south Atlantic after 12° S. An example of the earlier period is shown in Fig. 13, while an example of the later period is shown in Figure 14. Figure 13 is for Day 30.5, S 7.4°, while Fig. 14 is for Day 35.5, S 23.6°. We have grouped these two regions together, because the vertical structure of the late part of region 6 was basically the same as that of region 7.

The radiosonde data for the earlier period shows a strong temperature inversion at 1.5 km. The RH is typically very high (>80%) below this inversion, but decreases at the inversion to 50-60%. The aerosol extinction profile shows why the surface chemistry appeared clean, yet column AOD was not small. One can see that the surface extinction is below 0.01 km^{-1}, while the column extinction reaches >0.1 km^{-1} at 1 km or greater. During this early period, significant aerosol extended to 4 km, with the average 90% AOD level at 3.2 km, showing how high the aerosol was in the atmospheric column. The S_a in the early period was 63 $\pm$12 sr, much higher than the values determined for the N.

Hemisphere clean region, and close to the value of the biomass burning. As can be seen in Figure 2 and the discussion above, the algorithm results are more uncertain when an optically dense upper layer is above a clean maritime layer. The algorithm tends to underestimate the extinction in the lower level. In terms of the overall column optics this is not a significant error, however it does underestimate the scattering in this lower level significantly.

By the end of the period the region resembles the Northern Hemisphere clean situation. The radiosondes show a strong inversion at approximately 1.5 km. The RH stays high (80-100%) to this altitude then drops to low values(30-40%) above the inversion. Aerosols are capped at 1 km by the inversion, but only reach extinction of 0.1 km^{-1} or so below the inversion and are at background (<0.01 km^{-1}) above the inversion. The 90%AOD level is at 1.4 km. The S_a also decreases to levels seen in the first region (36$\pm$16 sr). AOD and angstrom exponents are also down to the values in Region 2 (0.094 and 0.35 respectively [Voss et al., this issue]). The structure in these clean northern and southern hemisphere cases is the same.

4. Conclusions

With the LIDAR and associated measurements during this cruise we were able to determine the aerosol vertical structure of the lower portion (<7 km) of the atmosphere. Comparisons of the LIDAR derived AOD and extinction with sunphotometers and a surface nephelometer and PSAP showed that the LIDAR inversions were giving reasonable results throughout the cruise. Specific situations, particularly clean lower layers below elevated aerosol layers, caused the problems with the near field LIDAR

inversions. However for the most part the LIDAR derived AOD and extinction agreed within the expected errors.

The LIDAR parameters showed that during this cruise the vertical distribution of the aerosols varied depending on location and meteorological conditions. LIDAR inversions to obtain the extinction profile illustrated a varying vertical structure depending on the dominant air mass and on the temperature structure of the atmosphere. In the periods of clean maritime aerosols in the Northern and Southern Hemisphere the aerosols were predominantly below 1-2 km. A dust event from Africa increased the maximum height of aerosol extinction to between 2 - 3 km. During a period in which the air mass was dominated by biomass burning from Southern Africa, the aerosol layer extended to 3-4 km. Because many of these aerosols are absorbing, differences in vertical structure will have important impacts on calculations of the radiative forcing by aerosols and on atmospheric correction of ocean color imagery.

5. Acknowledgements

We thank the officers and crew of the NOAA Research Vessel Ron Brown. We would like to acknowledge the support of NASA under contract #NAS5-31363 (KJV, EW, and HRG). Part of this work (PKQ) was funded by the Aerosol Program of the NOAA and the NASA Global Aerosol Climatology Project.

6. References

Ackermann, The extinction-to-backscatter ratio of troposphere aerosol: A numerical study, *J. Atmosph. and Ocean. Techn.*, 15, 1043 – 1050 (1998).

Bates, T.S., P.K. Quinn, D.J. Coffman, J.E. Johnson, T.L. Miller, D.S. Covert, A. Wiedensohler, S. Leinert, A. Nowak, and C. Neususs, Regional physical and chemical properties of the marine boundary layer aerosol across the Atlantic during Aerosols99, *J. Geophys. Res., submitted,* 2000.

Carrico, C.M, M.J. Rood, and J.A. Ogren, Aerosol light scattering properties at Cape Grim, Tasmania, during the first Aerosol Characterization Experiment (ACE 1), *J. Geophys. Res., 103,* 16,565 – 16,574 (1998).

Fernald, F.G., B. M. Herman, and J. A. Reagan, Determination of aerosol height distributions by lidar. *J. Appl. Meteorol.*, **11**, 482-489 (1972).

Fernald, F.G., Analysis of atmospheric lidar observations: some comments. *Appl. Opt.*, **23**, 652-653(1984).

Gordon, H. G., Atmospheric Correction of Ocean Color Imagery in the Earth Observing System Era, *Jour. Geophys. Res.*, **102D**, 17081-17106 (1997).

Gordon, H. G., T. Du, and T. Zhang, Remote sensing ocean color and aerosol properties: resolving the issue of aerosol absorption, *Applied Optics*, **36**, 8670-8684 (1997).

McInnes, L., M Bergin, J. Ogren, and S. Schwartz, Apportionment of light scattering and hygroscopic growth to aerosol composition, *Geophys. Res. Lett.*, 25, 513 516 (1998).

Quinn, P.K., D.J. Coffman, T.S. Bates, T.L. Miller, J.E. Johnson, K. Voss, E.J. Welton, and C. Neususs, Dominant aerosol chemical components and their contribution to extinction during the Aerosols99 cruise across the Atlantic, *J. Geophys. Res., submitted*, 2000.

Schoeberl, M. R., Lait, L.R., Newman, P. A., Rosenfield, J. E., The Structure of the Polar Vortex , *J. Geophys. Res*., 97, 7859-7882 (1992).

Spinhirne, J.D., J.A. Reagan, and B.M. Herman, Vertical Distribution of Aerosol Extinction Cross Section and Inference of Aerosol Imaginary Index in the Troposphere by LIDAR Technique, *J. Appl. Meteorol.*, 19, 426-438 (1980).

Spinhirne, J. D., Rall, J., and V. S. Scott, Compact eye-safe LIDAR systems, *Rev. Laser Eng.*, 23, 26 – 32 (1995).

Welton, E. J. Measurements of Aerosol Optical Properties over the Ocean using Sunphotometry and LIDAR, Ph. D. Dissertation. University of Miami, Coral Gables, 1-150 (1998).

Welton, E. J., K. J. Voss, H. R. Gordon, H Maring, A. Smirnov, B. Holben, B. Schmid, J. M. Livingston, P. B. Russell, P. A. Durkee, P. Formenti, M. O. Andreae, Ground-based LIDAR Measurements of Aerosols During ACE-2: Instrument Description, Results, and Comparisons with other Ground-based and Airborne Measurements, *Tellus*, **52**: 635 – 651 (2000a).

Welton, E. J., J. R. Campbell, J. D. Spinhirne, and V. S. Scott, Aerosol and Cloud measurements using micropulse LIDAR systems, *J. Atmos. Oceanic Tech*. Submitted, (2000b).

7. Figure Captions

Figure 1) LIDAR derived AOD vs Sunphotometer derived AOD for common measurement periods during the cruise. Line is 1:1 fit. LIDAR AOD is at 523nm, sunphotometer AOD ranges from 490 – 500 nm. Error bars on x-axis are from the standard deviation of sunphotometer samples common with LIDAR measurements. Error bars on y-axis are from the estimate of the error of the calibration coefficient, and signal noise (including afterpulse and overlap noise)..

Figure 2) LIDAR derived surface (75m) extinction (displayed as +) and nephelometer surface(19 m) extinction (displayed as the line) throughout the cruise.

Figure 3) LIDAR and Nephelometer extinctions during common measurements periods. Measurements are broken into Regions as discussed in text. Note the definite regional bias (LIDAR low) in Region 5 and 6a. Line is 1:1 line for reference.

Figure 4) Contour plot of LIDAR derived extinction coefficients along the cruise track. Regions as defined by Bates et al. [this issue] are delineated by the lines. The data positions on which the contours are based are shown as lines at the bottom of the graph.

Figure 5) Contour of integrated extinction from the surface to z. Vertical lines delineate regions as defined in Bates et al.[this issue]. The data positions on which the contours are based are shown as lines at the bottom of the graph.

Figure 6) S_a (extinction/backscattering) derived throughout the cruise. Vertical lines delineate regions as defined in Bates et al.[this issue]. S_a was lower in clean maritime airmasses then in those impacted by dust or biomass burning.

Figure 7) 1 km back-trajectories, Regions as discussed in text are shown divided by lines on the graph.

Figure 8) 4 km trajectories, Regions as discussed in text are shown divided by lines on the graph.

Figure 9) Radiosonde and LIDAR derived profiles typical for Region 2, Northern Hemisphere clean (31° N – 15.5° N). This specific case was for DOY 18.5, N 27.7°. LIDAR extinction is shown as the fine line with no symbols. This is an average of the nearest three profiles (each of which is a 10 minute cloudfree average) around the Radiosonde launch. Relative Humidity is displayed as the line marked with filled circles, while $\Delta T/\Delta z$ is displayed as the line marked with filled squares. Note overall extinction is low and capped by the first temperature inversion (positive $\Delta T/\Delta z$).

Figure 10) Radiosonde and LIDAR derived profiles typical for Region 3, Dust (15.5° N – 8° N). This specific case was for DOY 14.5, N 11.2°. Symbols are as in Figure 9. Extinction has increased from Region 2 and there is another aerosol layer above the first temperature inversion (positive $\Delta T/\Delta z$).

Figure 11) Radiosonde and LIDAR derived profiles typical for Region 4: Mixed Dust and Biomass (8° N – 3° N). This specific case was for DOY 26, N 7.5°. Symbols are as in Figure 9. Extinction is still high. The temperature, humidity and aerosol structure are all much more complicated than earlier in the cruise.

Figure 12) Radiosonde and LIDAR derived profiles typical for Region 5: Biomass burning (3° N – 5° S). This specific case was for DOY 29, S 2.3°. Symbols are as in Figure 9. Extinction is still high. Aerosol layer doesn't show a minimum between upper and lower layers.

Figure 13) Radiosonde and LIDAR derived profiles typical of the early portion of Region 6: Southern hemisphere clean (5° S – 24.5° S). This specific case was for DOY 30.5, S 7.4°. Symbols are as in Figure 9. Extinction is still high. This area was distinguished by having low surface extinction with an elevated aerosol layer with high extinction.

Figure 14) Radiosonde and LIDAR derived profiles typical of the later portion of Region 6: Southern hemisphere clean (5° S – 24.5° S) and Region 7: South Atlantic temperate marine air mass (24.5° S – 33° S). This specific case was for DOY 35.5, S 23.6°. Symbols are as in Figure 9. Extinction is now low again. This area is similar to the clean Northern Hemisphere case.

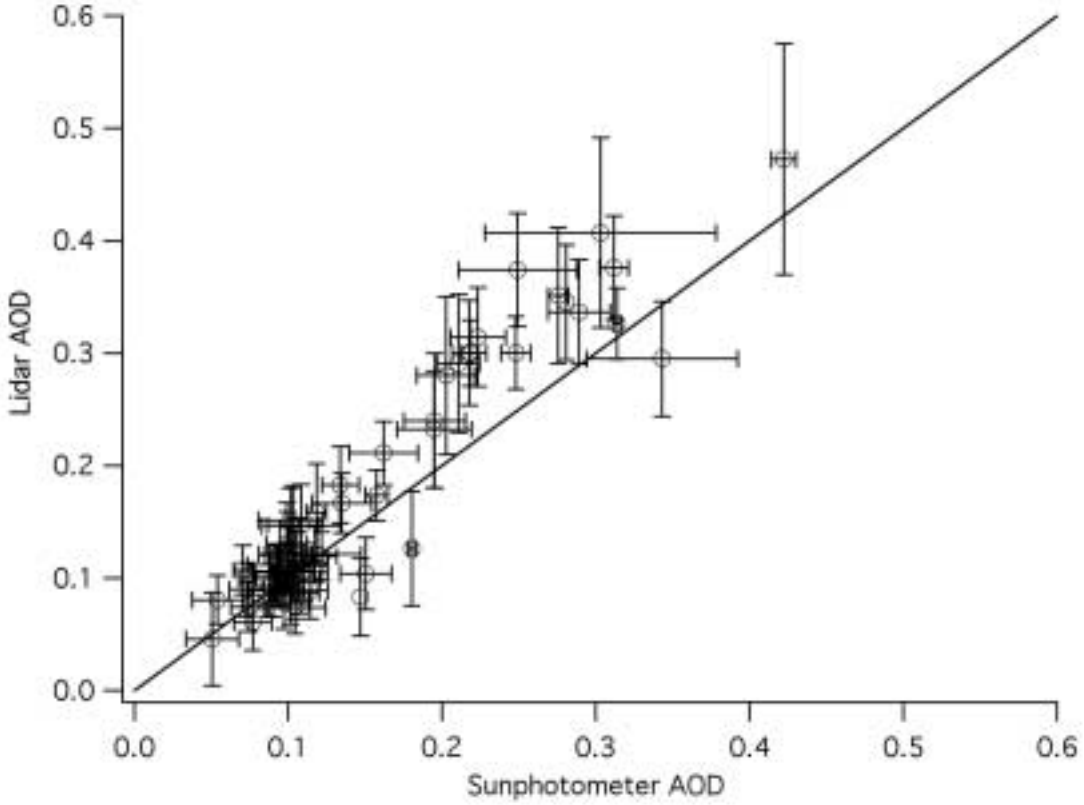

Figure 1

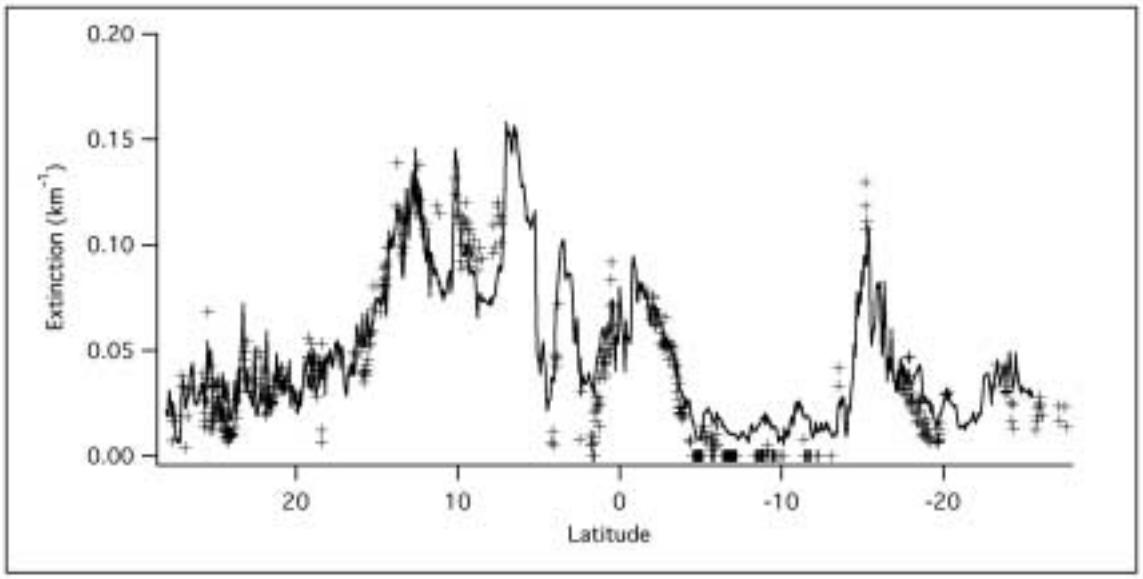

Figure 2

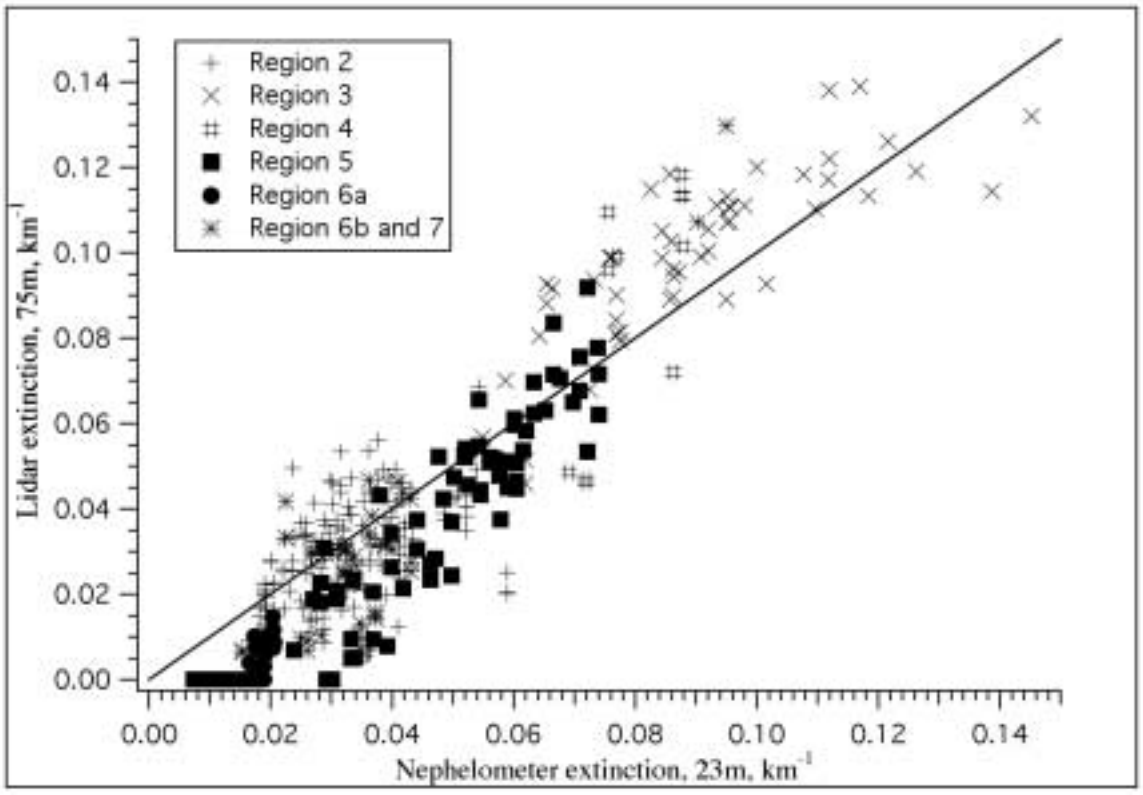
Region 2
Region 3
Region 4
Region 5
Region 6a
Region 6b and 7
Lidar extinction, 75m, km-1
Nephelometer extinction, 23m, km-1
0.00
0.02
0.04
0.06
0.08
0.10
0.12
0.14

Figure 3

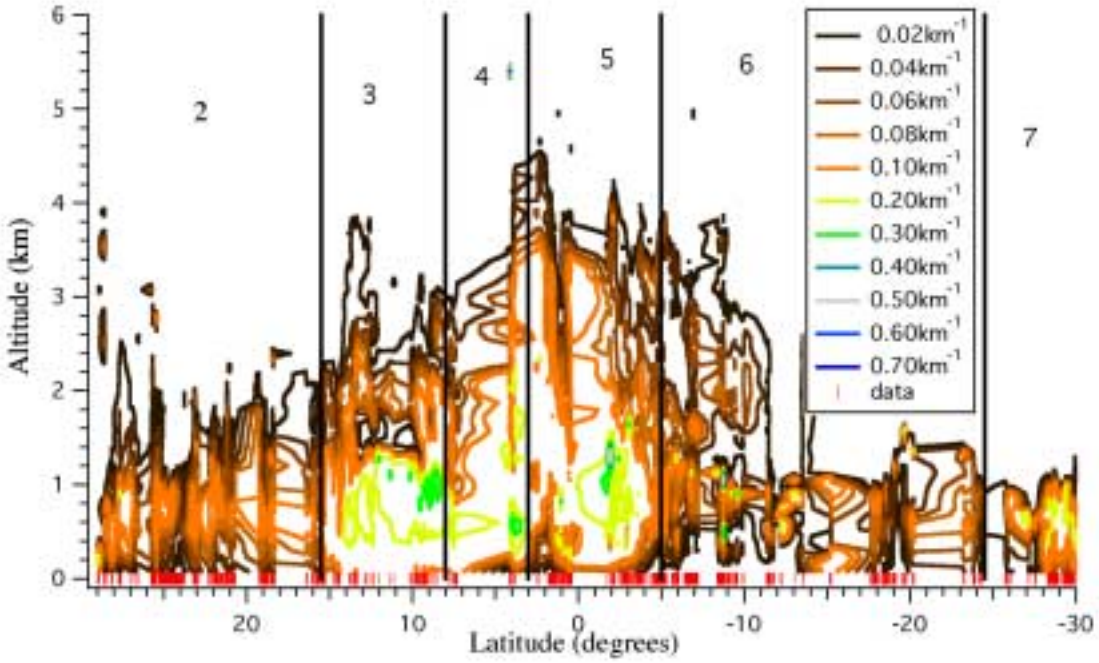
Altitude (km)
Latitude (degrees)
2
3
4
5
6
7
0.02km-1
0.04km-1
0.06km-1
0.08km-1
0.10km-1
0.20km-1
0.30km-1
0.40km-1
0.50km-1
0.60km-1
0.70km-1
data

Figure 4

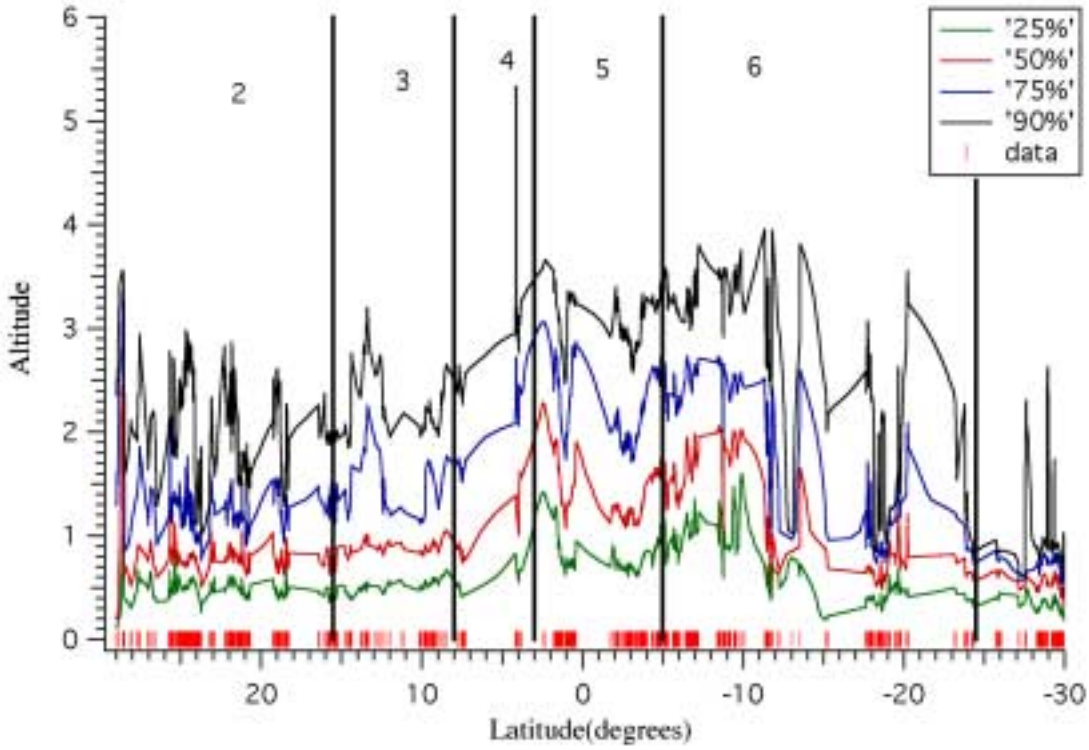
'25%'
'50%'
'75%'
'90%'
data
2
3
4
5
6
Altitude
Latitude(degrees)
0
1
2
3
4
5
6
20
10
0
-10
-20
-30

Figure 5

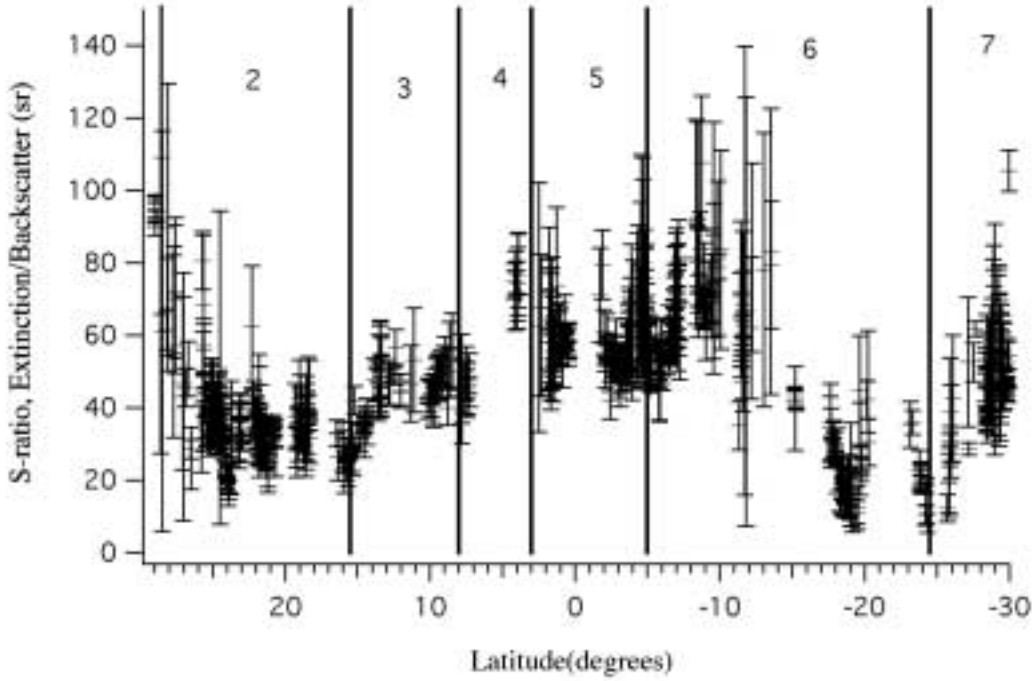
S-ratio, Extinction/Backscatter (sr)
140
120
100
80
60
40
20
0
2
3
4
5
6
7
20
10
0
-10
-20
-30
Latitude(degrees)

Figure 6

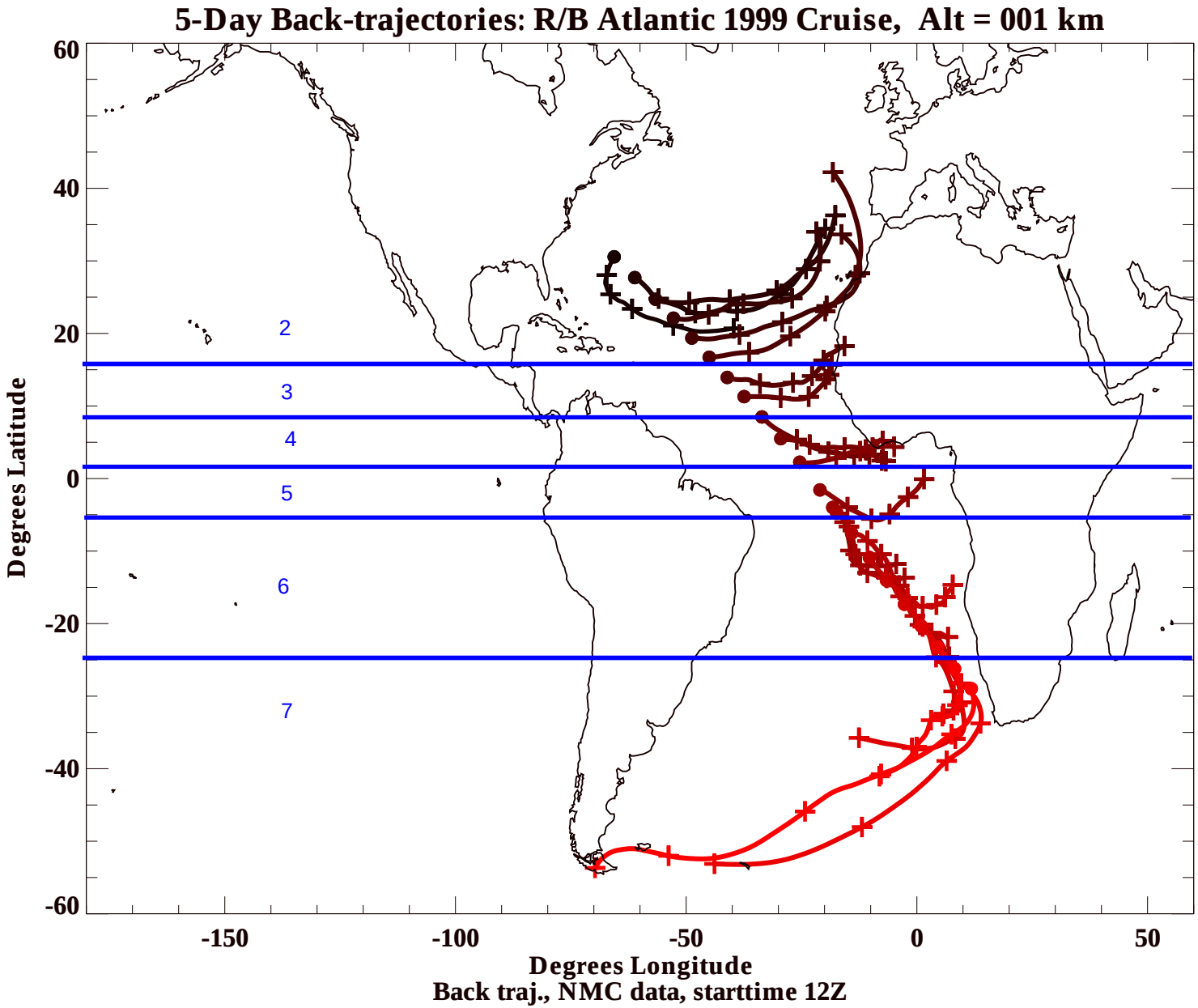
5-Day Back-trajectories: R/B Atlantic 1999 Cruise, Alt = 001 km
Degrees Latitude
60
40
20
0
-20
-40
-60
2
3
4
5
6
7
-150
-100
-50
0
50
Degrees Longitude
Back traj., NMC data, starttime 12Z

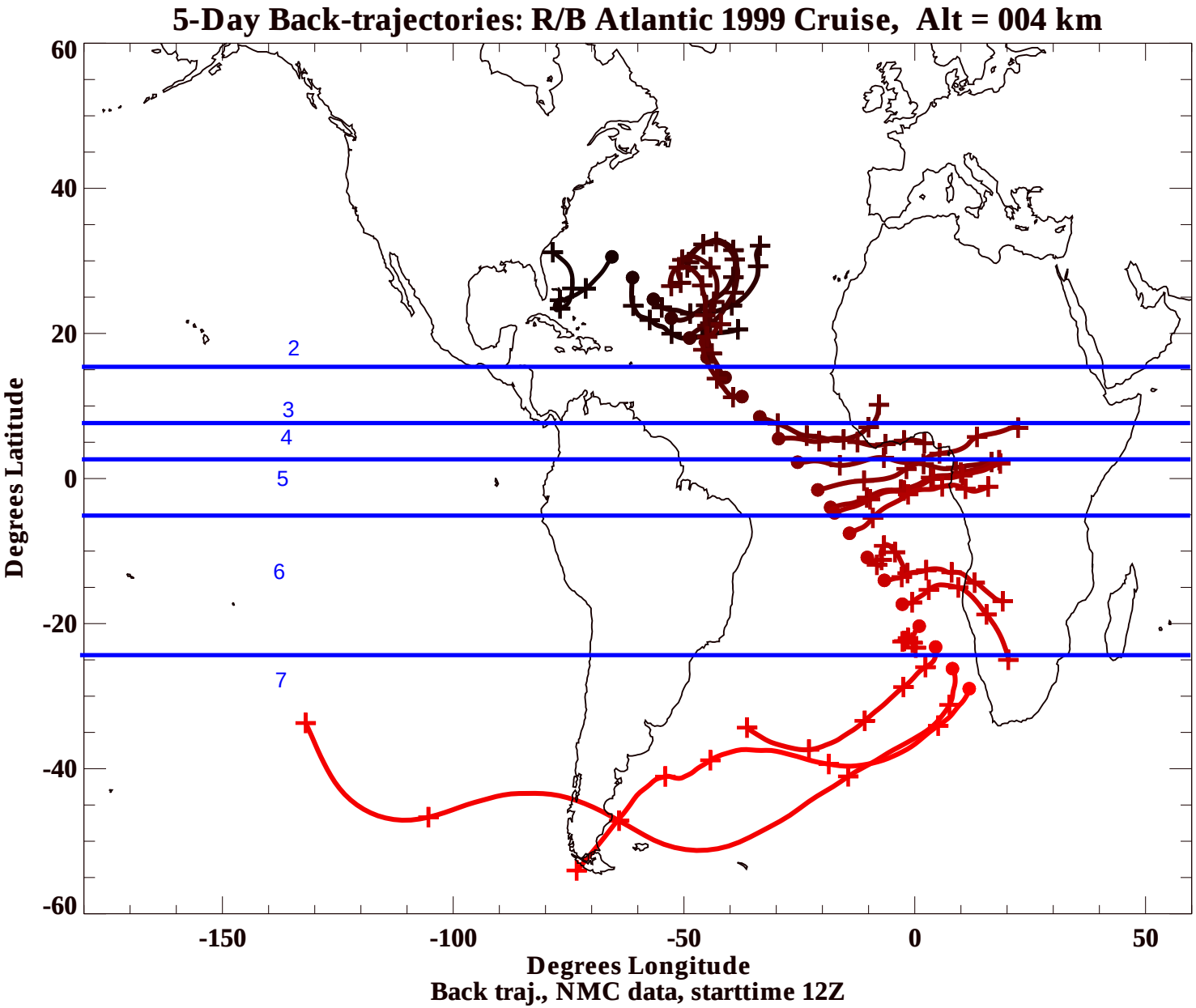
5-Day Back-trajectories: R/B Atlantic 1999 Cruise, Alt = 004 km
Degrees Latitude
60
40
20
0
-20
-40
-60
2
3
4
5
6
7
-150
-100
-50
0
50
Degrees Longitude
Back traj., NMC data, starttime 12Z

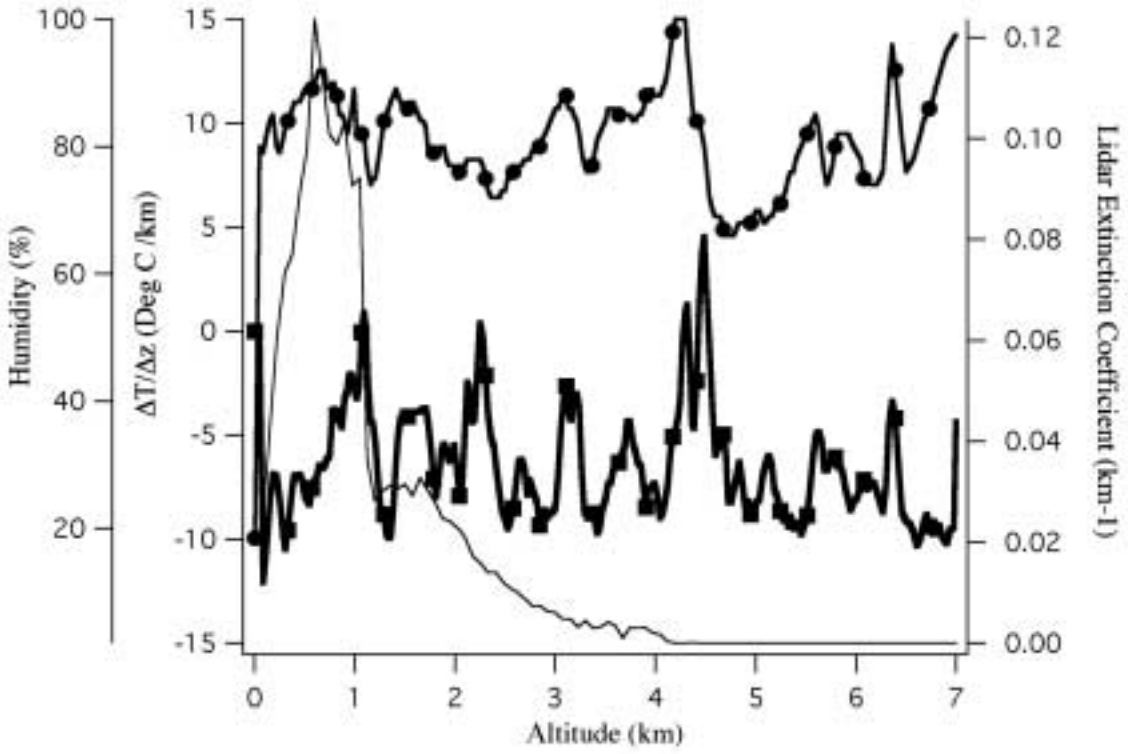
Humidity (%)
ΔT/Δz (Deg C /km)
Lidar Extinction Coefficient (km-1)
Altitude (km)
100
80
60
40
20
15
10
5
0
-5
-10
-15
0.12
0.10
0.08
0.06
0.04
0.02
0.00
0
1
2
3
4
5
6
7

Figure 9

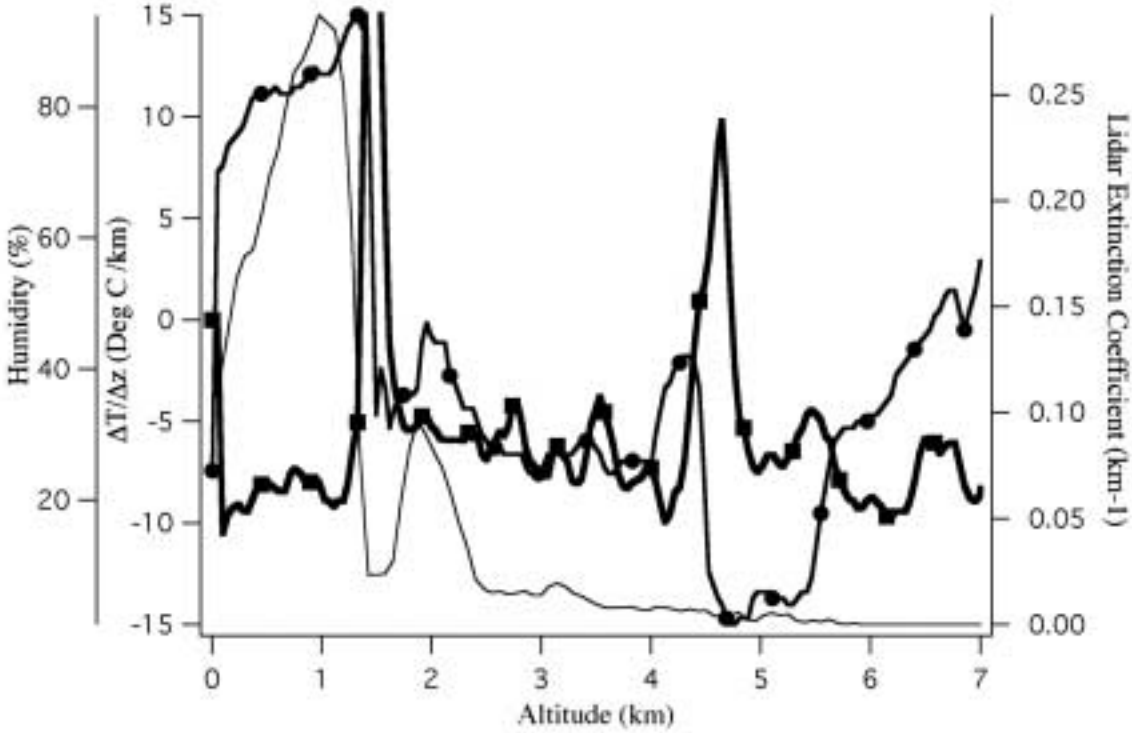
Humidity (%)
ΔT/Δz (Deg C /km)
Lidar Extinction Coefficient (km-1)
Altitude (km)
80
60
40
20
15
10
5
0
-5
-10
-15
0.25
0.20
0.15
0.10
0.05
0.00
0
1
2
3
4
5
6
7

Figure 10

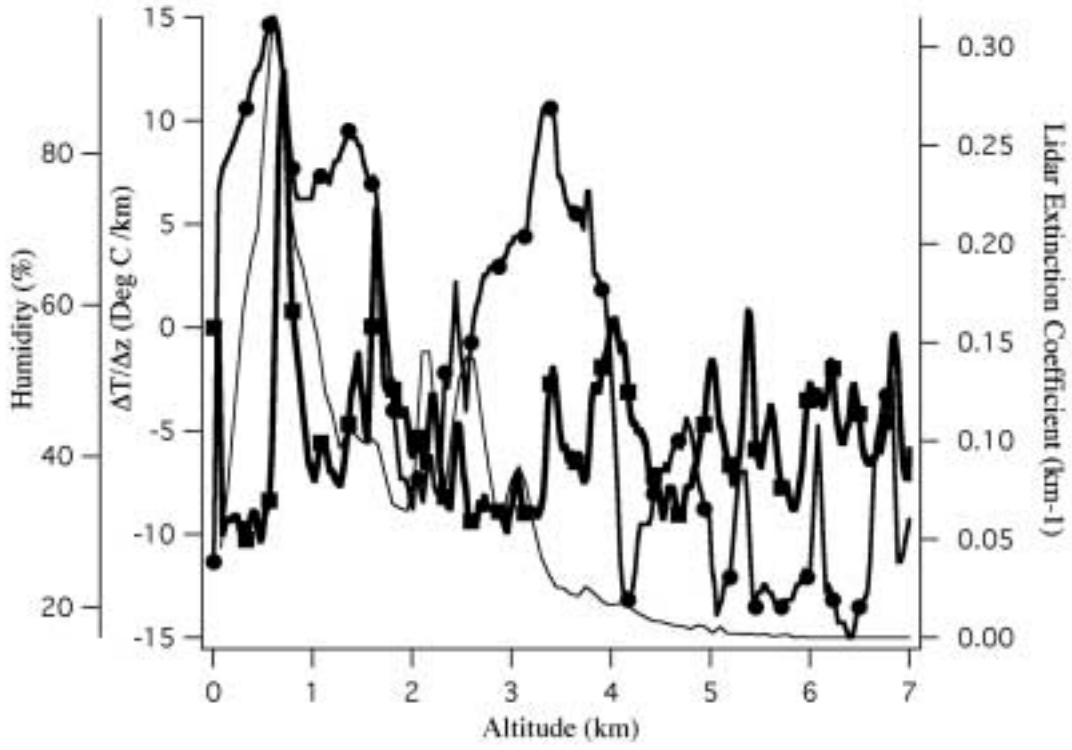
Humidity (%)
80
60
40
20
ΔT/Δz (Deg C /km)
15
10
5
0
-5
-10
-15
Lidar Extinction Coefficient (km-1)
0.30
0.25
0.20
0.15
0.10
0.05
0.00
0
1
2
3
4
5
6
7
Altitude (km)

Figure 11

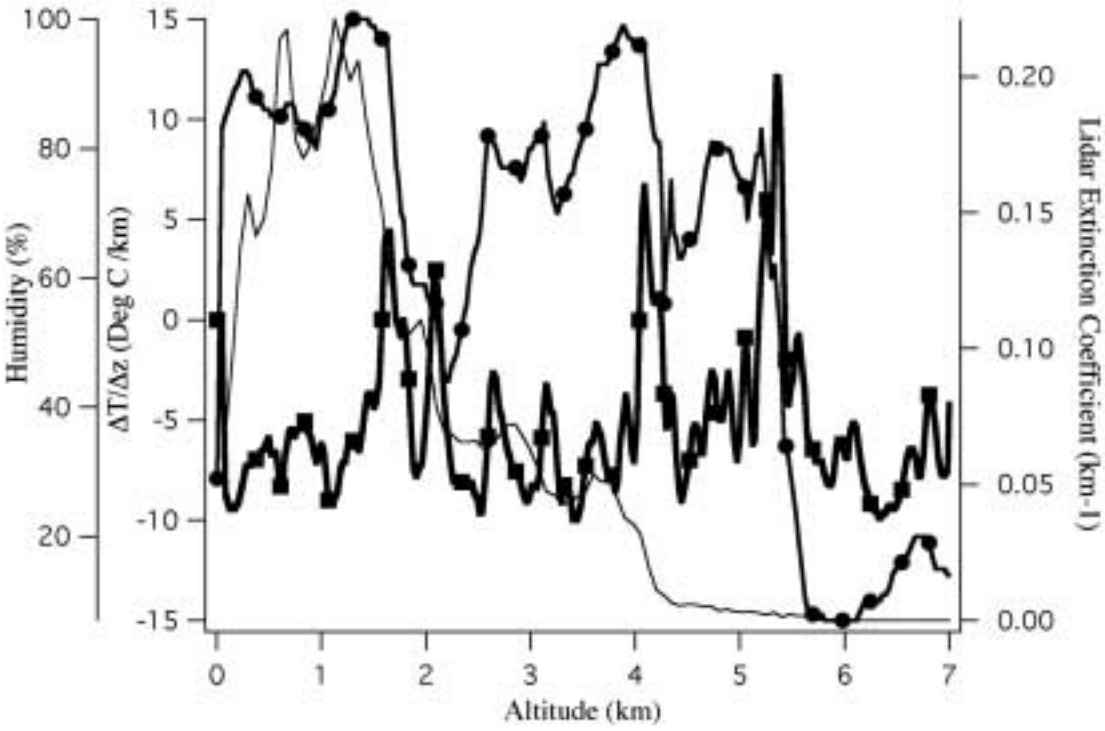
Humidity (%)
ΔT/Δz (Deg C /km)
Lidar Extinction Coefficient (km-1)
Altitude (km)
100
80
60
40
20
15
10
5
0
-5
-10
-15
0.20
0.15
0.10
0.05
0.00
0
1
2
3
4
5
6
7

Figure 12

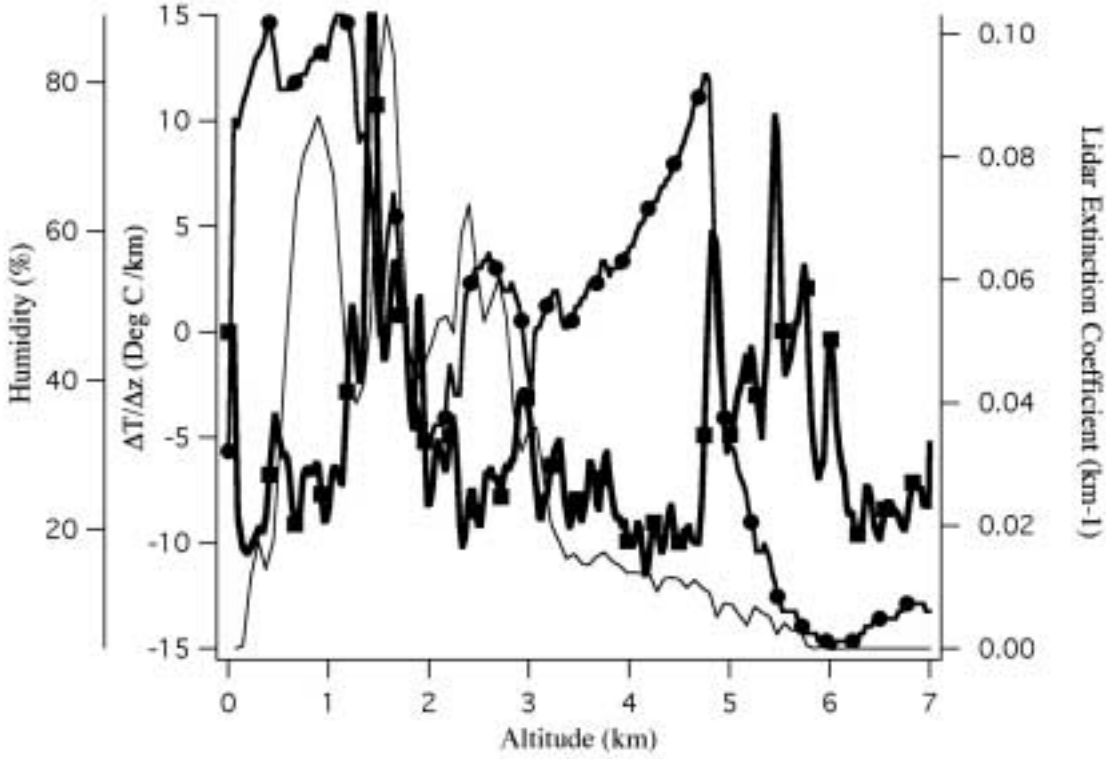
Humidity (%)
80
60
40
20
ΔT/Δz (Deg C /km)
15
10
5
0
-5
-10
-15
Lidar Extinction Coefficient (km-1)
0.10
0.08
0.06
0.04
0.02
0.00
0
1
2
3
4
5
6
7
Altitude (km)

Figure 13

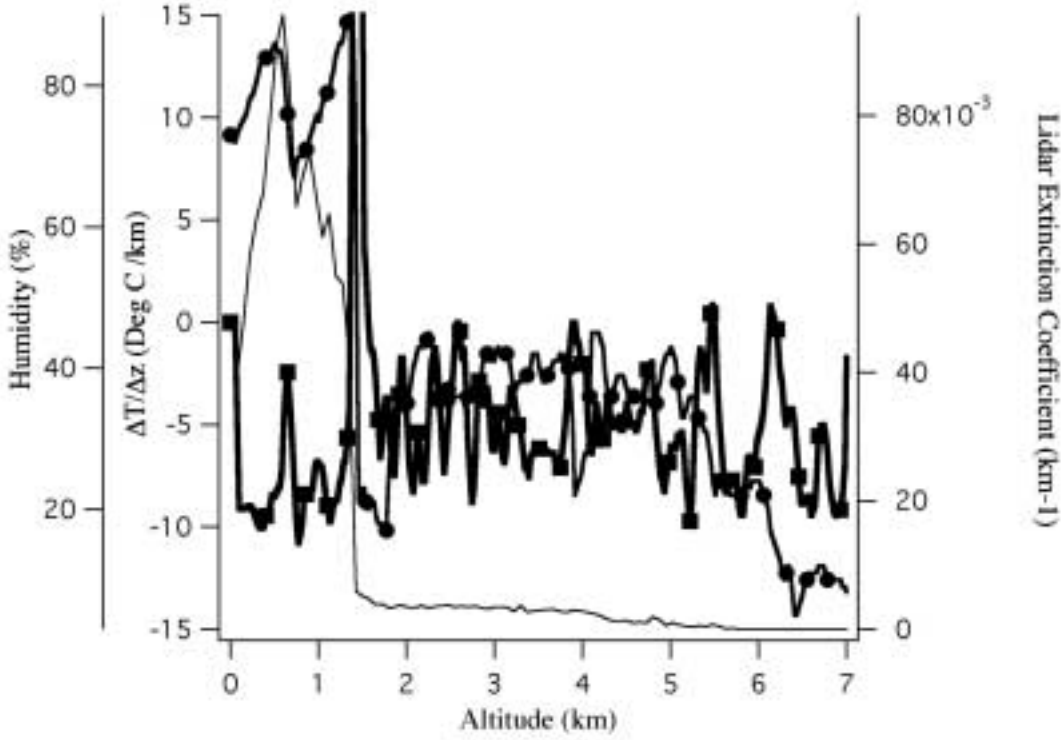
Humidity (%)
ΔT/Δz (Deg C /km)
Lidar Extinction Coefficient (km-1)
Altitude (km)
80x10-3

Figure 14

Appendix VII

Retrieval of Coccolithophore Calcite Concentration from SeaWiFS Imagery

(Submitted to *Geophysical Research Letters*)

Retrieval of Coccolithophore Calcite Concentration from SeaWiFS Imagery

Howard R. Gordon,[1] G. Chris Boynton,[1] William M. Balch,[2] Stephen B. Groom,[3]
Derek S. Harbour[4], and Tim J. Smyth[3]

[1]Department of Physics, University of Miami, Coral Gables, FL 33124
[2]Bigelow Laboratory for Ocean Sciences, West Booth Bay Harbor, ME 04575
[3]Centre for Coastal and Marine Sciences, Plymouth Marine Laboratory, Plymouth, Devon, PL1 3DH, UK
[4] Sir Alastair Hardy Foundation for Ocean Science, 1 Walker Terrace, Plymouth PL1 3BN, UK

Abstract

We examined blooms of the coccolithophorid *E. huxleyi*, observed in SeaWiFS imagery, with a new algorithm for the retrieval of detached coccolith concentration. The algorithm uses only SeaWiFS bands in the red and near infrared (NIR) bands to minimize the influence of the chlorophyll and dissolved organic absorption. We used published experimental determinations of the calcite specific backscattering and its spectral dependence, and assumed that the absorption coefficient of the medium was that of pure water, to estimate the marine contribution to the SeaWiFS radiance. The aerosol (and Rayleigh-aerosol interaction) contribution to the radiance was modeled as an exponential function of wavelength. These allow derivation of the coccolith concentration on a pixel-by-pixel basis from SeaWiFS imagery. Application to a July 30, 1999 SeaWiFS image of a bloom south of Plymouth, England indicates that the SeaWiFS estimates are in good agreement with surface measurements of coccolith concentration.

Introduction

Coccolithophores are small marine Prymnesiophyte phytoplankton which form external $CaCO_2$ scales (diameter ~ 2 μm and thickness 250 to 750 nm) called coccoliths. The coccoliths can form multiple layers and eventually detach. Coccolithophores are the

largest source of calcium carbonate on earth [Westbroek et al. 1985]. Of the coccolithophore species, *Emiliania huxleyi* is the most abundant, and its coccoliths can often be found from tropical to sub-arctic regions and further north into regions with water temperatures 0°C [Heimdal 1983]. The distribution of *E. huxleyi* coccoliths in sediments generally matches the distribution of the overlying species in the water column [McIntyre and Be 1967]. It can also be affected by biological processes such as grazing by marine zooplankton [Harris 1994], or microzones of bacterial decomposition which locally decrease the pH (see recent review by Milliman et al.[1999]). Dissolution of calcite depends on the depth of the calcite compensation depth. Approximately 20% of the biogenic carbonate is lost before accumulation in the sediments in regions such as the Sargasso Sea [Fabry and Deuser 1990], while 97% is lost in the Arabian Sea [Nair et al. 1989]. Even so, globally, calcium carbonate is responsible for about 75% of the deposition of carbon on the sea floor having a marine origin [Groom and Holligan 1987, Honjo 1986, Honjo 1990], it exceeds organic burial by a factor of seven. Thus, coccolith production is an important part of the biogenic carbon cycle.

The importance of coccolithophores to the overall particulate pool of phytoplankton had not been realized until the advent of remote sensing. Upwelling radiance measurements from the CZCS frequently showed large, mesoscale features in the temperate waters of both hemispheres. These features were sometimes characterized by complete saturation of band 3 (550 nm wavelength) of the CZCS. They were later attributed to intense light scattering by coccolithophores and associated coccoliths [Holligan et al. 1983]. Perhaps the most intriguing aspect of coccolithophores concerns the frequency of their blooms. Analysis of CZCS imagery showed 100-200 km diameter

coccolithophore blooms within temperate waters on an annual basis [Brown and Yoder 1994]. Apart from the inherent ecological interest in the development and fate of large-scale monospecific populations of phytoplankton, recent attention on the coccolithophores has focused on their role in global biogeochemical cycles [Holligan et al. 1993].

The Algorithm

Analysis of the influence of coccoliths on the water-leaving radiance [Gordon et al. 1988] suggests that determination of the coccolith concentration using spectral bands in the blue and green region of the spectrum requires the chlorophyll concentration (*Chl*). Unfortunately, estimation of *Chl* is difficult in such blooms. A second difficulty is that at high coccolith concentration the blue-green ocean color bands often saturate and must be abandoned. These problems can be circumvented by using the red and near infrared (NIR) spectral bands for two reasons. First, at these long wave-bands the absorption coefficient of sea water alone is so high that the additional absorption by phytoplankton and dissolved organic material is almost irrelevant. Second, because of the high water absorption, the water-leaving radiance in these bands is unlikely to become large enough to saturate the sensor.

The top-of-atmosphere (TOA) spectral reflectance $\rho_t(\lambda)$ can be written $\rho_t(\lambda) = \rho_r(\lambda) + \rho_A(\lambda) + t_p(\lambda)t_s(\lambda)\rho_w(\lambda)$, where $\rho_r(\lambda)$ is the contribution due to Rayleigh scattering in the atmosphere in the absence of the aerosol, $\rho_A(\lambda)$ is the contribution from scattering by the aerosol in the absence of the air (but including the Rayleigh –aerosol interaction), and $\rho_w(\lambda)$ is the contribution from the water-leaving radiance. The quantities $t_s(\lambda)$ and $t_p(\lambda)$ are the diffuse transmittances of the atmosphere, along a path

from the sea surface to the sun (t_s) and the sea surface to the sensor (t_p), at the wavelength λ.

Our algorithm uses SeaWiFS Bands 6, 7, and 8 (670, 765, and 865 nm). In these bands the water-leaving reflectance can be written approximately $\rho_w \cong b_b / 6(a_w + b_b)$, where a_w is the absorption coefficient of pure sea water, and b_b is the backscattering coefficient of the medium, e.g., see Gordon et al. [1988]. In coccolithophore blooms b_b results mostly from scattering by the coccolithophores and the detached coccoliths. For the 1991 coccolithophore bloom in the central North Atlantic, Balch et al. [1996] found empirically that the backscattering coefficient at 546 nm [$b_b(546)$ in m^{-1}] could be related statistically to the detached coccolith concentration [N_{Cocco} in ml^{-1}] through $b_b(546)=1.35\times10^{-7}\ N_{Cocco} + 3.06\times10^{-3}$, and to the concentration of calcite [C in moles/m^3] through $b_b(546)=1.6C - 0.0036$. In addition, the spectral variation of b_b could be approximated by $b_b(\lambda)\approx b_b(546)\times(546/\lambda)^{1.35}$, where λ is the wavelength in nm [Balch et al. 1996, Voss et al. 1998]. These relationships are used to relate $\rho_w(\lambda)$ to either N_{Cocco} or C.

For $\rho_A(\lambda)$ we use the Wang and Gordon [1994] approximation that $\rho_A(\lambda) \approx \rho_A(\lambda_0)\exp[a(\lambda_0 - \lambda)]$, where a is a constant and λ_0 is taken to be 865 nm. Because this algorithm cannot estimate aerosol properties, the diffuse transmittances of the atmosphere are modeled assuming that there is only Rayleigh scattering and, in the case of band 7, O_2 absorption.

Applying these observations and assumptions to the sensor-measured $\rho_t(\lambda) - \rho_r(\lambda)$ allows derivation of the three unknowns $b_b(546)$, $\rho_A(865)$, and a on a pixel-by-pixel basis using the SeaWiFS bands at 670, 765, and 865 nm, however, a correction using the visible bands is required to address the significant out-of-band response in bands 6 and 8

prior to application of the algorithm. This correction was developed using by applying the SeaWiFS spectral response functions to $\rho_t(\lambda) - \rho_r(\lambda)$ in the visible as described by Gordon [1995].

Results

We processed several images of coccolithophore blooms and found that spatial patterns in $b_b(546)$ and a showed distinct similarities in regions of intense blooms even though there is no obvious bloom structure evident in the sensor-measured reflectance at 865 nm. Assuming that a should be the same inside and outside the bloom, we believe that these similarities are due to small errors in the sensor calibration; however, we found that reducing the out-of-band contributions by a factor of two removed much of this covariation. (Note, if this procedure were not applied, the change in $b_b(546)$ due to incomplete correction for the atmosphere would be typically ~ 0.005 m^{-1}or less, corresponding to a detached coccolith concentration of ~ 70,000 ml^{-1}.) Figures 1 and 2 provide $b_b(546)$ and a, respectively, for a coccolithophore bloom off Plymouth, England acquired on July 30, 1999. Figure 1 shows that the maximum value of $b_b(546)$ is approximately 0.08 m^{-1}, and the minimum values are ~0.005 m^{-1} (near the upper left corner of the image). Figure 2 indicated that a shows only a hint of the bloom, suggesting that the procedure has successfully separated the water and atmospheric signals.

For the image shown in Figure 1, surface measurements of the concentration of detached coccoliths were made coincident with the satellite overpass, at the points marked with an "X." Samples for coccolithophore cell and detached coccolith concentration were taken in buffered formalin, and the concentrations estimated with an

inverted microscope. Using the relationship between $b_b(546)$ and N_{Cocco}, we estimated the detached coccolith concentration for the image. Figure 3(a) compares the coccolith estimated concentration, along a track joining the measurement locations, with the measured values. The error bars are an assumed 10% error in coccolith counts and a 12% standard deviation in the $b_b(546)$-N_{Cocco} relationship. The agreement is excellent. It should be noted that no attempt has been made to tune the algorithm to the measurements, other than to reduce the out-of-band correction by a factor of 2 to remove the similarity in the initial $b_b(546)$ and a patterns. For example, assuming *Chl* was nominally 1 mg/m^3 rather than zero, the retrieved $b_b(546)$ would increase by ~5% improving the agreement in Figure 3a. The analysis has been carried out completely using only previously published relationships between the variables. Figure 3(b) provides an estimate of the calcite concentration along the same track as in Figure 3(a).

Concluding Remarks

We have demonstrated the efficacy of a simple algorithm for retrieval of calcite concentration from coccolithophore blooms using SeaWiFS imagery. We used the detached coccolith concentration as an intermediate product (Figure 3a) only because it, rather than the calcite concentration, was measured coincident with the imagery. In application of the algorithm, normally one would proceed directly to calcite concentration from $b_b(546)$. Calcite concentration is preferable to detached coccolith concentration because (1) it includes coccoliths on plated cells, (2) the $b_b(546)$-C relationship shows less variability across coccolithophore species than the $b_b(546)$-N_{Cocco} relationship [Balch et al. 1998], and (3) calcite concentration is more relevant to ocean biogeochemistry than N_{Cocco}. Although no attempt here has been made to do so, we believe that given sufficient

surface truth the algorithm could be tuned to provide better retrievals. We encourage investigators observing coccolithophore blooms to sample them for microscopic counting in the event that they are also imaged by SeaWiFS.

The algorithm in its present form is capable of processing one orbit of a complete GAC image (North Pole to South Pole) in approximately five minutes, and is thus fast enough to be included in routine SeaWiFS processing. Although the algorithm is not capable of distinguishing between coccolithophore blooms features with similar high red-NIR reflectance, it can be combined with the Brown and Yoder [1994] classification algorithm to provide calcite concentration when the classification algorithm indicates the presence of a coccolithophore bloom.

Acknowledgments

The authors are grateful for support for this work from the U.S. Office of Naval Research (HRG) under grant number N00014-99-1-0007, NASA (HRG, WMB) under contract numbers NAS5-31363 and NAS5-31734. This research forms part of the Core Strategic Research Project on the Dynamics of Marine Ecosystems (DYME) of the Centre for Coastal and Marine Sciences, Plymouth Marine Laboratory, UK.

References

Balch, W.M., K. Kilpatrick, P.M. Holligan, D. Harbour, and E. Fernandez, The 1991 coccolithophore bloom in the central north Atlantic II: Relating optics to coccolith concentration, *Limnology and Oeanography,* **41**, 1684—1696, 1996.

Balch, W.M., D.T. Drapeau, T.L. Cucci, and R.D. Vaillancourt, Optical backscattering by calcifying algae: Separating the contribution of particulate inorganic and organic carbon fractions, *J. Geophys. Res.,* **104C**, 1541—1558, 1999.

Brown, C.W., and J.A. Yoder, Coccolithophorid blooms in the global ocean, *J. Geophys. Res.*, **99C**, 7467—7482, 1994.

Fabry, V.J., and W.G. Deuser, Aragonite and Magnesian fluxes to the deep sea, *EOS*, **71**, 161, 1990.

Gordon, H.R., O.B. Brown, R.H. Evans, J.W. Brown, R.C. Smith, K.S. Baker and D.K. Clark, A Semi-Analytic Radiance Model of Ocean Color, *J. Geophys. Res.*, **93D**, 10909—10924, 1988.

Gordon, H.R., Remote sensing of ocean color: a methodology for dealing with broad spectral bands and significant out-of-band response, *Applied Optics*, **34**, 8363—8374, 1995.

Groom, S.B., and P.M. Holligan, Remote sensing of coccolithophore blooms, *Advances in Space Research*, 7, 273--278, 1987.

Harris, R.P. Zooplankton grazing on coccolithophore *Emiliania huxleyi* and its role in inorganic carbon flux, *Marine Biology*, **119**, 431—439, 1994

Heimdal, B.R., Phytoplankton and nutrients in the waters north-west of Spitsbergen in the autumn of 1979, *Jour. Plankton Res.*, **5**, 901—918, 1983.

Holligan, P.M., E. Fernandez, J. Aiken, W. Balch, P. Boyd, P. Burkill, M. Finch, S. Groom, G. Malin, K. Muller, K. Purdie, C. Robinson, C. Trees, S. Turner, and P. van der Wal, A biogeochemical study of the coccolithophore, *Emiliania huxleyi*, in the North Atlantic, *Global Biogeochemical Cycles*, **7**, 879—900, 1993.

Holligan, P.M., M. Viollier, D.S. Harbour, P. Camus, and M. Champagne-Philippe, Satellite and Ship Studies of Coccolithophore Production Along the Continental Shelf Edge, *Nature*, **304**, 339—342, 1983.

Honjo, S., Oceanic particles and pelagic sedimentation in the western North Atlantic Ocean, The Geology of North America Vol. M, The Western North Atlantic Region, Geological Society of America, Ed. P.R. Vogt and B.E. Tucholke, 469—478, 1986.

Honjo, S., Particle fluxes at 47° N and 34° N 20° W stations between April 3 to September 26, 1989, *EOS*, **71**, 81, 1990.

McIntyre, A., A.W.H. Be, Modern Coccolithophorideae of the Atlantic Ocean -- I.Placoliths and cyrtoliths, *Deep Sea Res.*, **14**, 561—597, 1967.

Milliman, J., P.J. Troy, W. Balch, A.K. Adams, Y.-H. Li, and F.T. MacKenzie, Biologically-mediated dissolution of calcium carbonate above the chemical lysocline?, *Deep Sea Research*, **46**, 1653—1669, 1999.

Nair, R.R., V. Ittekkot, S.J. Monganini, V. Ramaswamy, B. Haake, E.T. Degens. B.N. Desai, S. Honjo, Increased particle flux to the deep ocean related to monsoons, *Nature*, **338**, 749—751, 1989.

Wang, M., and H.R. Gordon, A Simple, Moderately Accurate, Atmospheric Correction Algorithm for SeaWiFS, *Remote Sensing of Environment*, **50**, 231—239, 1994.

Westbroek, P., E.W. De Vrind-De Jong, P. Van der Wal, A. H. Borman, and J. P. M. De Vrind, Biopolymer-mediatedcalcium and manganese accumulation and biomineralization, *Geol. Mijnbouw*, **64**, 5—15, 1985.

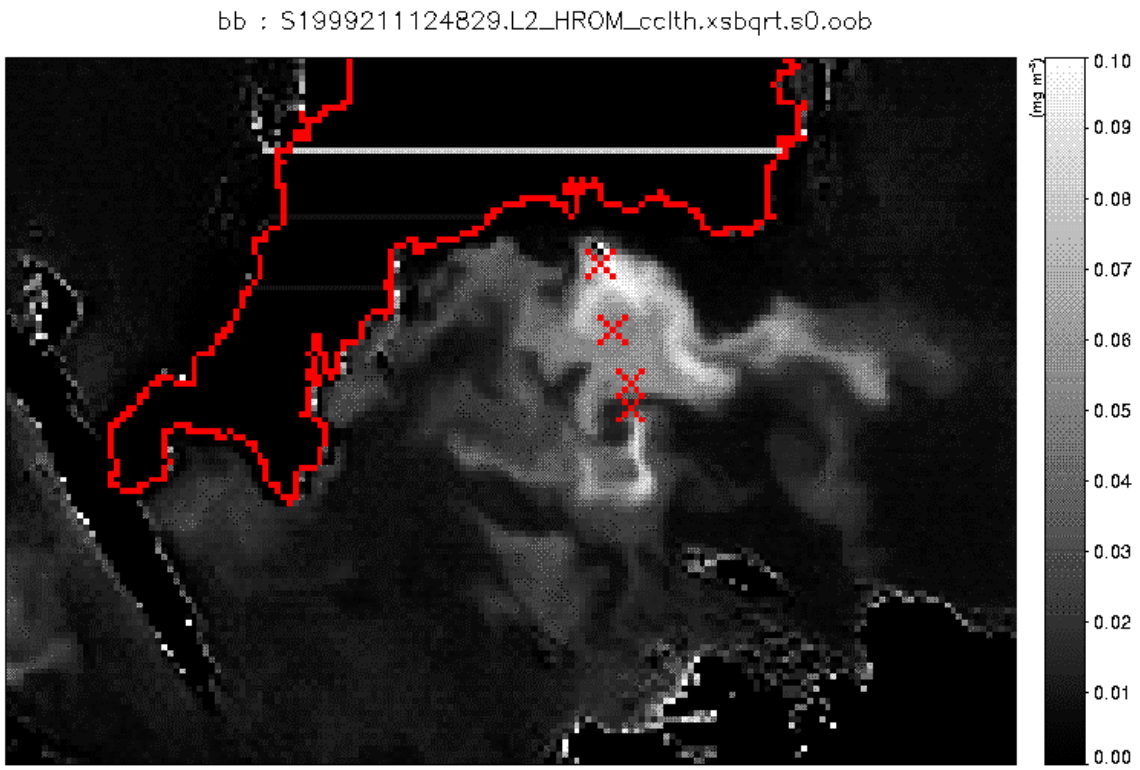

Figure 1. $b_b(546)$ in m^{-1} retrieved from the July 30, 1999 SeaWIFS image of Plymouth, England. Areas of enhanced backscattering result from a bloom of *E. Huxleyi*. The locations marked with "X" are the locations at which samples were taken to determine the concentration of detached coccoliths and of intact *E. Huxleyi* cells.

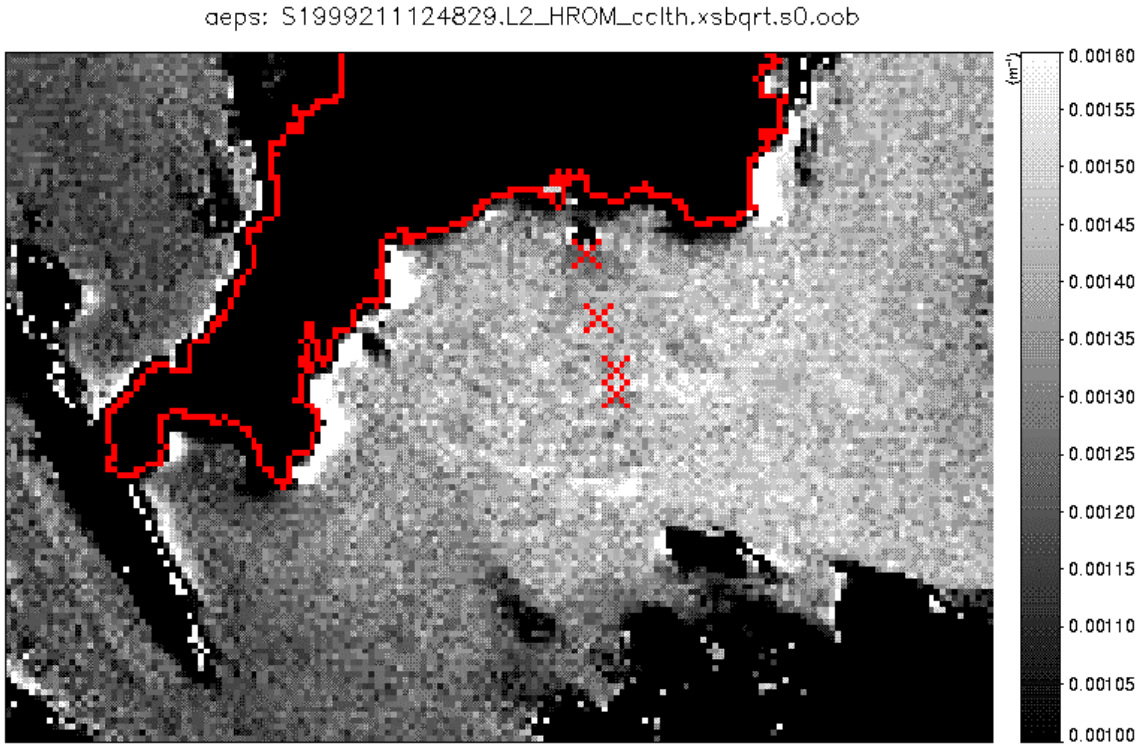

Figure 2. The atmospheric correction parameter *a* in nm^{-1} retrieved from the July 30, 1999 SeaWIFS image off Plymouth, England. Note that the coccolithophore bloom is net evident in this image.

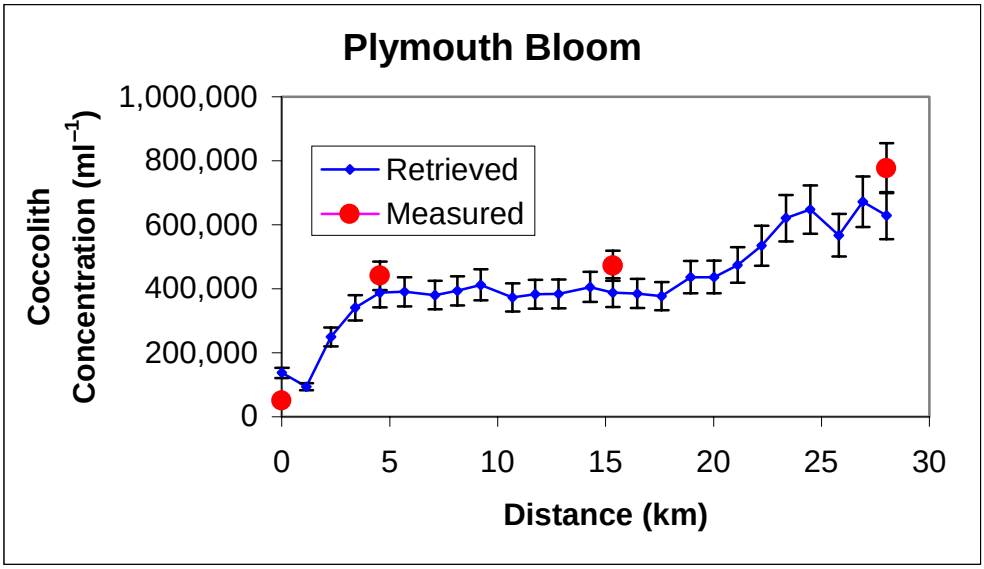

(a)

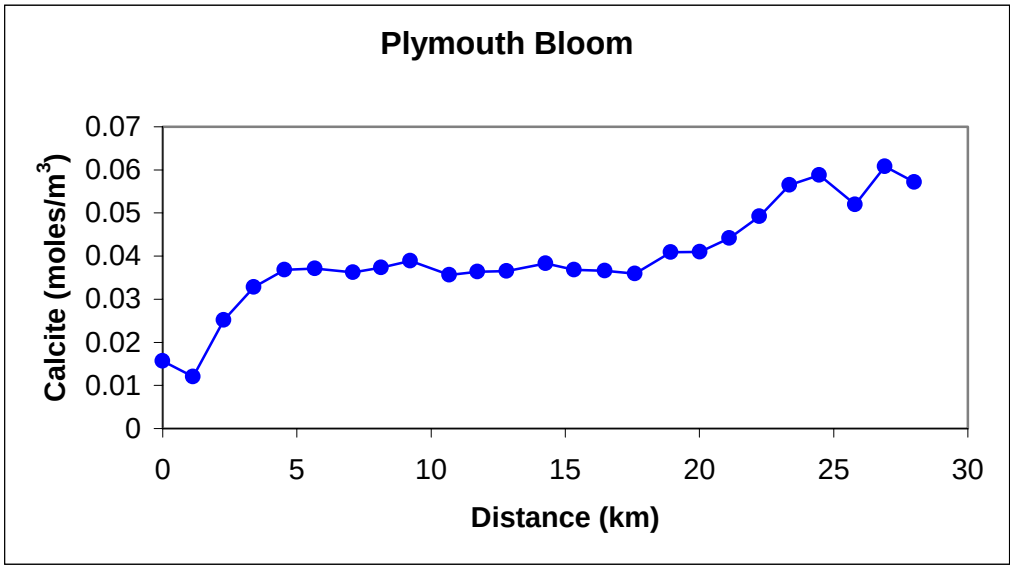

(b)

Figure 3. (a) comparison between retrieved and measured detached coccolith concentration (a), and (b) estimated calcite concentration along the same track as in (a).